Fakultät für Elektrotechnik und Informationstechnik
Lehrstuhl für Kommunikation und Navigation

Geostationary Data Relays for Low Earth Orbit Satellites

Johannes Sebastian Knogl

Vollständiger Abdruck der von der Fakultät für Elektrotechnik und Informationstechnik der Technischen Universität München zur Erlangung des akademischen Grades eines

Doktor-Ingenieurs (Dr.-Ing.)

genehmigten Dissertation.

Vorsitzender: Univ.-Prof. Dr.-Ing. Thomas Eibert

Prüfer der Dissertation:

1. Univ.-Prof. Dr. sc. nat. Christoph-Georg Günther
2. Prof. Michel Bousquet,
   Université de Toulouse / Frankreich

Die Dissertation wurde am 18.06.2014 bei der Technischen Universität München eingereicht und durch die Fakultät für Elektrotechnik und Informationstechnik am 11.06.2015 angenommen.

Abstract

Low Earth Orbiting (LEO) satellites play a central role in Earth observation. The improved resolution of their instruments generates high data volumes. In some applications, this data should furthermore be available in near real-time. Geostationary (GEO) relay satellites offer an attractive perspective for providing the required connectivity. Traditional approaches, however, become complex when many satellites are to be served simultaneously. The present thesis proposes a new approach for providing the required connectivity with a reduced complexity.

The geostationary data relay is designed to serve a large number, say 15, Low Earth Orbit (LEO) satellites concurrently. Data rates of $30 - 100$ Mbit/s per LEO-GEO inter-satellite link meet the required downlink capacity of many current and future LEO satellite missions. The GEO satellite is kept simple. Transparent transponders make the concept flexible in the long-term for future modulation or coding schemes. The GEO satellite requires an antenna system which is able to serve the 15 LEO satellites simultaneously. For this purpose, a new antenna concept was developed. The reflector setup of the antenna system was designed to map the radiation from LEO satellites at different positions on separate spots on an antenna array. This requires a special aplanatic reflector setup. The antenna array consists of 1600 patch antennas which are dynamically grouped in 2x2 sub-arrays. The sub-arrays are activated according to the movement of the LEO satellites. A switch unit enables reconfiguring the sub-arrays. It also routes the Radio Frequency (RF) signals to the transponders. The required number of transponders is limited to the number of maximum supported LEO satellites, thus providing a cost-efficient design. The switch unit uses Micro Electromechanical System (MEMS) switches on a Printed Circuit Board (PCB) to save space and weight.

The performance of the system is dependent on the choice of the active 2x2 sub-arrays following the LEO satellite movements. In order to determine the optimal choice, both the information about the GEO satellite antenna pointing and the GEO satellite antenna position is required. Two cost-efficient estimation methods were developed to provide this information. The antenna pointing is estimated by matching the 2x2 sub-arrays receiving the highest LEO satellite signal power levels with the nominal locations of the mapped LEO satellites. The latter are determined with a high accuracy using Global Navigation Satellite Systems (GNSS). Simulations show antenna pointing accuracies of $< 0.05°$.

The GEO satellite position is estimated using the LEO satellites as navigation satellites. Pseudorange measurements on the LEO-GEO ISLs supported by two-way GEO-Earth range measurements enable a position estimation similar to GNSS positioning. Simulation results show real-time GEO satellite positioning accuracies in the order of meters and post processed accuracies in the order of centimeters.

It is planned to validate some of the concepts developed in this thesis in satellite experiments. They shall be performed on the geostationary satellite Heinrich-Hertz of the German Aerospace Center (DLR) as well as on the OPS-Sat satellite of the European Space Agency (ESA).

Zusammenfassung

Die folgende Arbeit beschreibt ein neues Kommunikationskonzept für geostationäre (GEO) Datenrelais Satelliten. Das Datenrelais ermöglicht es, eine größere Anzahl von Low Earth Orbit (LEO) Satelliten gleichzeitig durch Intersatelliten-Links anzubinden. Mit dem neuen Konzept werden die Signale der LEO Satelliten auf ein Array von Einzelstrahlern abgebildet, die immer dann aktiviert werden, wenn sie durch einen LEO Satelliten angestrahlt werden. Über eine neue Schaltmatrix werden die empfangenen Signale zu transparenten Transpondern weitergeleitet. Die Signalverteilung auf dem Antennenarray wird genutzt, um die Lage des GEO-Satelliten zu schätzen. Die Position des GEO-Satelliten wird bestimmt, indem die LEO-Satelliten als Navigationssatelliten genutzt werden.

Contents

Acronyms

ADS-B	Automatic Dependent Surveillance - Broadcast
BPSK	Binary Phase Shift Keying
BRTS	Bilateral Ranging Transponder System
CCD	Charge-Coupled Device
CDMA	Code Division Multiple Access
CP	Connection Point
CRB	Cramér-Rao Bound
DLR	German Aerospace Center
DOP	Dilution of Precision
ECEF	Earth Centered Earth Fixed
ECSS	European Cooperation for Space Standardization
EDRS	European Data Relay System
EGNOS	European Geostationary Navigation Overlay Service
EIRP	Equivalent Isotropically Radiated Power
ESA	European Space Agency
FDF	Flight Dynamics Facility
FDMA	Frequency Division Multiple Access
FOV	Field of View
FPGA	Field Programmable Gate Array
FSS	Fixed Satellite Services
GEO	Geostationary Orbit
GNSS	Global Navigation Satellite System
GOCE	Gravity Field and Steady-State Ocean Circulation Explorer
GPS	Global Positioning System
GSFC	Goddard Space Flight Center
HPA	High Power Amplifier
HPOP	High Precision Orbit Propagator
HST	Hubble Space Telescope
ILRS	International Laser Ranging Service
IP	Insertion Point
ISL	Inter-Satellite Link

ITU	International Telecommunication Union
JPL	Jet Propulsion Laboratory
LCT	Laser Communication Terminal
LEO	Low Earth Orbit
LNA	Low Noise Amplifier
LOS	Line-of-Sight
LTCC	Low Temperature Co-Fired Ceramic
MEMS	Micro Electromechanical System
MEO	Medium Earth Orbit
NASA	National Aeronautics and Space Administration
NRT	Non Real-Time
NTC	Non-Time Critical
PCB	Printed Circuit Board
PDOP	Positional Dilution of Precision
PPP	Precise Point Positioning
PSK	Phase Shift Keying
RF	Radio Frequency
RT	Real-Time
RX	Receive Side
SDR	Software Defined Radio
SLR	Satellite Laser Ranging
SNR	Signal-to-Noise Ratio
SPDT	Single Pole Double Throw
SSO	Sun-Synchronous Orbit
STC	Slow-Time Critical
STK	System Tool Kit
TDMA	Time Division Multiple Access
TDRSS	Tracking and Data Relay Satellite System
TM	Telemetry
TOA	Time of Arrival
TT&C	Telemetry, Tracking and Command
TUM	Technische Universität München
TX	Transmit Side
UAV	Unmanned Aerial Vehicle
WAAS	Wide Area Augmentation System

Chapter 1

Introduction

Satellite services play a fundamental role in modern society. Besides television broadcasting, communication services and navigation solutions, Earth observation becomes more and more important. New applications for agricultural and ecological surveillance require data from satellite resource monitoring. Disaster response and rescue operations need information about the affected areas of operation. The military and intelligence use such capabilities as well. Finally, tracking services for vessels and aircrafts demand access to position and telemetry data collected by satellites for traffic planning and security.

The resolution of the cameras and radars used in Earth observation steadily increases. This leads to a tremendous growth in the data volumes. In the future, a larger downlink capacity will be necessary. Furthermore, the data for applications like air traffic surveillance is only useful for a very short period of time. These applications need a real-time access to the satellites. Two developments are necessary to satisfy these requirements with existing infrastructure in the future. One is to increase the data rate on the downlink, the other one is to increase the contact times by increasing the number of satellite ground stations. But both approaches have limits.

The data rates on the downlinks of Earth observation satellites have been increased steadily during the last few decades. An example of this can be seen in Table 1.1 for the *Landsat* Earth observation satellites by the National Aeronautics and Space Administration (NASA). However, a further increase in data rates on radio frequency (RF) channels is technically limited by the size of the antennas and the power to supply the amplifiers as well as by the frequency spectrum.

Landsat Generation	Launch Date	Data Rate
Landsat 1	1972	15 Mbit/s
Landsat 4	1982	85 Mbit/s
Landsat 7	1999	150 Mbit/s
Landsat 8	2013	384 Mbit/s

Table 1.1: Evolution of the increase in the data rates of the *Landsat* Earth observation satellites during the last few decades.

The contact times of a single ground station to Earth observation satellites are limited by the geometry of the satellite-ground station configuration. The satellites have to orbit at altitudes between $200 - 1500$ km in so called Low Earth Orbits (LEO) in order to achieve the desired imaging resolutions. Due to their orbital periods of approximately 100 min, they can only contact a single ground station for a few minutes per pass. A network of ground stations spread over the world can reduce the gaps between the contact times. However, even with a 9-station network like the ESTRACK core network of the European Space Agency (ESA), contact gaps to LEO satellites of up to several hours occur. In addition, the maintenance and operation of a ground station network is expensive.

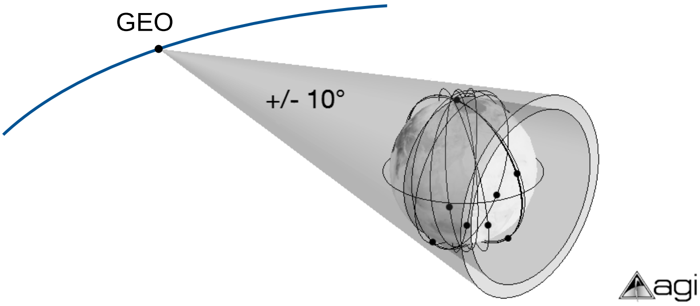

Figure 1.1: Satellite constellation consisting of 15 LEO satellites and one GEO satellite. The LEO satellites are located within a solid angle of approximately ±10°.

In order to overcome the problems of limited download capacity and interrupted access times, geostationary relay satellites are an attractive solution. A geostationary data relay receives the data from LEO satellites via inter-satellite links and forwards it to the ground. The main advantage, compared to direct LEO-Ground links, is the large Field of View (FOV). A GEO satellite can cover up to 69% of the LEO satellite orbits (see Figure 1.1). Only two geostationary data relays are required to provide uninterrupted real-time access to LEO satellites. Only one single ground station is required for transferring the data from each LEO satellite to the ground. Due to the extended contact times, data rates of $30 - 100$ Mbit/s on the inter-satellite links (ISLs) are sufficient to serve download volumes of several Tbit per day. This exceeds current downlink volumes with margins.

So far, three different geostationary data relay systems have been developed. The US Tracking and Data Relay Satellite System (TDRSS) by NASA is most widely known. The system originally consisted of two GEO satellites. The first two operational TDRSS satellites were launched in 1983 and 1988. They were equipped with two onboard steerable antennas, each supporting a single ISL. The relays could provide return data rates of up to 300 Mbit/s in S-band and Ku-band. Each satellite carried an additional 30 element helical array providing five return links at 100 kbit/s. The satellites were built in order to complement the network of ground stations and to provide longer communication times to the space shuttle and other spacecrafts. The second generation of TDRSS satellites launched in 2000 is able to provide a maximum data rate of 800 Mbit/s in S-, Ku- and Ka-band (cf. Miller and Berndt [1996] and Lewis [1996]).

Another system is the Russian Luch data relay. Its first satellite, Kosmos 1700, was launched in 1985. The satellite was equipped with two data channels and was intended for real-time video transmission between the Russian space station MIR and the operation center. The most recent satellite Luch 5V was launched in April 2014 and provides seven transponders with data rates of 5 MBit/s in S-band and 150 MBit/s in Ku-band (cf. ISS Reshetnev [2013]).

The European Space Agency (ESA) started a geostationary data relay project in 2011 as a public-private partnership, together with EADS Astrium. This European Data Relay Satellite System (EDRS) focuses mainly on high data rate links. Instead of RF communication links the system is based on optical links. A Steerable Laser Communication Terminal (LCT) shall support data rates up to 1.8 Gbit/s. The first satellite is planned for launch in 2014 (cf. Witting and Kably [2012]).

A recent publication also proposes to use the Inmarsat-4 constellation as a system of geostationary data relays for low data rate connections of less than 500 kbit/s in the L-band (Johnston et al. [2012]). 256 spot beams shall cover the LEO satellite orbits and provide data links for Inmarsat SB-SAT terminals.

Geostationary data relay systems can be classified according to their data rates:

- $<$ 1 Mbit/s: Low data rate geostationary data relays for Telemetry, Tracking and Command (TT&C) purposes. Such data relays can be realized with global horn antennas (see Katona [2012]).
- 1-100 Mbit/s: Intermediate data rate geostationary data relays for payload downlink. High gain RF antennas on the LEO and GEO satellites are required.
- $>$ 100 Mbit/s: High data rate geostationary data relays for dedicated payload downlink. ESA uses optical communication links to reach such high data rates.

The geostationary data relay satellites launched within the mentioned programs successfully provide point-to-point communication links by steering their antennas. But so far, they have not addressed the concurrent communication with a substantial number of satellites, e.g. 15 satellites, at intermediate data rates of $30 - 100$ Mbit/s, or many more satellites if the links are multiplexed. For example, LEO satellite payloads that capture the Automatic Dependent Surveillance - Broadcast (ADS-B) signals of aircrafts produce rather low data rates, but can be installed on constellations like Globalstar with approximately $30 - 50$ satellites. They can all be accommodated on a single transponder. A geostationary data relay of the described type provides a cost-efficient solution to the problem of limited downlink capacity and real-time capabilities for whole constellations of Earth observation satellites. Therefore, the following thesis presents a new design for geostationary data relays fulfilling these requirements.

Conventional designs using a single reflector antenna for each ISL would exceed the space and mass budgets of the geostationary data relay for providing many links in parallel. Therefore, a new concept for an antenna system was developed. It is presented in Chapter 3. The frequency band was chosen to be the Ka-band, in order to reduce the dimensions of the antenna. Furthermore, it avoids the highly occupied lower frequency bands, which enables larger bandwidth allocation. The antenna concept makes use of a special aplanatic dual-reflector setup. A homogenous gain over a FOV of ±10° is achieved. Within this FOV, more than 80% of all currently active LEO satellites are covered. Radiation from different positions within the FOV is focused on separate spots on a patch antenna array, similar to the functionality of a CCD camera. This divides the FOV in spot beams.

The LEO satellites access the geostationary data relay using a Frequency Division Multiple Access (FDMA) scheme with frequency reuse among the spot beams. The signals of active spot beams are routed to the transponders by a switch matrix. The switches are RF Micro Electromechanical System (MEMS) devices in order to save weight and space. The number of RF-chains is at most equal to the number of supported LEO satellites. Thus, the complexity of the RF hardware scales up mainly with the number of satellites, rather than with the FOV of the antenna system.

Since the LEO satellites are moving, hand-overs from active spot beams to their adjacent ones are necessary. Thereby, the correct moment of the hand-over is decisive. If the hand-over is not timed perfectly, a fraction of the signal power is not focused on the active antenna element. A loss in gain and therefore a potential disruption of the communications performance are the consequence. In order to determine the correct timing of the hand-over, the attitude and the position of the GEO satellite must be known. The communications concept and the antenna system enables the development of new concepts for the attitude and for the position estimation of the GEO satellite. The concepts make only use of the existing communications infrastructure and are therefore cost-efficient.

The attitude determination concept presented in Chapter 4 is based on the information provided by the multibeam antenna system. An error in the satellite attitude causes a displacement of the focal points on the two-dimensional antenna array. These errors can be determined by searching for the rotations which match the displaced focal points with the original non displaced ones. Using this approach, calibration errors between the attitude determination hardware and the antenna pointing are excluded. Separate hardware for attitude determination becomes dispensable. Simulations show an attitude accuracy of $< 0.05°$.

The new positioning concept for geostationary data relays is presented in Chapter 5. It uses the LEO satellites, precisely positioned by onboard GNSS receivers, as navigation satellites for the GEO satellite. Similar to GNSS positioning, pseudoranges between the LEO satellites and the GEO satellite are used to determine the GEO satellite position. The pseudorange measurements can be conducted concurrently to the data transmission, which makes the operation resource efficient and economic. The dynamics in the signal sources enables an effective estimation of the biases on the LEO-GEO pseudoranges. In addition, the dedicated communication links provide high Signal-to-Noise Ratio (SNR) levels which reduces the pseudorange code noise.

Powerful receiver hardware on ground enables efficient processing. Simulations show real-time positioning accuracies in the order of meters and post processed accuracies in the order of centimeter. This exceeds the accuracies of most of the conventional ground based approaches.

The focus during the design of the geostationary data relay concept was on a simple and compact setup, both on the hardware side as well as on the communication architecture. The successful "bent-pipe" technology for GEO satellites using a transparent transponder to relay the LEO satellite data shall be applied. This provides flexibility in the long-term without restriction on the implemented modulation or coding schemes. No onboard processing is necessary. The LEO satellites take care of the signal conditioning. Besides the application as a geostationary data relay for multiple LEO satellites, the proposed system concept is also suited for UAVs (Unmanned Aerial Vehicles) or for ground, airborne or maritime terminals.

Chapter 2

Communications Concept for Geostationary Data Relays

2.1 Preliminary Design Studies

The design of a communications concept for geostationary data relays requires the knowledge of the LEO satellite orbit statistics. It determines the visibility of the LEO satellites from the geostationary orbit and thus the LEO-GEO contact times. The contact times and the required downlink capacity by current and future LEO satellite missions determine the data rates on the inter-satellite links. The following two sections show results which are the basis for deriving the communications architecture requirements in Section 2.2.

2.1.1 Analysis of LEO Satellite Orbit Statistics

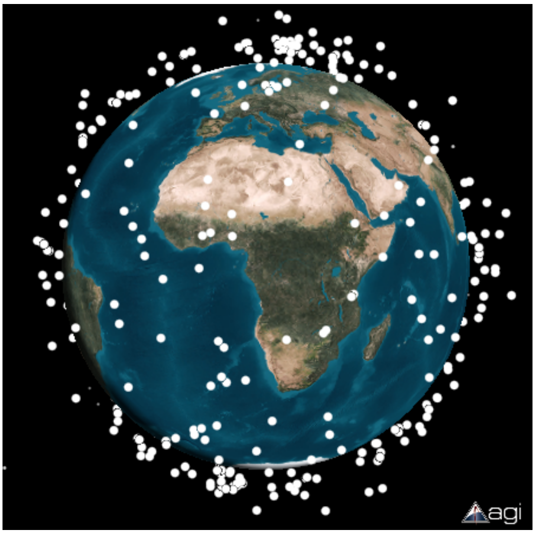

Figure 2.1: Current distribution of active LEO satellites as seen from the GEO orbit.

Statistics of Analytical Graphics Inc. show that approximately 1000 active satellites are currently orbiting the Earth. Slightly more than 460 move at altitudes below 1600 km and are therefore called Low Earth Orbit (LEO) satellites (see Figure 2.1). Another group of satellites is located at approximately $20\,000 - 23\,000$ km altitude. This Medium Earth Orbit (MEO) counts approximately 70 active spacecrafts including in particular the navigation satellites for the Global Positioning System (GPS), GLONASS, Beidou and Galileo. The third set of satellites are the geosynchronous satellites located at 35 786 km altitude. They have a population of approximately 400 active satellites.

In the following analysis of the LEO satellite orbit statistics we are mainly interested in Earth observation satellites. If we exclude the two big self-contained communication constellations Iridium and Globalstar, 390 LEO satellites remain. Figure 2.2 shows the LEO satellite distribution classified by the altitude and inclination. The main fraction of LEO satellites moves in orbits between 400 km and 900 km (> 80%). The inclinations of the orbital planes range between 10° to 110°. Most of the LEO satellites are injected in polar orbits to enable Sun-Synchronous Orbits[1] (SSO) at their altitudes. SSO are favored by LEO satellites, since the orbital plane of SSO can be chosen to have the satellite's solar panels continuously illuminated by the sun. This ensures a continuous power generation. In addition, objects on the same Earth latitude are seen at the same local mean solar time leading to an equal sun angle. It makes it easier to compare images.

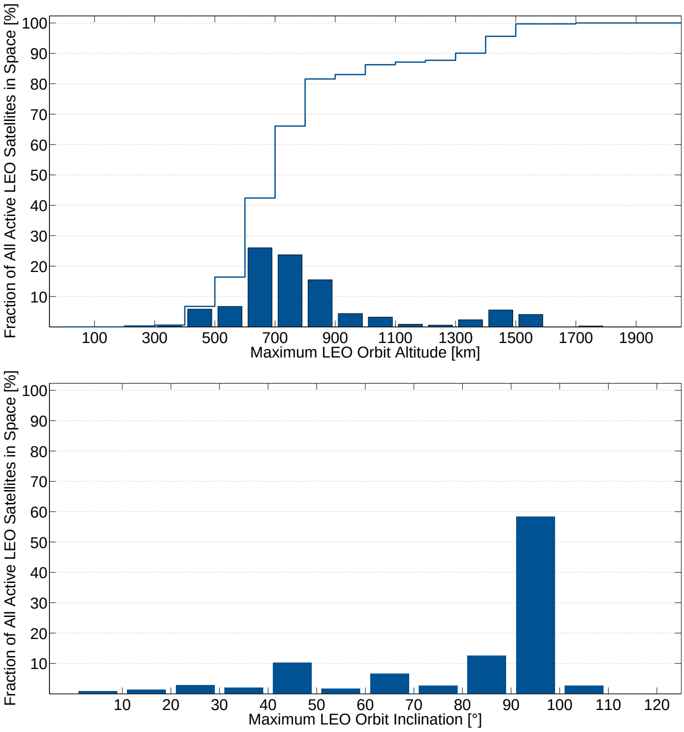

Figure 2.2: *Upper figure:* LEO satellite altitude statistics and cumulative representation (blue curve) including all LEO satellites up to a certain altitude. *Lower figure:* LEO satellite statistics considering the orbital inclination.

---

[1] For a certain choice of the inclination and the altitude of the orbit, the inhomogeneous mass distribution of the Earth with peak near the equator causes the orbital plane of the spacecraft to rotate by approximately one degree eastwards per day with respect to the celestial sphere. Therefore, the rotation of the orbital plane follows the Earth's movement around the Sun.

The GEO satellite sees a two dimensional projection of the Earth and the LEO satellite distribution. In this projection, the Earth becomes a disc. The two dimensional projection of the LEO satellite density is maximum near the border of the disc and forms a ring. This projected LEO satellite density has peaks near the poles of the Earth disc due to the preferred polar orbits (cf. Figure 2.1).

2.1.2 Analysis of LEO-GEO Contact Times

Without restrictions in the Field of View (FOV) of a GEO satellite, a minimum fraction of 54% and a maximum fraction of 100% of a LEO satellite orbit are visible. The fraction depends on the LEO satellite's altitude and the orientation of the orbital plane. The rest of the orbit is shadowed by the Earth. On average 65% of a typical LEO satellite orbit (500 km altitude and polar orbit) are visible. Correspondingly, on average 65% of all LEO satellites out of a constellation are simultaneously visible for a geostationary data relay. Due to their low altitudes, LEO satellites have orbital periods of about 100 min. Hence, a geostationary data relay can establish contact to a LEO satellite for about 65 min until it disappears behind the Earth.

Figure 2.3 shows the evolution of the number of visible LEO satellites out of a constellation of 15 LEO satellites. The satellites are chosen to form a representative selection according to the LEO satellite statistics concerning altitude and inclination (see Table 5.5 in Section 5.3). The evolution shows that on average 9.6 LEO satellites are visible.

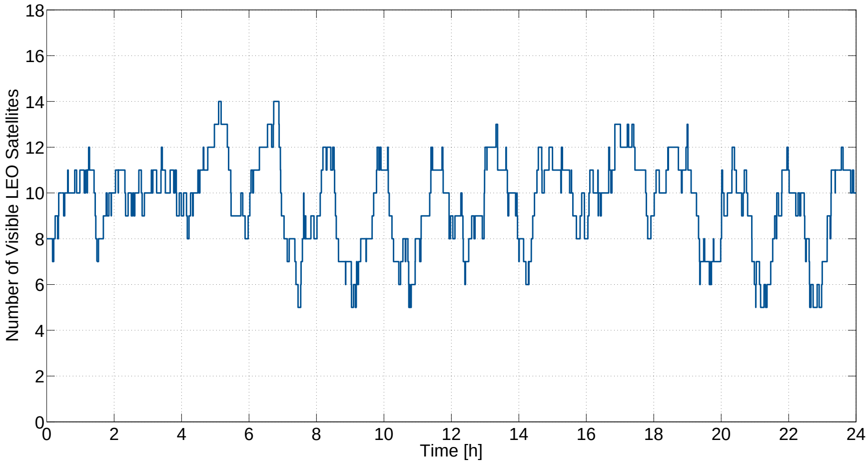

Figure 2.3: Number of visible LEO satellites out of a 15 LEO satellite constellation. On average 9.6 LEO satellites are visible, which corresponds to approximately 65%.

A single geostationary data relay enables access times to the LEO satellites of $> 50\%$. Already two geostationary data relays, located at opposite sides of the Earth, provide a coverage of 100% of the LEO satellite orbits (higher than 75 km). A continuous real-time access to onboard data is assured. Figure 2.4 illustrates such a constellation with two geostationary data relays and two ground stations.

In case political or economic reasons don't allow a second ground station outside the home country, an inter-satellite link between the two geostationary data relays is an alternative. One geostationary data relay transmits its data to the second relay and from there to the ground. The lower figure of Figure 2.4 shows such a scenario. Due to an angle of $< 180°$ between both GEO satellites and the center of the Earth, LEO satellites have to orbit on a minimum altitude of 305 km to be visible 100% of the time.

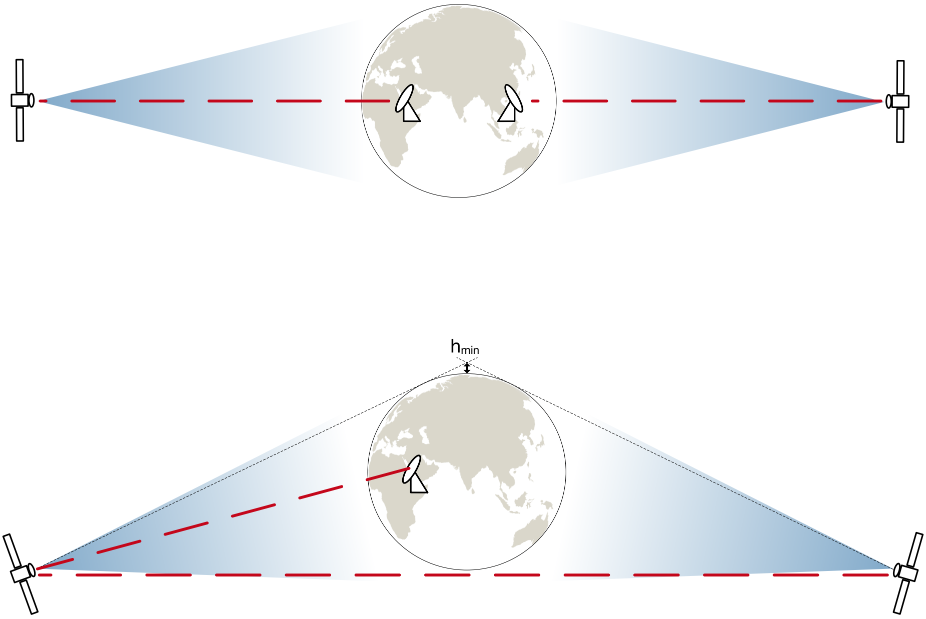

Figure 2.4: *Upper Figure:* Two geostationary data relays, located at opposite positions of the Earth, cover LEO satellite orbits higher than 75 km for 100%. *Lower Figure:* If only one ground station shall be used, an inter-satellite link connects both geostationary data relays. Due to an angle of $< 180°$ between both GEO satellites and the center of the Earth, only LEO satellites with a minimum altitude of $h_{min} = 305$ km are covered for 100%.

An interesting analysis is the comparison of the contact times of a single geostationary data relay to LEO satellites with the contact times a single ground station and a network of ground stations can establish to LEO satellites. In order to analyze these contact times, a simulation has been performed. It determines the contact times to TerraSAR-X, the Hubble Space Telescope (HST) and the DLR-TUBSAT LEO satellites by the geosynchronous telecommunication satellite ARTEMIS, the ground station Weilheim I and the core network of ground stations of the ESTRACK ground station network of the European Space Agency (ESA) (cf. Figure 2.5). The simulation results in Table 2.1 show up to approximately double the contact times by the ARTEMIS satellite compared to the ESTRACK network of 9 antennas (8 separate locations).

Figure 2.5: Sites of the core network of ESA's ESTRACK ground station network and location of the ground station Weilheim I.

	TerraSAR-X	**HST**	**DLR-TUBSAT**
	Apogee 510 km	Apogee 568 km	Apogee 733 km
	Perigee 507 km	Perigee 563 km	Perigee 713 km
	Period 94.8 min	Period 96.0 min	Period 99.2 min
	Inclination 97.4 deg	Inclination 28.5 deg	Inclination 98.7 deg
DLR			
Weilheim I Lat. 47.9 deg Long. 11.1 deg	1:00 h 4.2%	0:17 h 1.2%	1:19 h 5.5%
ESA			
Kourou Lat. 5.25 deg Long. -52.8 deg	0:35 h	1:34 h	0:49 h
Maspalomas Lat. 27.8 deg Long. -15.6 deg	0:40 h	1:20 h	0:56 h
Villafranca Lat. 40.4 deg Long. -4.00 deg	0:47 h	0:45 h	1:06 h
Cebreros Lat. 40.6 deg Long. -4.37 deg	0:47 h	0:44 h	1:07 h
Redu Lat. 50.0 deg Long. 5.15 deg	0:58 h	0:08 h	1:22 h
Santa Maria Lat. 37.0 deg Long. -25.1 deg	0:45 h	0:57 h	1:05 h
Kiruna Lat. 67.9 deg Long. 21.0 deg	1:51 h	0:00 h	2:22 h
Perth Lat. -31.8 deg Long. 115.9 deg	0:42 h	1:13 h	0:58 h
New Norcia Lat. -31.0 deg Long. 116.2 deg	0:42 h	1:14 h	0:58 h
ESTRACK (9 antennas)	7:47 h 32.4%	7:55 h 33.0%	10:43 h 44.7%
GEO satellite			
ARTEMIS	15:55 h 66.3%	14:03 h 58.5%	17:17 h 72.0%

Table 2.1: Average contact times per day between the ESA ESTRACK core ground station network, the Weilheim ground station site, and the ARTEMIS geosynchronous satellite to TerraSAR-X, the Hubble Space Telescope (HST) and the DLR-TUBSAT. The simulation period was the 14.10.2009 10:00 to 24.10.2009 10:00. The ARTEMIS satellite shows up to approximately double the contact times than the ESTRACK network of 9 antennas (8 separate locations). The overall contact times by ARTEMIS range between 58.5 – 72.0%.

2.2 Communication Architecture Requirements

The analysis and statistics performed in Section 2.1 are the base to design the communications concept for the geostationary data relay. The following requirements define the communications concept.

- The geostationary data relay shall provide concurrent access to 15 LEO satellites. 15 LEO satellites are selected as a baseline for representing a ”large” number of LEO satellites. It substantially exceeds the number of supported LEO satellites by existing geostationary data relays like TDRSS, Luch or EDRS.

- The geostationary data relay shall provide a data rate of 30 – 100 Mbit/s on each LEO-GEO Inter-Satellite Link (ISL). The choice is based on the analysis of the LEO-GEO contact times with the aim to fulfill the downlink capacity requirements of current and future LEO satellite missions. Table 2.2 shows that with a data rate of 30 – 100 Mbit/s the current download volumes of small Earth observation satellites like RapidEye are exceeded with margin in the required downlink capacity. But also the large download volumes of satellites like TerraSAR-X or EnMap can be served.

Satellite (Launch date)	Data Rate to Single Ground Station	Single Ground Station (∼ 5% contact)	Geostationary Data Relay (65% contact, 30 Mbit/s)	Geostationary Data Relay (65% contact, 100 Mbit/s)
Radarsat 2 (2007)	105 Mbit/s	454 Gbit/day	1700 Gbit/day	5600 Gbit/day
TerraSAR-X (2007)	300 Mbit/s	1296 Gbit/day		
RapidEye (2008)	80 Mbit/s	346 Gbit/day		
Met-Op-B (2012)	70 Mbit/s	303 Gbit/day		
EarthCARE (2015)	150 Mbit/s	648 Gbit/day		
EnMAP (2017)	320 Mbit/s	1382 Gbit/day		

Table 2.2: Maximum downlink data volumes per day for direct ground links and via a geostationary data relay.

- The frequency band for the ISLs and the GEO-Ground return link shall be 27 GHz in Ka-band. This reduces the size and therefore weight of the antenna structures with equal gain compared to lower frequency bands. In addition, this frequency band is less occupied in comparison to S-band and X-band and therefore allows to allocate large bandwidth. According to the International Telecommunication Union (ITU) Radio Regulations (ITU [2008]) the selected frequency band is dedicated to ISLs and fixed satellite services.

- The GEO satellite shall be equipped with transparent transponders with a standard transponder bandwidth of 36 MHz. No onboard processing shall be applied. This ensures a longterm flexibility of the satellite's hardware, being independent on the choice of future modulation and coding schemes. The number of transponders shall match the number of supported LEO satellites.

- The GEO satellite antenna for the ISLs shall provide a Field of View (FOV) of at least ±10°. This covers LEO satellite orbits up to 950 km altitude, i.e. more than 80 % of all LEO satellites. Orbits with larger altitude are covered partly, if the orbital plane is not perpendicular to the GEO-Earth axis (see Figure 2.6)

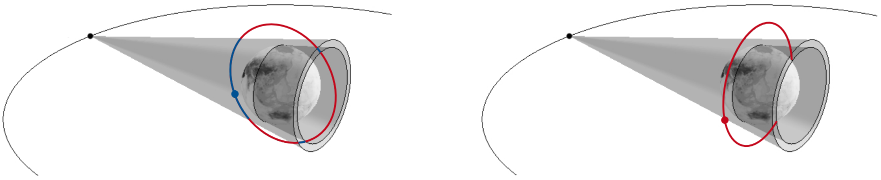

Figure 2.6: *Left:* LEO satellite orbital plane parallel to GEO-Earth axis: While the satellite is crossing the FOV, contact is possible (blue parts). *Right:* LEO satellite orbital plane perpendicular to GEO-Earth axis: No contact possible.

- The FOV shall be subdivided into a large number of spot beams. Only the antenna elements of active spot beams shall forward their signals to the transponders with the help of an RF switch matrix. Spot beams lead to an economic exploitation of frequency resources.

- The spot beams shall have a size of approximately 1° beamwidth. This is a trade-off between two parameters. The first parameter is the number of spot beams needed to cover the FOV which determines the complexity of the antenna system. The second parameter is the worst case overlap time, i.e. the time during which more than one LEO satellite are in the same spot beam. This parameter influences the available data rates, since within one spot beam, two LEO satellites have to share one transponder. Figures 2.7 to 2.8 show the analysis of the influence of the spot beamwidth on the two parameters. Assumptions about a representative constellation of LEO satellites considering altitude and inclination are taken into account. A spot beamwidth of 1° leads to a number of 400 spot beams to cover the FOV and an overlap time of $< 5\%$.

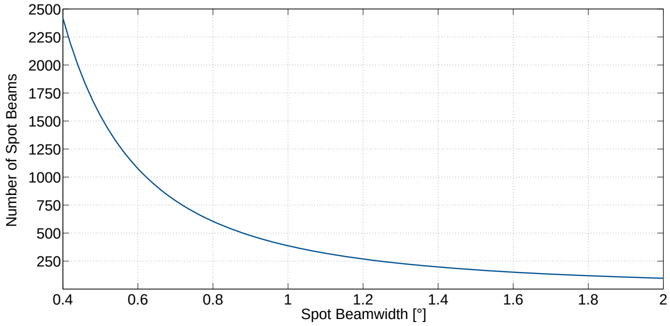

Figure 2.7: Estimated number of spot beams needed to cover a FOV of ±10°.

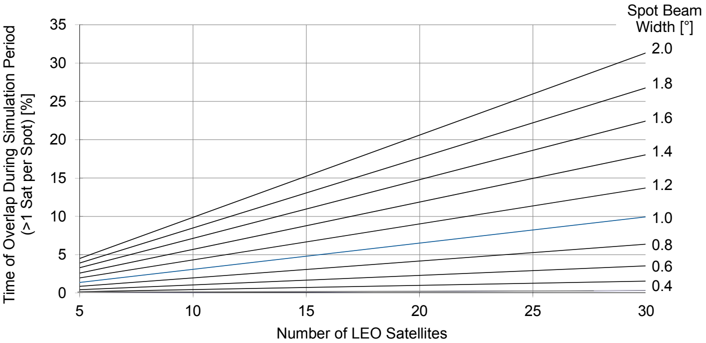

Figure 2.8: Spot beam overlap of TerraSAR-X with other satellites dependent on the cell size and the number of LEO satellites in the supported constellation.

The choice of the spot beamwidth also has influence on the occupation of the spot beams with LEO satellite signals and on the spot beam transit times. Figure 2.9 illustrates this occupancy for a ±10° FOV subdivided into hexagonal spot beams of 1° diameter. Spot beams pointing near the projected border of the Earth are more occupied compared to spot beams pointing towards the center due to the density distribution of the LEO satellites (cf. Section 2.1.1). Figure 2.10 shows the distribution of the spot beam transit times.

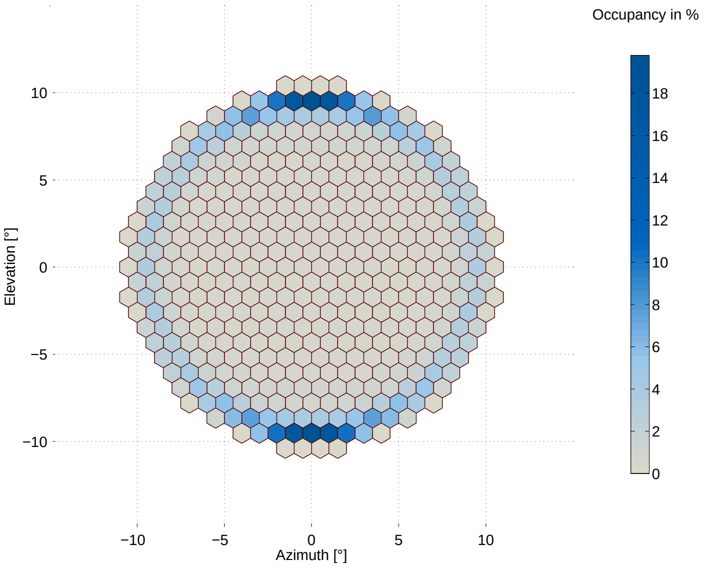

Figure 2.9: Mean LEO satellite occupancy of spot beams in a geostationary data relay's field of view of ±10°. A constellation of 15 LEO satellites is assumed.

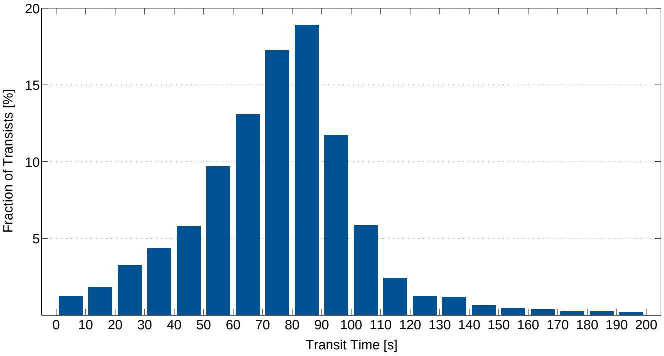

Figure 2.10: Distribution of spot beam transit times (spot beamwidth ∼ 1°).

- A Frequency Division Multiple Access (FDMA) scheme with frequency reuse among the spot beams shall be used. FDMA is favored in comparison to Code Division Multiple Access (CDMA) schemes, which lead to a large frequency bandwidth occupation, and Time Division Multiple Access (TDMA) schemes, which lead to high peak power during transmission. Figure 2.11 shows different FDMA frequency allocation schemes dependent on the frequency reuse distance D. D is determined by the maximum tolerable signal-to-interference ratio while the interference power is determined by the side lobe levels of the spot beams due to the characteristics of the antenna system. Since each spot beam is connected to a transponder which works in a fixed frequency band, FDMA is not possible during spot beam overlap. In that case the LEO satellites in the same spot beam shall share the frequency band applying a TDMA scheme.

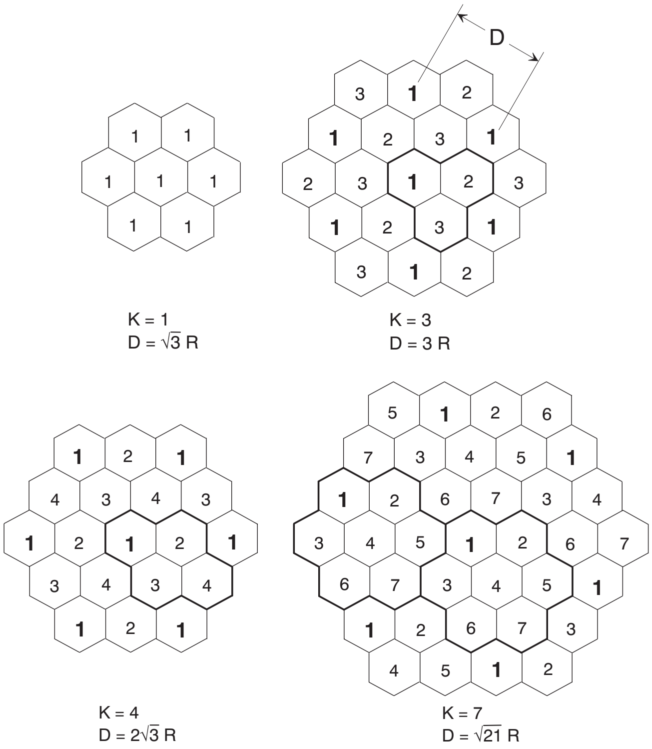

Figure 2.11: Spot beam structures with cluster sizes $K = 1$, 3, 4, and 7. D is the frequency reuse distance with R being the edge length of one hexagon. Numbers in spot beams denote the frequency bands. (*Figure adapted from Lutz et al. [2000].*)

- An adaptive modulation and coding scheme shall be applied, in order to adapt to the varying losses on the LEO-GEO-Earth link. The main dynamics in the losses of approximately 15 dB are due to atmospheric disturbances like rain fading on the GEO-Earth link (cf. Maral and Bousquet [2009]). The dynamics in the free space loss of the LEO-GEO ISLs are much smaller with approximately 1.5 dB.

- The LEO satellites shall take care of the signal conditioning. This includes a Doppler pre-compensation for frequency drifts on the LEO-GEO ISLs in order to match the RX LNA frequency bands on the GEO satellite. The hardware on the GEO satellite shall be kept as simple as possible.

- In addition to the dedicated payload downlink, a separate low data rate link shall be provided. Such a link can be used for TT&C services and only requires a data rate of $1 - 2$ Mbit/s. The communications system can be realized with an additional global horn antenna on the GEO satellite and LEO satellite. The 15 LEO satellites ideally share one transponder of 36 MHz on the GEO satellite using an FDMA scheme with approximately 2.3 MHz per ISL. An example for such a system is presented in Katona [2012] and will not be discussed further in this thesis.

2.3 Summary

The first section in this chapter analyzed important aspects about the LEO satellite orbit statistics and about the derived LEO-GEO contact times. The contact times formed the base for determining the required data rates of a geostationary data relay, in order to meet the demands of current and future LEO Satellite downlink capacities.

The supported number of satellites and the data-rates defined the requirements for the baseline communications concept. The main baseline parameters are summarized in Table 2.3.

The communications concept defines the requirements for the antenna subsystem, which are derived in the following chapter.

Baseline Design Parameter	
Number of concurrently served LEO satellites	15
Data rate for the ISLs	$30 - 100$ Mbit/s on the LEO-GEO ISLs
Frequency band for the ISLs	27 GHz in Ka-band
Bandwidth of the ISLs	36 MHz for each ISL
GEO satellite transponder design	Transparent, no onboard processing
GEO satellite antenna field of view	±10°
GEO satellite antenna spot beamwidth	1°
Number of spot beams	400
Multiple access scheme	FDMA; TDMA during spot beam overlap
Coding and modulation scheme	Adaptive coding and modulation
Doppler shift compensation	TX detuning on the LEO satellite

Table 2.3: The table shows the main baseline parameters of the communications concept for the geostationary data relay proposed in this thesis.

Chapter 3

Multibeam Antenna Concept for Geostationary Data Relays

3.1 GEO Satellite Antenna Requirements

In the previous chapter the communications concept for a geostationary data relay for intermediate data rates was defined. In this chapter the concept for the required GEO satellite onboard antenna system is developed. The system parameters derived from the communication architecture requirements are presented in the following section.

- The antenna shall be designed as a reflector setup which focuses radiation from different directions on separate spots (see Figure 3.1). The focal plane shall be covered with antenna elements like a phased array antenna, but only the antenna elements which are currently illuminated shall be active. This reduces the number of active RF channels to only the number of supported satellites, which is power efficient. The spatial separation of the signals corresponds to a multibeam structure in the field of view. Thus, the antenna system is able to cover a FOV of ±10° subdivided in 400 spot beams, where up to 15 spot beams concurrently shall receive signals.

  The alternative design to fulfill these requirements is a phased array antenna on the focal plane of a reflector setup (see Figure 3.1). It creates spot beams by adjusting the phases of its antenna elements. In order to receive 15 signals concurrently, the phases have to be adjusted digitally. The disadvantage of this approach are the required RF chains for each antenna element, which consume extra mass and power compared to the focusing solution. In addition, either an onboard processing unit is required or a large bandwidth on the downlink, in order to download the separate antenna element signals for post-processing on the ground. A direct radiating phased array antenna is also not an option since it requires even more antenna elements to create the same aperture as the reflector setup, which additionally increases the complexity.

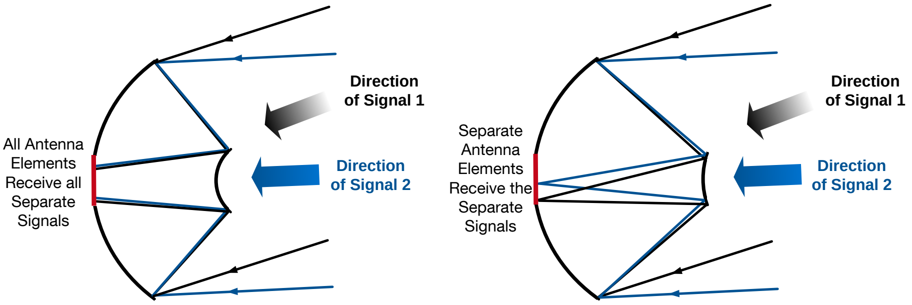

Figure 3.1: *Left side:* All elements on a phased array antenna are illuminated. *Right side:* Focusing radiation from different directions on separate spots on the antenna array enables spatial separation of the incoming signals.

- The GEO satellite antenna for the LEO-GEO ISLs shall provide an antenna gain of at least 31.0 dBi for achieving a data rate of 30 Mbit/s and an antenna gain of at least 40.1 dBi for achieving a data rate of 100 Mbit/s. Assumed are LEO satellites with a TX reflector antenna of 0.5 m in diameter and a transmit power of 50 W. Table 3.1 shows the according link budget. (For details about the link budget calculation see Appendix A.)

	30 Mbit/s	100 Mbit/s
Uplink: LEO-GEO		
Carrier Frequency	27.0 GHz	
Carrier Bandwidth	36.0 MHz	
LEO TX Antenna Diameter	0.5 m	
LEO TX Antenna Gain	40.8 dBi	
LEO TX Power	50.0 W	
LEO EIRP	56.8 dBW	
Worst Case Free Space Loss	213.4 dB	
GEO RX Antenna Gain	31.0 dBi	40.1 dBi
GEO RX System Noise Temperature	550 K	
GEO RX G/T	2.6 dB/K	11.7 dB/K
C/N_0	74.6 dBHz	83.9 dBHz
Downlink: GEO-Earth		
Carrier Frequency	27.0 GHz	
Carrier Bandwidth	36.0 MHz	
GEO TX Antenna Diameter	0.8 m	
GEO TX Antenna Gain	44.9 dBi	
GEO TX Power	25.0 W	
GEO EIRP	57.9 dBW	
Free Space Loss	212.7 dB	
Atmospheric Loss	1.4 dB	
Rain Loss (99.9% availability)	13.4 dB	
Ground RX Antenna Diameter	5.0 m	
Ground RX Gain	60.8 dBi	
Ground RX System Noise Temperature	380 K	
Ground RX G/T	34.0 dB/K	
C/N_0	93.0 dBHz	
Overall C/N_0	74.5 dBHz	83.3 dBHz
Required C/N_0 for 30/100 Mbit/s	74.5 dBHz	83.3 dBHz

Table 3.1: Exemplary link budget for a geostationary data relay above Europe and a ground station located in Munich, Germany.

- The antenna focal plane shall be covered with patch antenna elements on a Printed Circuit Board (PCB), in order to reduce weight and space.

- An RF switch unit shall be used to route signals received by the different patch antenna elements to the transponders. The number of switch unit output channels shall match the number of transponders corresponding to the number of supported LEO satellites.

- The switches shall consist of Micro Electromechanical System (MEMS), in order to save weight, space and power. They also provide low signal losses.

- The switch unit shall be located directly behind the patch antenna PCB, in order to avoid long and heavy harnesses. The switch unit shall be kept thermally stable, in order to avoid damaging of the RF-MEMS switches.

- The antenna shall either be located on the Earth deck (plane facing the Earth) or at one of the two side decks not containing the solar panels. Due to weight restrictions limiting the length of cables, only a dual reflector design is realizable on the Earth deck. At the side decks an offset reflector setup seems most promising. The two possible designs are visualized in Figure 3.2.

  The dual reflector design on the Earth deck is selected as the baseline design in this thesis. The reasons are explained in the next section.

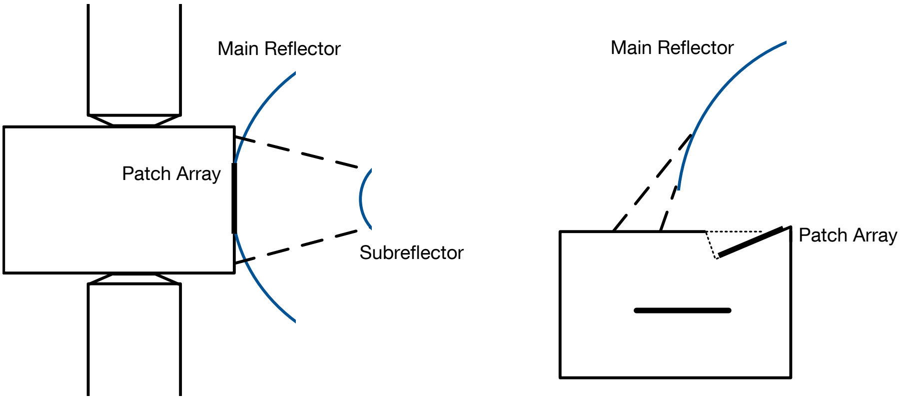

Figure 3.2: Two possible designs for the reflector setup: *Left:* Dual-reflector center aligned antenna mounted on the Earth deck. *Right:* Single reflector offset antenna mounted on one of the side decks.

3.2 Reflector Setup

3.2.1 Characteristics of Imaging Systems

The reflector setup of the new antenna system for the geostationary data relay has the task to focus radiation from separate directions within the field of view of ±10° on separate foci. A parabolic single reflector system, usually the choice for directive communication antennas, only focuses paraxial radiation as described later. It is therefore not suited for this application. Thus, a more sophisticated reflector setup is necessary. In order to determine a setup with the required abilities, a closer look into geometrical optics is helpful. The relation between the wavelength of Ka-band signals (1 cm) and the size of the reflectors implies that geometrical optics is a good approximation.

An ideal optical system fulfills the requirement of focusing radiation from different directions on separate spots. But image-forming systems in general can suffer from different aberrations, i.e. imaging errors, based on deviations from ideal optical systems. The main aberrations for monochromatic rays are the five so called *Seidel Aberrations*, introduced 1857 in a paper by Philipp Ludwig von Seidel. They can be expressed with the help of third-order optics, the so called *Seidel Optics*, where optical systems are described by a series expansion truncated after the third order (cf. Born and Wolf [1959]). The five aberrations are *Spherical Aberration*, *Coma*, *Astigmatism*, *Curvature of Field* and *Distortion*. Figure 3.3 illustrates the different effects.

A spherical reflector, for example, shows *Spherical Aberration*, i.e. paraxial rays with different distances to the optical axis are focused on different points and therefore form a blurred focal spot. A parabolic reflector compensates for *Spherical Aberration*. It is typically used to focus paraxial wave fronts in communication applications. However, a parabolic reflector suffers from *Coma* leading to a blurred focal point for non-paraxial rays in geometrical optics description or correspondingly to a lower gain and higher side lobes in electromagnetic description. A ray-tracing simulation as well as an electromagnetic field simulation are used to visualize the consequences of *Coma* for a parabolic reflector in Figure 3.4 and 3.5.

Imaging systems with neither *Spherical Aberration* nor *Coma* are called *Aplanats* (see also Allen [1975]). Aplanatic reflector designs are feasible by a dual-reflector setup as developed by Schwarzschild in 1905, Chrétien in 1922 and Maksutov in 1932 (see also Terebizh [2005]). Descriptions and underlying theory are additionally found in Wetherell and Rimmer [1972], Wyman and Korsch [1974] and Granet [2006]. Imaging systems able to compensate for *Spherical Aberration*, *Coma* and *Astigmatism* are called *Anastigmats*.

Since *Curvature of Field* and *Distortion* is not harming the focusing of radiation, but only displaces the separate focal points, an anastigmatic reflector setup regarding theoretical aspects is the favored design. However, with a raising number of aberration compensations, the number of side conditions increases. Consequently, the degree of freedom in the design parameters becomes more and more restricted. In the following section, the possible reflector designs are investigated.

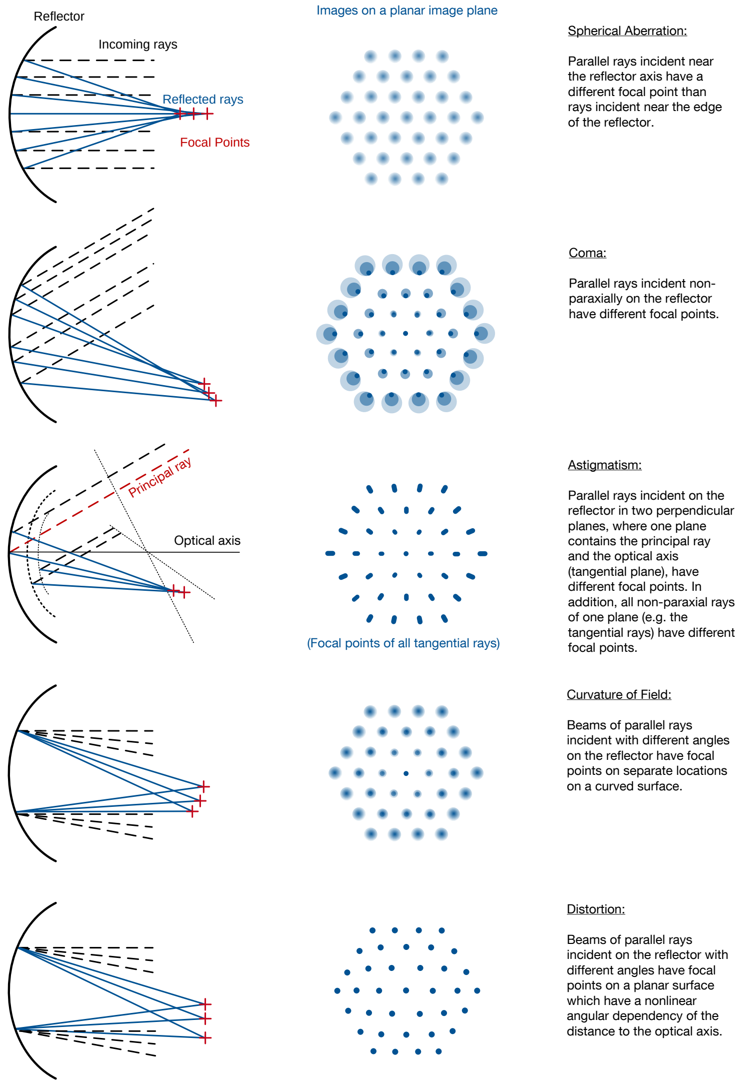

Spherical Aberration:

Parallel rays incident near the reflector axis have a different focal point than rays incident near the edge of the reflector.

Coma:

Parallel rays incident non-paraxially on the reflector have different focal points.

Astigmatism:

Parallel rays incident on the reflector in two perpendicular planes, where one plane contains the principal ray and the optical axis (tangential plane), have different focal points. In addition, all non-paraxial rays of one plane (e.g. the tangential rays) have different focal points.

Curvature of Field:

Beams of parallel rays incident with different angles on the reflector have focal points on separate locations on a curved surface.

Distortion:

Beams of parallel rays incident on the reflector with different angles have focal points on a planar surface which have a nonlinear angular dependency of the distance to the optical axis.

Figure 3.3: The figures on the right show images of signal sources on a hexagonal grid in the far field of a reflector. The images are distorted by the five *Seidel Aberrations* when not compensated for by the reflector. The figures on the left show the optical paths of exemplary rays leading to the distorted images. *(Illustration ideas adopted from MacEvoy [2013] and Savard [2013].)*

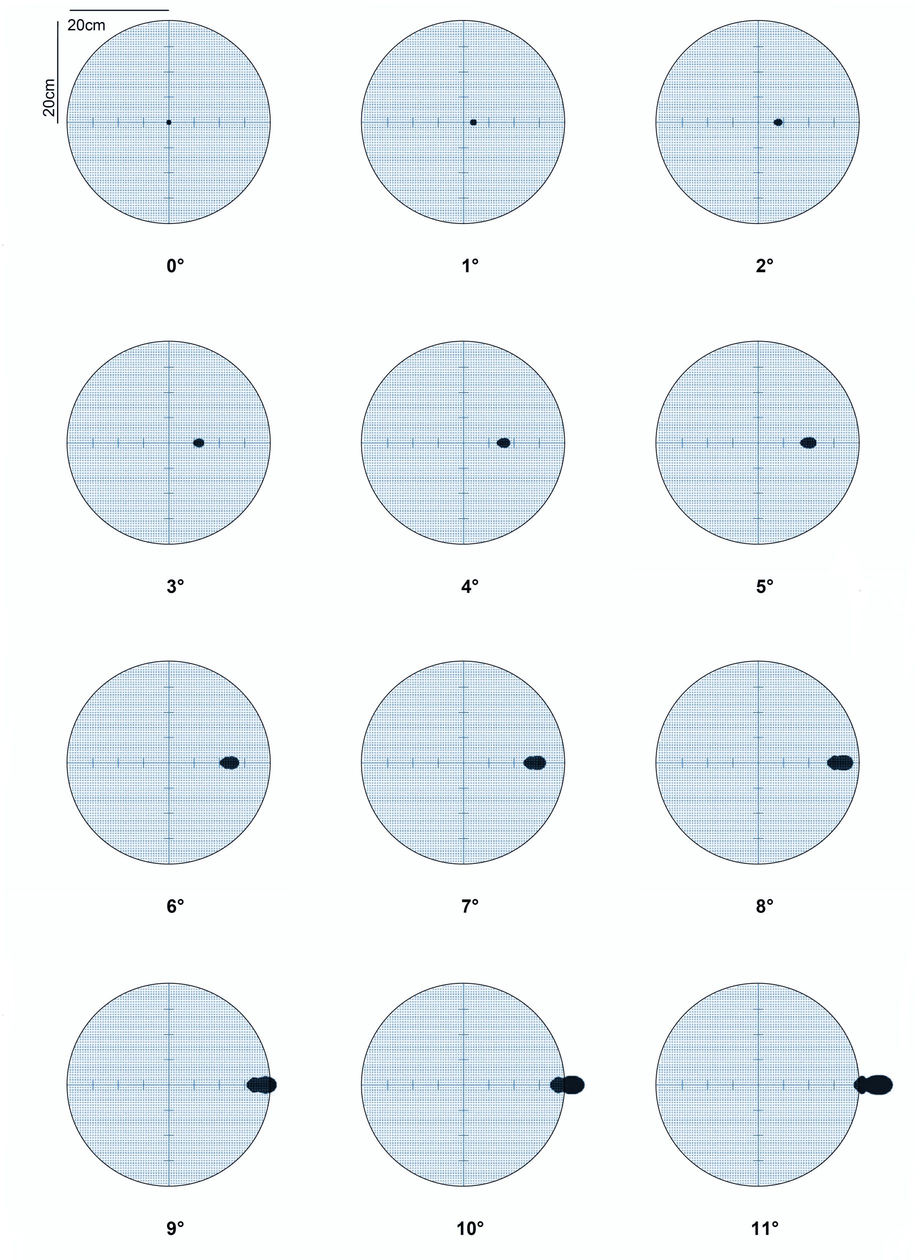

Figure 3.4: Ray-tracing code simulation: Aberrations (mainly *Coma*) blur the image on the focal plane of a parabolic dual-reflector with raising angle of the incoming rays to the reflector axis.

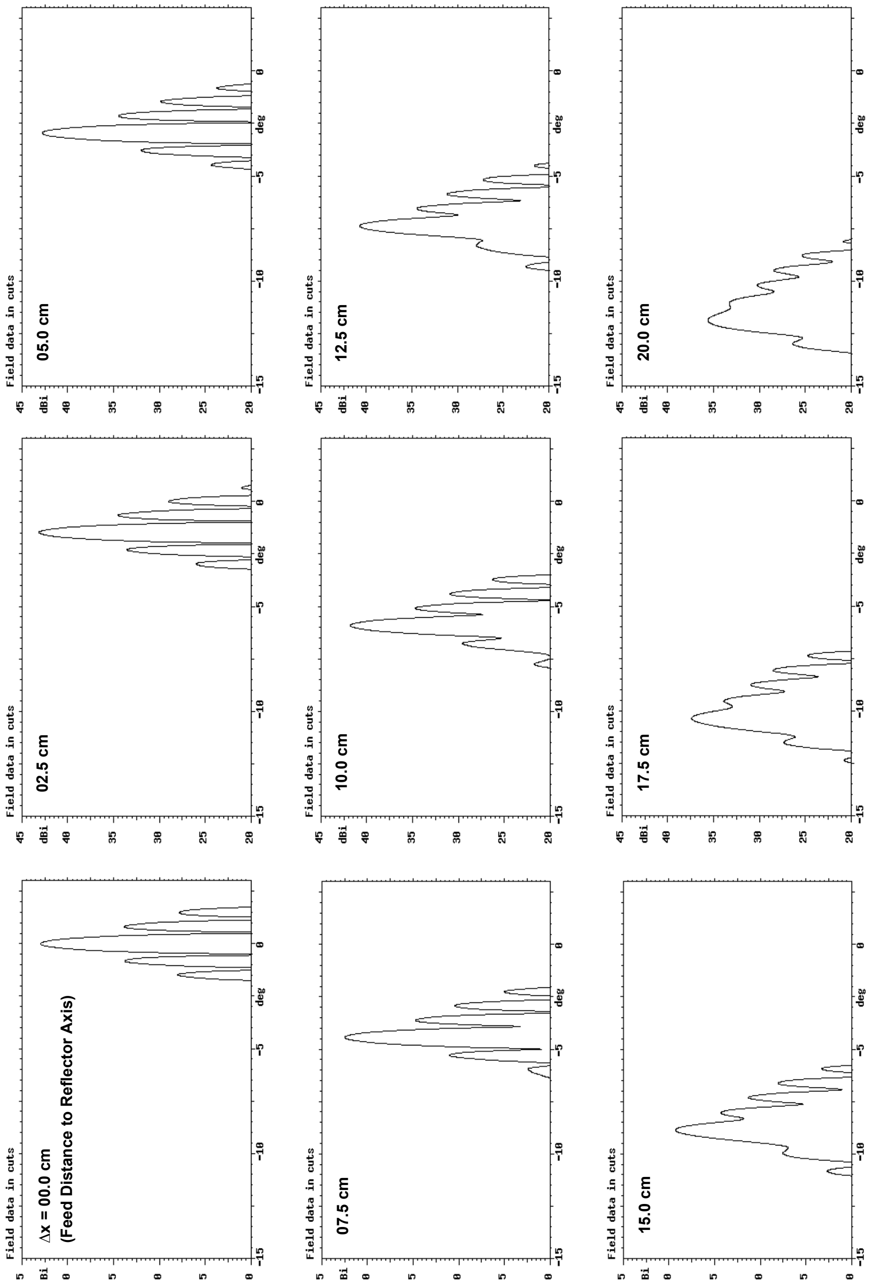

Figure 3.5: Electromagnetic field simulation: Aberrations (mainly *Coma*) lead to a decline in gain and an increase of the side lobes of a parabolic reflector antenna with raising angle of the incoming rays to the reflector axis.

3.2.2 Anastigmatic and Aplanatic Reflector Designs

The reflector setup for the geostationary data relay antenna system is determined by four main design parameters. The usual choice for the set is the diameter of the primary reflector D_p, the vertex back focus B, the primary focal ratio $F_\mathrm{p} = f_\mathrm{p}/D_\mathrm{p}$, with f_p the primary focal lenght, and the system focal ratio F (cf. Wetherell and Rimmer [1972]). While the first two parameters D_p and B are directly related to the dimensions of the reflector setup (see Figure 3.6), the influence of the last two parameters is only indirectly visible. They determine the dimensions of the distance between the primary and secondary reflector S, the secondary focal length f_s and the diameter of the secondary reflector D_s and of the focal plane D_I, while the last two are additionally dependent on the field of view θ_I. The mathematical expressions for the values are shown in Equations (3.6) to (3.9).

In mathematical descriptions of dual-reflector designs, especially in astrophysics, the additional normalized parameters $\eta = B/D_\mathrm{p}$, $\beta = B/f_\mathrm{p}$ and the magnification $m = F/F_\mathrm{p}$ are used.

In Section 3.2.1, an anastigmatic reflector setup was determined as the optimum design concerning imaging properties. Wetherell and Rimmer [1972] show that the condition for anastigmatic two-reflector designs is fulfilled when $\beta = -\left(2m^2 + m\right)$. This limits the set of design parameters while practical restrictions due to the realization and manufacturing have to be taken into account:

- $m > 0.5$ leads to virtual images and therefore, such a solution is not applicable for real imaging systems.
- For $m < 0$, the primary reflector becomes convex. An example is the so called concentric *Schwarzschild* reflector setup (cf. Figure 3.6). In order to achieve a sufficient aperture, such a design would exceed realizable dimensions for space antennas.
- $0 < m < 0.5$ are so called *Couder* reflector setups similar to *Cassgrain* types, but with a concave secondary reflector (cf. Figure 3.6). However, β becomes negative and therefore the focal plane is located between both reflectors. Such a setup is not favorable as the backside of the antenna array could not be located inside the satellite's thermal shield and signal paths to the transponders become long.

All alternatives for anastigmatic reflector designs would require three or more reflectors, which are not feasible due to the complexity of such designs and the losses at each reflection (see Cook [1981] and Frosch [1978]).

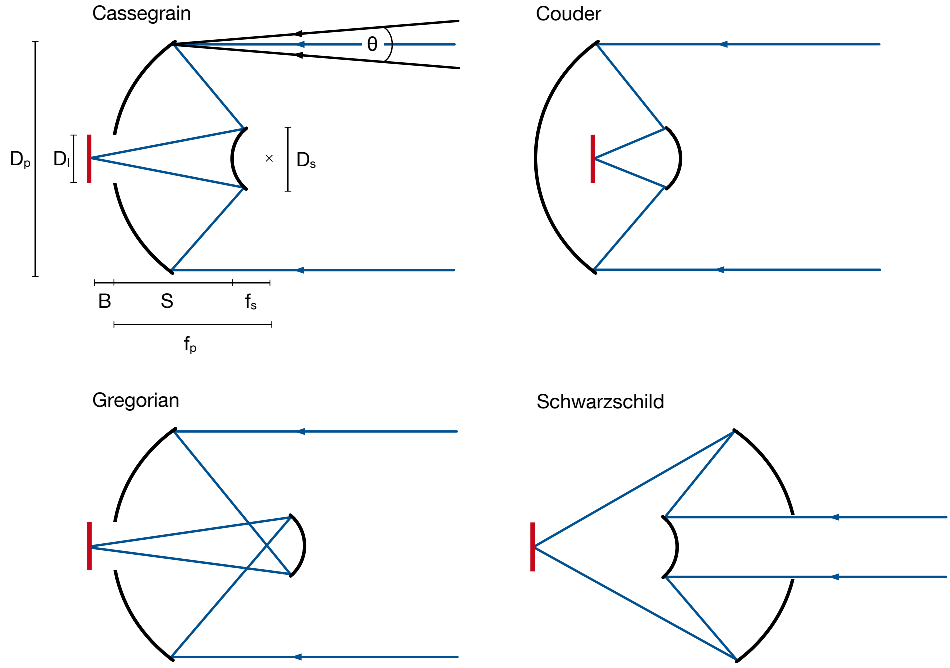

Figure 3.6: Examples of four different design types of dual-reflector setups. The *Cassegrain* type has a concave primary reflector and a convex secondary reflector, where the secondary reflector lies between the primary reflector and the primary focal point. The *Gregorian* type has a concave secondary reflector, where the secondary reflector lies on the opposite side of the primary focal point. The *Couder* type is similar to the *Cassegrain* type, but with a concave secondary reflector. The focal point lies between the reflectors. The concentric *Schwarzschild* type has a larger concave secondary reflector than the primary reflector and a hole through which the incoming radiation passes. The primary reflector is convex. The *Cassegrain* type also shows the nomenclature of the main design parameters for a dual-reflector setup.

Anastigmatic designs are not feasible due to practical restrictions. Therefore, at least *Spherical Aberration* and *Coma* shall be excluded by applying an aplanatic design. *Aplanats* can be categorized in three main design types: *Cassegrain*, *Gregorian* and *Schwarzschild*.

The *Schwarzschild* type faces similar problems as the anastigmatic *Couder* reflector setup, where the focal plane is located between both reflectors.

In the *Gregorian* design the secondary reflector is located after the prime focus, while for the *Cassegrain* type the secondary reflector is located before the prime focus (see Figure 3.6). This leads to a longer design of the *Gregorian* type. Therefore, the *Cassegrain* type is the favored reflector setup.

The *Cassegrain* version of an aplanatic two-reflector setup was developed by George Willis Ritchey and Henri Chrétien in the beginning of the 20th century and is since known as *Ritchey-Chrétien* design. The mathematical description for dual-reflector setups is provided by Wetherell and Rimmer [1972]. Under the assumption that only third-order aberrations are considered, the aspheric surfaces of the reflectors form conic sections (see also Schroeder [2000]). The sag is described by

$$z(r) = \frac{cr^2}{\left(1 + \sqrt{1 - \kappa c^2 r^2}\right)}, \tag{3.1}$$

where $z(r)$ is the distance of the surface from a plane tangent to its vertex as a function of the radial distance r from the optical axis. $z(r)$ is parametrized by the conic constant κ and the vertex curvature c. Schroeder [2000] shows that the vertex curvature of the primary reflector c_{p} and the secondary reflector c_{s} are

$$c_{\mathrm{p}} = -\frac{1}{2D_{\mathrm{p}}F_{\mathrm{p}}} \tag{3.2}$$

and

$$c_{\mathrm{s}} = \frac{\left(1 - m^2\right)}{2mD_{\mathrm{p}}\left(F_{\mathrm{p}} + \eta\right)}. \tag{3.3}$$

The conic sections depend on the type of the two-reflector system. In general they are categorized as follows

$\kappa < 0$	hyperboloid
$\kappa = 0$	paraboloid
$0 < \kappa < 1$	prolate ellipsoid
$\kappa = 1$	sphere
$\kappa > 1$	oblate spheroid

The conic sections of the primary and secondary reflector for the *Ritchey-Chrétien* reflector setup are derived in Wetherell and Rimmer [1972]:

$$\kappa_\mathrm{p} = \frac{-2\left(F_\mathrm{p} + \eta\right)}{m^2\left(F - \eta\right)} \tag{3.4}$$

and

$$\kappa_\mathrm{s} = -\left[\frac{2F\left(m+1\right)}{\left(m-1\right)^3\left(F-\eta\right)} + \frac{4m}{\left(m-1\right)^2}\right]. \tag{3.5}$$

Both κ_p and κ_s are smaller than zero and therefore have hyperbolic shapes.

The distance S from secondary to primary reflector is described by

$$S = \frac{D_\mathrm{p}\left(F - \eta\right)}{m+1}. \tag{3.6}$$

The secondary focal length f_s is determined by

$$f_\mathrm{s} = \frac{FD_\mathrm{p}(f_\mathrm{p} - S)}{f_\mathrm{p} + FD_\mathrm{p}}. \tag{3.7}$$

The diameter of the focal plane at a field of view comprising θ_i is calculated by

$$D_\mathrm{I} = \theta_\mathrm{i} F D_\mathrm{p}. \tag{3.8}$$

and the diameter of the secondary reflector by

$$D_\mathrm{s} = \frac{D_\mathrm{p}\left(F_\mathrm{p} + \eta + \theta_\mathrm{i} F_\mathrm{p}\left|F - \eta\right|\right)}{F + F_\mathrm{p}}, \tag{3.9}$$

with the field of view θ_i.

Aplanatic systems only cancel *Spherical Aberration* and *Coma*. Therefore, the systems suffer from *Curvature of Field*, which requires a curved antenna array. The theoretical sag of the best focus image surface with minimum wavefront error (compromise between *Astigmatism* and defocus) is described by

$$z_\mathrm{I}\left(r\right) = r^2/2R_\mathrm{I}, \tag{3.10}$$

with $R_\mathrm{I} = -mD_\mathrm{p}F\left(F_\mathrm{p} + \eta\right)/\left[m^2\left(F + F_\mathrm{p} - \eta\right) + \eta\right]$.

Since curved PCBs are not yet space approved concerning mechanical stress and thermal tensions, a method to apply a flat PCB is presented in Section 3.3.

After the theoretical determination of the baseline reflector setup, the quantitative determination of the optimum design parameters has to be performed. The field of view $\theta_\mathrm{I} = 20°$ is fixed by the antenna requirements. D_p, F_p, F and B for the *Ritchey-Chrétien* reflector setup are determined in the following paragraph.

The primary reflector diameter D_p is derived from the effective aperture of the antenna required to reach a gain of 31.0 to 40.1 dBi. The effective aperture is defined by the aperture of the primary reflector subtracted by either the aperture of the secondary reflector, i.e. blockage, or the area of the focal plane D_I, dependent on which of them shadows the primary reflector more. Thereby, also the shadowing of non-paraxially radiation has to be considered. A primary reflector with diameter of $D_\mathrm{p} = 1.2$ m is selected as a baseline. It provides a theoretical gain of approximately 48 dBi, where 3 to 6 dB losses are considered for blockage and spill-over effects, i.e. when radiation is not optimally hitting the reflectors and radiation spills over the reflector surface, e.g. due to high side-lobe levels.

The back focal length B shall be close to zero, in order to be able to thermally connect a cooling plate containing the antenna array with the primary reflector. This enables an efficient heat dissipation using the primary reflector as a radiator. In addition, the hole in the primary reflector is reduced to a minimum.

The remaining design parameters F_p and F are determined by a trade-off. Since the value f_p gives a better impression about the design dimensions than the normalized value F_p, f_p is used in the trade-off considerations. Figure 3.7 shows the evolution of the theoretical antenna gain defined by the effective aperture in dependency of the system focal ratio F and the primary focal length f_p at a fixed D_p of 1.2 m. According to Equation (3.8), the image surface diameter D_I is independent of f_p. Therefore, all curves converge to a joint curve when $D_\mathrm{I} \geq D_\mathrm{s}$.

Figure 3.8 shows the evolution of the image surface diameter D_I in dependency of F for fixed $D_\mathrm{p} = 1.2$ m and $\theta_\mathrm{I} = 20°$ according to the Antenna Subsystem Requirements (cf. Section 3.1). A small image surface diameter leads to a smaller number of antenna elements and larger aperture of the primary reflector and is therefore favorable. Figure 3.9 shows the evolution of the secondary reflector distance to the vertex S in dependency of the system focal length F and the primary focal length f_p at a fixed D_p of 1.2 m. After a trade-off between the image surface diameter D_I and the secondary reflector distance to the vertex S on the one side and the achievable antenna gain on the other side, a system focal ratio of $F = 0.7$ was selected.

Figure 3.10 shows the sag for $D_\mathrm{p} = 1.2$ m and $F = 0.7$ m in dependency of f_p. The image surface curvature can only be compensated effectively for a small sag as described in Section 3.3. After a trade-off between the image surface curvature and the effective aperture, the primary focal length f_p was selected to 0.7 m.

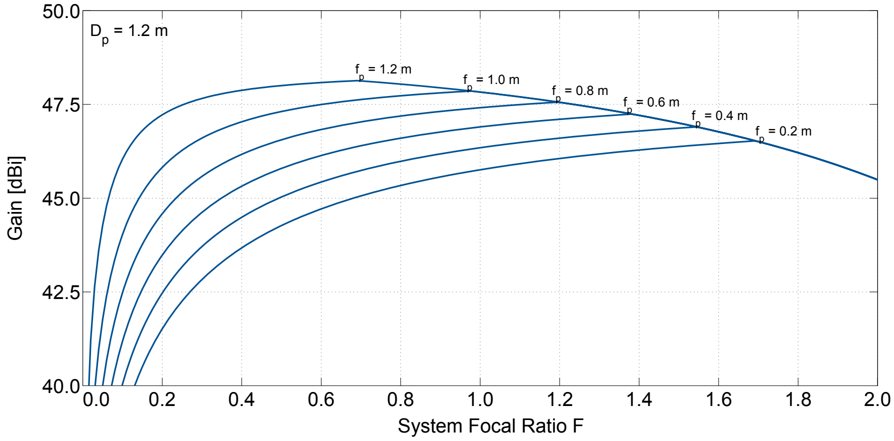

Figure 3.7: The theoretical antenna gain defined by the effective aperture in dependency of the system focal ratio F and the primary focal length f_p at a fixed primary reflector diameter D_p of 1.2 m. Since D_I is independent of f_p all curves converge to a joint curve when $D_\mathrm{I} \geq D_\mathrm{s}$.

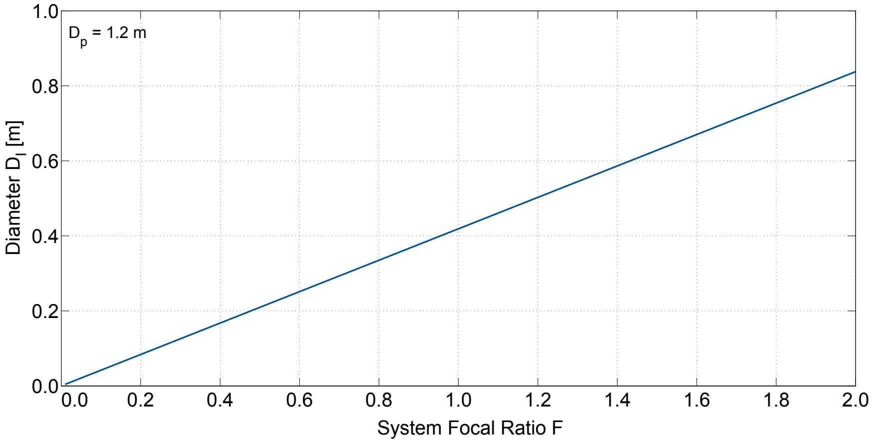

Figure 3.8: Evolution of D_I in dependency of the system focal length F at a fixed primary reflector diameter D_p of 1.2 m.

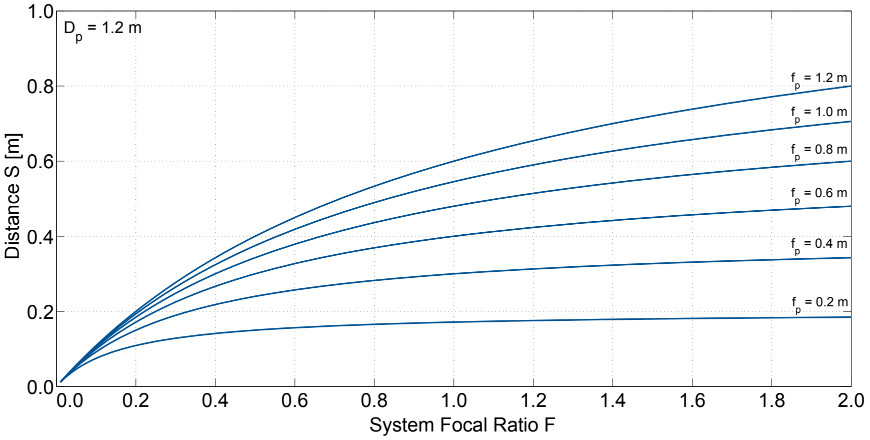

Figure 3.9: The secondary reflector to vertex distance S in dependency of the system focal length F and the primary focal length f_p at a fixed primary reflector diameter D_p of 1.2 m.

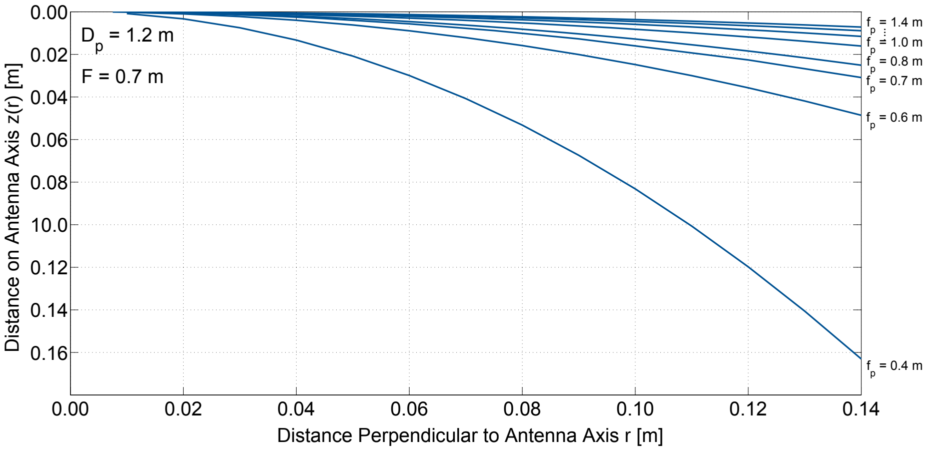

Figure 3.10: Curvature of the image surface for a *Ritchey-Chrétien* reflector setup with system focal ratio $F = 0.7$ and primary reflector diameter of $D_\mathrm{p} = 1.2$ m in dependency of the primary focal length f_p.

The baseline parameters and the derived antenna dimensions for the *Ritchey-Chrétien* setup are recapitulated in Table 3.2. In addition, the parameters for a comparable *Cassegrain* reflector setup (parabolic primary reflector, hyperbolic secondary reflector) are shown, which serves as a benchmark design for the simulations.

Design Parameter	*Ritchey-Chrétien*	*Cassegrain*
Image Surface Diameter	$D_\mathrm{I} = 0.29$ m	$D_\mathrm{I} = 0.29$ m
Primary Reflector Diameter	$D_\mathrm{P} = 1.20$ m	$D_\mathrm{P} = 1.20$ m
Primary Focal Length	$f_\mathrm{P} = 0.70$ m	$f_\mathrm{P} = 0.70$ m
System Focal Ratio	$F = 0.70$	F = 0.70
Secondary Reflector Diameter	$D_\mathrm{s} = 0.40$ m[a]	$D_\mathrm{s} = 0.70$ m
Secondary Reflector Focal Length	$f_\mathrm{s} = 0.40$ m	$f_\mathrm{s} = 0.70$ m
Secondary Reflector Vertex Distance	$S = 0.40$ m	$S = 0.70$ m
Vertex Back Focus	$B = 0.00$ m	$B = 0.00$ m

---

[a] The theoretically determined secondary reflector diameter according to Equation (3.6) would be $D_\mathrm{s} = 0.74$ m. However, a trade-off between blockage and spill-over showed an optimized secondary reflector diameter of 40 cm for maximum gain at the rim of the field of view.

Table 3.2: Parameter set for the *Ritchey-Chrétien* setup and a *Cassegrain* reflector setup which shall serve as a benchmark design later on.

3.3 Patch Antenna Array

According to the requirements in Section 3.1, the reflector setup shall focus radiation from different directions on separate spots in the focal plane. There, the radiation is received by antenna elements. Section 2.2 shows that a multibeam coverage of ±10° leads to approximately 400 antenna elements while providing 1° spot beamwidths. A realization with horn or helix antennas would result in > 30 kg for the antenna array assuming a weight of minimum 75 g per antenna element. Such a solution is not practicable. Therefore, a Printed Circuit Board (PCB) including patch antenna elements shall be used. It only weights approximately $1 - 2$ kg in total. In addition, a PCB consumes little space as RF circuits can be integrated on a multilayer board of a few millimeters thickness only. Figure 3.11 shows a 4x4 patch array on a Rogers RT/duroid 6002 high frequency laminate developed at the Institute for Communications and Navigation at the German Aerospace Center (DLR).

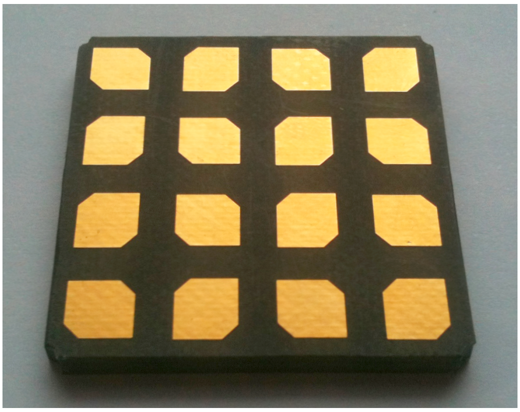

Figure 3.11: Exemplary 4x4 Ka-band patch array on a Rogers RT/duroid high frequency laminate developed at the Institute of Communications and Navigation at the German Aerospace Center (DLR).

The *Ritchey-Chrétien* reflector setup produces a curved focal plane as derived in Section 3.2.2. Curved PCBs are difficult to manufacture by state of the art technology and not yet space approved. In addition, curved PCBs consume more space than flat PCBs. Therefore, the curved PCB shall be substituted by a flat PCB, but shall provide a similar radiation pattern. In order to achieve a similar radiation pattern, a tilt in the direction of the radiation of the single elements has to be introduced. In addition, the spacing between the elements as well as the distance of the PCB to the reflector vertex has to be adjusted by a trade-off between defocus of the center antenna elements and the edge antenna elements (see Figure 3.12). It has to be considered that the edge antenna elements are occupied more frequently and therefore shall be privileged (see Section 2.2).

A single patch element can not be steered electronically, but a 2x2 array of patch elements can be steered by adjusting the phases of the single array element signals. The phase shifts can be created in the copper layer of the PCB by microstrip delay lines (cf. Pillans et al. [1999b]). Figure 3.13 shows an electromagnetic simulation of an antenna element on a curved array and an antenna element on a flat array with beamforming. The beamforming is only extended to provide the maximum gain in the desired radiation direction of 28°. The loss in gain compared to a curved array is approximately 1.5 dB for an edge antenna element.

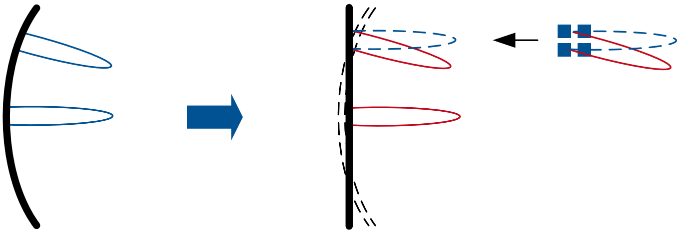

Figure 3.12: A 2x2 sub-array of patch elements enables a steering of the beam (*right side*). A curved PCB can be approximated by a flat PCB. The distance of the flat array to the primary reflector vertex is a compromise between defocus of the center antenna elements and defocus of the edge antenna elements.

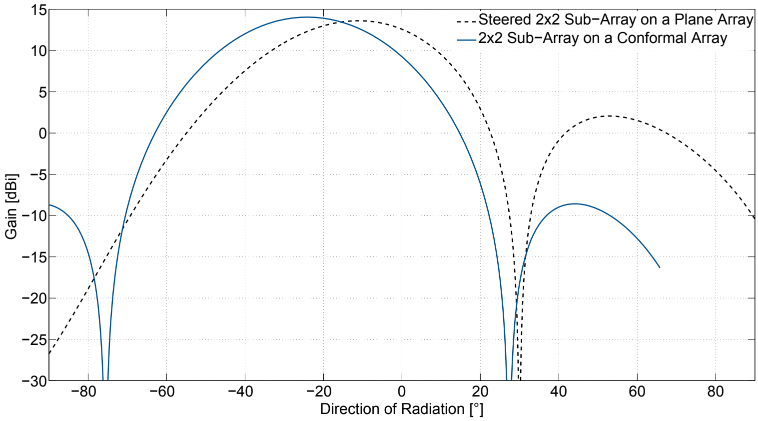

Figure 3.13: Simulation of an antenna element on a curved array and an antenna element on a flat array. The phase-shifts were adjusted, in order to reach the optimum gain at the desired beam direction of 26° in the dual-reflector setup. A further steering would have reduced the gain. The loss in gain in comparison to the curved PCB is approximately 1.5 dB.

Using 2x2 sub-arrays provides another advantage in addition to the steering ability. They produce a more efficient illumination taper for a dual-reflector setup compared to a single patch element, which reduces spill-over losses. The characteristics of the applied patch antennas are simulated with TICRA GRASP based on the following parameter set: Diameter $d = 59$ mm (simulated as a circular antenna), thickness $h = 3.0$ mm, dielectric constant $\epsilon_{\mathrm{r}} = 6.0$. Figure 3.14 shows the gain profile of a 2x2 sub-array with spacing of $0.7 \cdot \lambda$ in comparison to a single patch antenna.

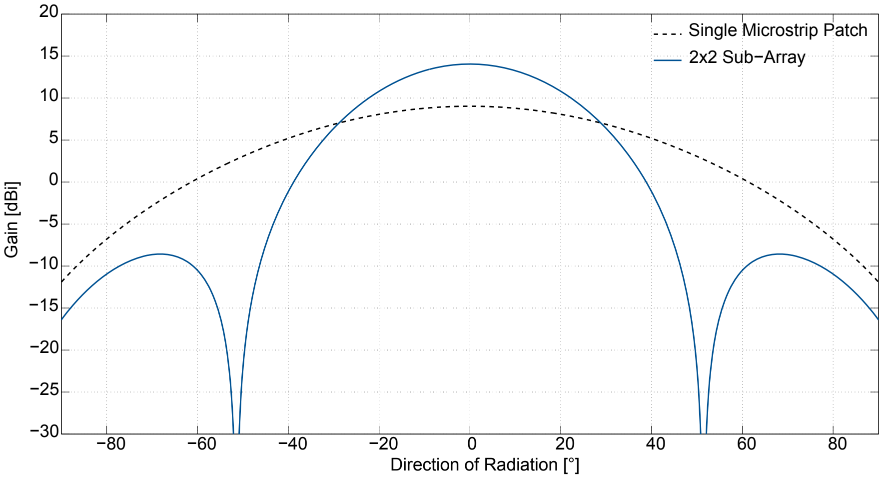

Figure 3.14: Gain of a single aperture coupled microstrip patch antenna (dashed black line) and a 2x2 sub-array (blue line). The $\theta_{3\mathrm{dB}}$ beamwidth is much smaller for the 2x2 sub-array and reaches approximately 40°.

The 2x2 sub-arrays are distributed on a hexagonal grid to evenly cover the focal plane (see Figure 3.15). The spacing a between the 2x2 sub-arrays shall be as close as possible, in order to avoid gaps in the gain profile. The minimum a is determined by the minimum distance the patch antennas can be placed to each other. Negative effects due to mutual coupling between the 2x2 sub-arrays shall be reduced by implementing fencing vias (cf. Bahl [2003]).

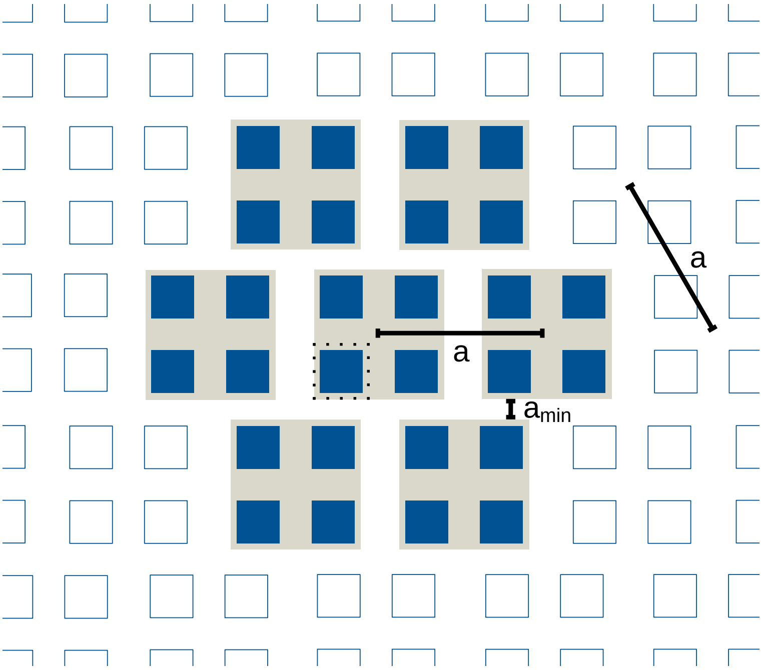

Figure 3.15: Hexagonal distribution of 2x2 sub-arrays on the PCB. The minimum grid size a is determined by minimum distance a_{min} the patch antennas can have. A via fencing, indicated by black dots around one element in the center, reduces mutual coupling between the sub-arrays.

3.4 Simulation and Results

The electromagnetic simulations of the antennas are performed with TICRA GRASP, a software specialized on reflector antennas. Physical optics methods and physical theory of diffraction are used to calculate the field distribution. Particular effects due to surface inaccuracies, blockage by the fixing, mutual coupling, ohmic and impedance mismatch losses or manufacturing tolerances of the setup are not considered in this simulation.

The *Ritchey-Chrétien* antenna was optimized considering the gain of the antenna elements at the rim of the antenna array. A trade-off between blockage and spill-over showed that a secondary reflector diameter of $D_\mathrm{s} = 40$ cm leads to the best results. The flat antenna array is shifted to 6.5 cm distance from the reflector vertex, in order to compensate for the missing curvature. Microstrip patches forming 2x2 sub-arrays as shown in Figure 3.14 are applied as antenna elements.

The optimized *Ritchey-Chrétien* antenna shall be compared to a benchmark setup. Therefore, a *Cassegrain* setup with equal primary reflector diameter $D_\mathrm{p} = 1.20$ m, image surface diameter $D_\mathrm{I} = 0.29$ m and secondary reflector diameter $D_\mathrm{s} = 0.70$ m, is simulated. Table 3.2 shows an overview of the parameters. In addition, single patch antennas are used as antenna elements, in order to compare the spill-over losses between single patch antennas and 2x2 sub-arrays.

The simulation results are shown in Figure 3.16 and Figures 3.17 and 3.18 as well as in Table 3.3. The simulation in Figure 3.18 was performed with a flat array and steered 2x2 sub-arrays while the simulations of one quarter of the full antenna array of the *Ritchey-Chrétien* setup are only performed with curved antenna arrays for complexity reasons.

The *Cassegrain* setup shows a steep decline in gain along the radial direction caused by the uncompensated aberrations, mainly *Coma*, for non-paraxial radiation. Since the secondary reflector diameter has to be much larger than for the *Ritchey-Chrétien* setup, in order to avoid large spill-over losses, the blockage is higher.

In comparison, the *Ritchey-Chrétien* setup with curved antenna array reduces the decline in gain in radial direction to only 0.7 dB due to the compensation of *Coma*. The 2x2 sub-arrays enable a more efficient illumination of the secondary reflector than single patch antennas, which reduces the spill-over. The loss in gain applying a flat antenna array instead of a curved antenna array is approximately $1.0 - 1.5$ dB and therefore matches the loss seen in the antenna element comparison in Figure 3.13.

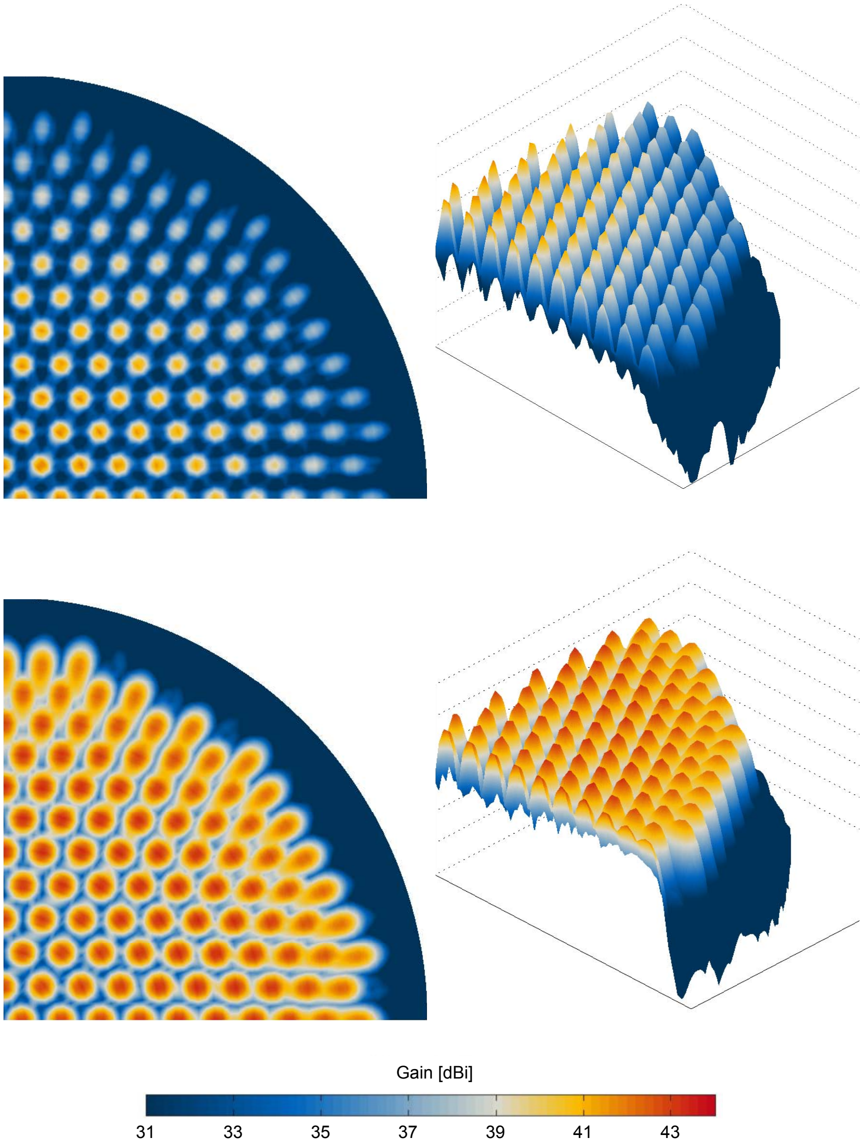

Figure 3.16: Visualization of one quarter of the simulated antenna gain for a *Cassegrain* reflector setup with single patch antennas (top) and a *Ritchey-Chrétien* reflector setup with fixed 2x2 sub-arrays on a curved array (bottom). The *Cassegrain* antenna is characterized by a steep radial decline in gain due to uncompensated aberrations and spill-over. The aplanatic *Ritchey-Chrétien* antenna compensates for the radial decline in gain. The 2x2 sub-arrays lead to an increase in spot beam gain as the secondary reflector illumination is more efficient.

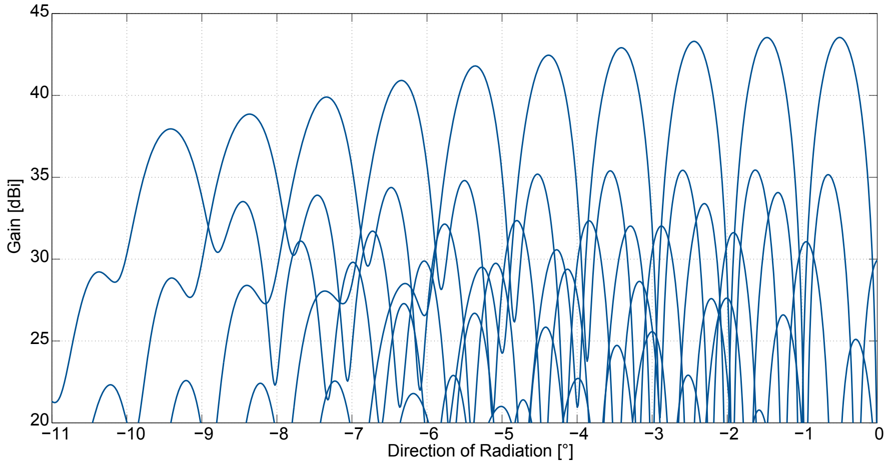

Figure 3.17: Radial cut through the gain profile of the *Cassegrain* reflector setup with single microstrip patch antenna elements.

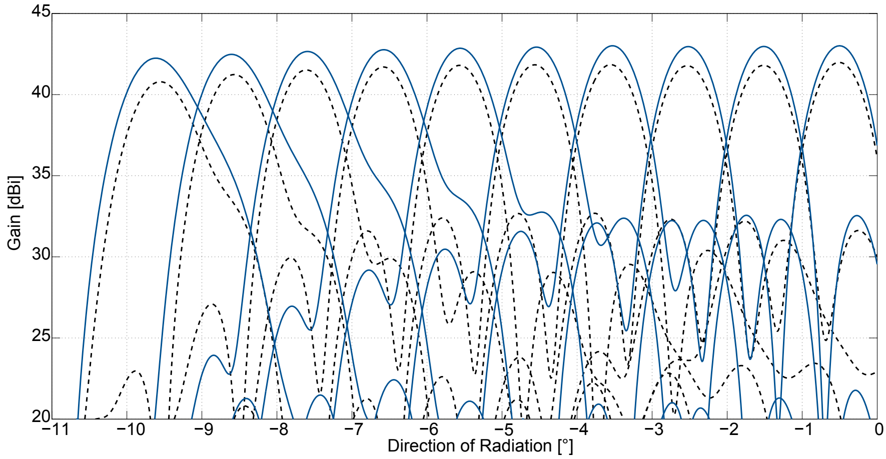

Figure 3.18: Radial cut through the gain profile of the aplanatic *Ritchey-Chrétien* reflector setup with fixed 2x2 microstrip patch sub-arrays. The blue line shows the gain profile for a curved antenna array. The black dashed line shows the gain profile for a flat array with steered 2x2 sub-arrays. The loss in gain for the flat antenna array is approximately 1.0 – 1.5 dB.

Center Antenna Element	*Cassegrain*	*Ritchey-Chrétien* (curved PCB)	*Ritchey-Chrétien* (flat PCB)
Spill-over Antenna Element	1.4 dB	1.0 dB	0.7 dB
Spill-over Secondary Reflector	2.2 dB	2.5 dB	2.3 dB
Blockage/Interference by Sec. Reflector	3.1 dB	0.9 dB	0.8 dB
3dB Beamwidth	0.5°	0.7°	0.8°
Peak Gain	43.5 dBi	43.0 dBi	42.0 dBi
Edge Antenna Element			
Spill-over Antenna Element	1.7 dB	1.1 dB	1.5 dB
Spill-over Secondary Reflector	2.5 dB	2.4 dB	3.2 dB
Blockage/Interference by Sec. Reflector	5.2 dB	0.4 dB	1.0 dB
3dB Beamwidth	0.8°	1.1°	0.8°
Peak Gain	38.0 dBi	42.3 dBi	40.8 dBi

Table 3.3: Simulation results for the *Cassegrain* and *Ritchey-Chrétien* reflector setups.

Dynamic Grouping of the 2x2 Sub-arrays

So far, fixed 2x2 sub-arrays form the antenna elements for the *Ritchey-Chrétien* antenna setup. Although the radial decline in gain is mitigated and the peak gain is increased, Figure 3.18 shows a variation in the gain of approximately $4-5$ dB. In order to bridge the gaps, dynamic groups of the single patch elements to 2x2 sub-arrays instead of fixed groups are introduced (see Figure 3.19). The method enables to reduce by half the spacing between the 2x2 sub-arrays while the number of patch antennas stays equal. This leads to a much more homogeneous gain profile across the whole field of view as visualized in Figures 3.20 and 3.21.

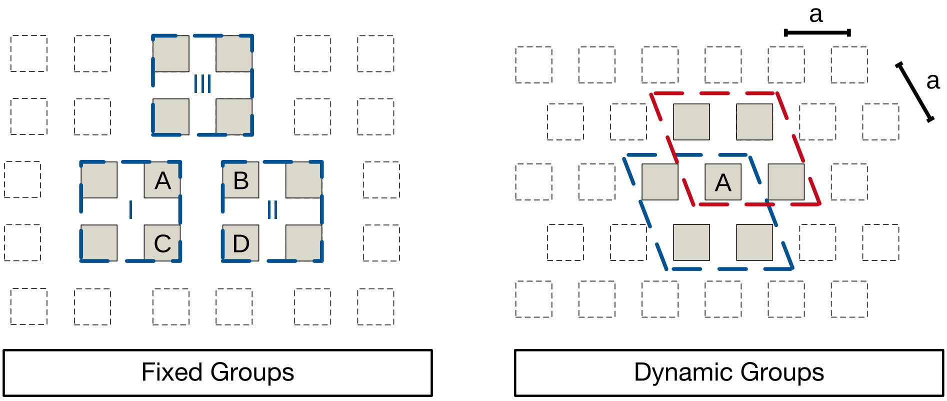

Figure 3.19: *Left:* Array containing fixed 2x2 microstrip patch sub-arrays I, II and III. A combination of patch element A, B, C and D is not possible. *Right:* Dynamic 2x2 sub-arrays. In contrast to the figure on the left, element A can participate in four different sub-arrays (two of them are shown surrounded by dashed lines). The grid now is a hexagonal arrangement, in order to provide a hexagonal and spot beam grid. The spacing between the patch antennas is $a \approx 0.7 \cdot \lambda$.

In order to realize the dynamic 2x2 sub-arrays, the signals received by the single patch elements have to be combined dynamically. This is done by an RF combination unit. A concept for such a solution based on RF MEMS switches is presented in the following section.

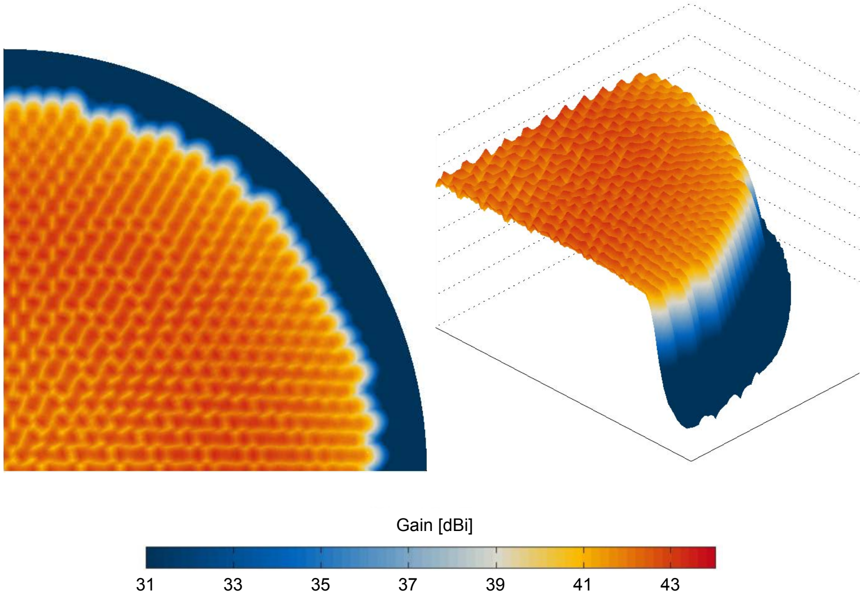

Figure 3.20: Visualization of one quarter of the simulated antenna gain for a *Ritchey-Chrétien* reflector setup with dynamic 2x2 sub-arrays on a planar array. The dynamic grouping enables to bridge the gaps occurring with fixed 2x2 sub-arrays. A homogeneous gain profile is created.

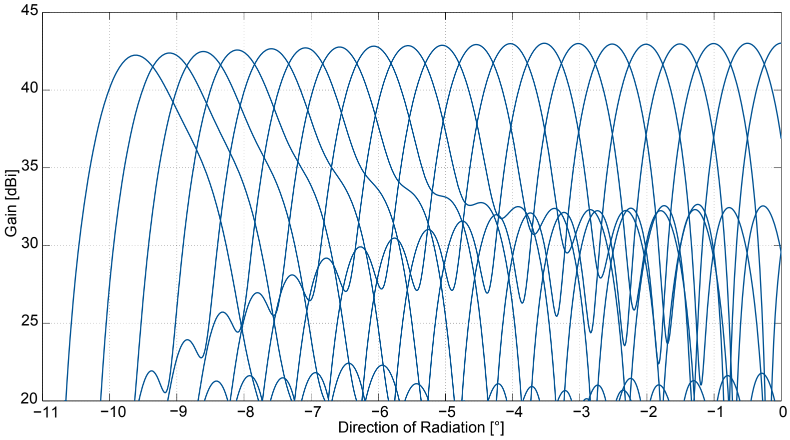

Figure 3.21: Radial cut through the gain profile of the aplanatic *Ritchey-Chrétien* reflector setup with dynamic 2x2 microstrip patch sub-arrays.

3.5 RF Switch Unit

The antenna concept presented in the previous section requires approximately 1600 patch antennas distributed on a hexagonal grid, in order to provide the homogeneous gain profile. The received signals from four adjacent patch elements have to be combined with adjusted phases to form a 2x2 sub-array. Subsequently, the sum signal has to be routed to one of the 15 transponders (in the case of 15 supported LEO satellites). For this task, a switch unit with 1600 input channels and 15 output channels has to be designed. Conventional space approved Single Pole Double Throw (SPDT) switches have a mass of approximately 55 g (cf. Dow-Key Microwave Corp. [2013]). Assuming only one switch per patch antenna leads to more than 1000 switches, which by far leads to an exceeding of the mass limits for a realistic space antenna system. Therefore, the concept for the switch unit in this thesis is based on RF Micro Electromechanical System (MEMS) switches. RF MEMS switches have dimensions below one millimeter and a negligible mass of micrograms or less (cf. Schönlinner et al. [2011] and Shea [2006]). In addition, MEMS switches possess a low signal attenuation of approximately 0.5 dB per switch (cf. Radant MEMS [2013]). The switches or switch modules (cf. Figure 3.22) are directly placed on PCBs, where the RF signals are distributed along microstrip lines (cf. Ziegler et al. [2009]). This saves harnesses and connectors.

State of the art switch units are based on tapering tree concepts (cf. Chan et al. [2009] and Figur et al. [2012]). Thereby, a number of k fixed switch units with n input channels and m output channels, where $n > m$, are concatenated in a tree structure with $k \cdot n$ input channels and m output channels. Figure 3.23 visualizes such a switch unit built of 4 to 2 basic elements.

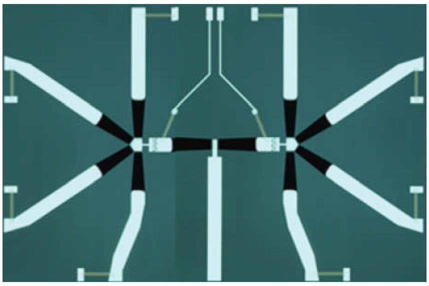

Figure 3.22: Microscope image of an 8 to 1 MEMS switch module. The black bars result from open MEMS switches which are not reflecting the incoming light to the camera. *(Image with kind permission from EADS Innovation Works, Germany)*

A drawback of tapering trees are routing conflicts, which occur if the number of input signals at one switch unit is larger than the number of output channels. Furthermore, the concept is fault-prone as one broken switch can block a whole branch.

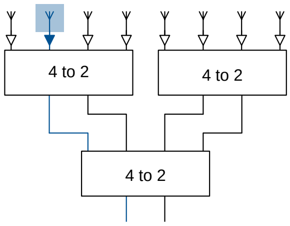

Figure 3.23: Tapering tree concept with 8 input channels and 2 output channels.

Adapted to the requirements of the antenna concept, a new design for a switch unit was developed. It is based on three separate modules: a *Combination Network*, a *Selection Network* and a *Switch Matrix* shown in Figures 3.24 and 3.25. The first module groups the 1600 patch elements into approximately 1600 different sub-arrays (see Figure 3.19). The second module contains 400 LNAs which amplify the signals from the sub-arrays. The number of active LNAs matches the number of received signals, i.e. the number of visible LEO satellites. The switch matrix, consisting of two PCBs, finally routes the amplified signals from the sub-arrays to the transponders. The individual PCBs can be attached to each other in a sandwich structure enabling a very lightweight and space saving setup (see Figure 3.27). Ideally, the three modules and the antenna array are integrated on one multilayer PCB. Each module includes a total of approximately 6500 MEMS switches.

The *Combination Network* connects each patch antenna to one out of four different combination ports by MEMS switches. A combination port forms the sum signal of four different patch elements, i.e. creates a 2x2 sub-array. The desired phases of the signals from the four patch antennas are set by the lengths of the microstrip signal paths (cf. Pillans et al. [1999a]).

The *Selection Network* connects one out of four combination ports to an LNA by MEMS switches. Only one of the four combination ports can be active at the same time since one patch antenna can only participate in one 2x2 sub-array.

The *Switch Matrix* consists of two identical PCBs with microstrip rows and columns. The LNA outputs from the *Selection Network* are connected to injection points distributed alternately on the two PCBs. This reduces the number of signals on each PCB avoiding routing conflicts. The injection points are located inside the rhombs created by the microstrip lines. They are schematically illustrated in the expansion in PCB 3 of Figure 3.25. The rows are connected to the columns by nodes consisting of six MEMS switches (see expansion in PCB 4 of Figure 3.25). The switch in horizontal direction is bypassing the node using vias to the other side, i.e. the second layer of the PCB. The transponders are connected via nodes at the edge of the matrix. They are represented by numbers in Figure 3.25. Each transponder has four connections, two at each *Switch Matrix* PCB, where only one connection is active at the same time.

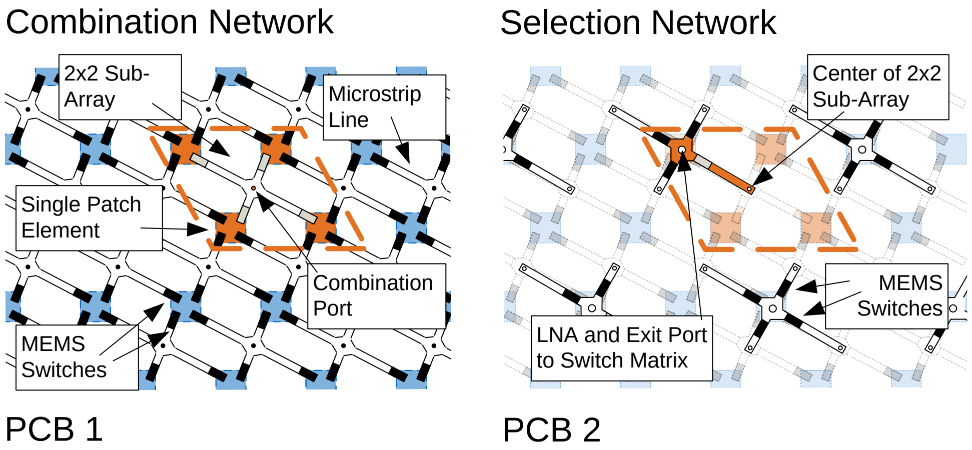

Figure 3.24: First and second PCB of the switch unit: Black bars represent open RF-MEMS switches, grey bars closed RF-MEMS switches, white bars microstrip lines.

The switch matrix concept and the routing strategy are chosen for minimizing the signal losses. This is achieved by keeping the signal paths short, by minimizing the number of crossed switches and by avoiding signal reflections along the paths. The transponder outputs are located at the edge of the switch unit closest to where most of the signals are received. The matrix rows and columns are not perpendicular since crossings with an angle larger than 90° reduce RF reflections.

Switching in a pre-calculated way enables the routing of the signals. The basic routing strategy is to route the signals out along one column for shortest paths. The column right or left from the injection point is chosen to the direction, where a smoother angle between row and column is achieved along the path. Signals on the upper half are routed to the top, signals on the lower part are routed to the bottom. If a signal on a column can not be routed due to occupied nodes or transponders, adjacent columns are used. Due to the high number of possible routing paths, the *Switch Matrix* avoids single points of failure since defective nodes can be bypassed easily.

The functionality of the *Switch Matrix* on the GEO satellite was simulated for a constellation of 15 LEO satellites. During 12 500 different LEO Satellite distributions on the matrix, no routing conflicts occurred. Statistics about the attenuation of the 120 000 simulated signal paths have been performed. The assumed attenuation was 0.5 dB per switch (cf. Radant MEMS [2013]) and 0.3 dB per centimeter for the microstrip lines (LTCC material) (cf. Kulke et al. [2002]). The average signal attenuation was determined to approximately 4.2 dB after the first LNA. A signal routed from the center of the matrix to the edge is attenuated by 8.2 dB. The maximum attenuation was approximately 23 dB which determines the necessary amplification by the LNAs. The histogram in Figure 3.26 shows the attenuation probability.

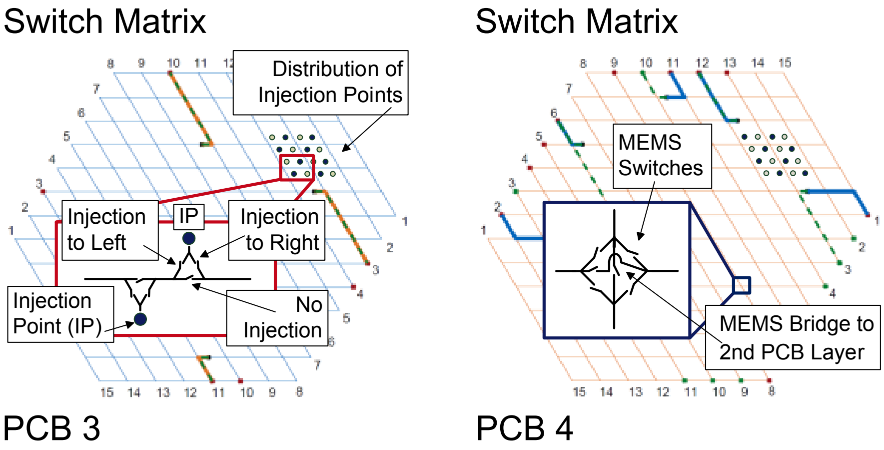

Figure 3.25: The *Switch Matrix* consists of two identical PCBs with each two layers: The red box in the left Figure shows the details of the switching schematics around the Injection Points (IP) where the LNA signals from PCB 2 are injected. A routing algorithm selects the signal routes on the matrix microstrip lines (blue lines on PCB 3, orange lines on PCB 4). The signals have to cross nodes shown in the blue box in the right Figure. At the rim, the signals are connected to different transponder inputs represented by numbers. The switching arrangements are only schematic and not optimized for RF signal flows.

The simulations show that the *Switch Matrix* has to be reconfigured every 5 s on average. MEMS switches can perform more than > 1 billion cycles during their life-time. Thus, the required cycles are not limiting the life-time of the MEMS switches, which exceeds 20 years under thermal stable conditions (cf. Shea [2006]).

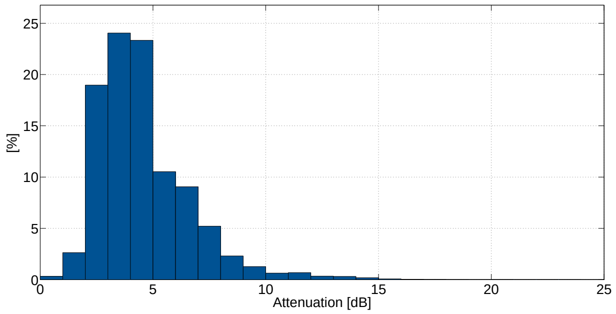

Figure 3.26: Histogram showing the fraction of 120 000 signal paths with a certain attenuation on the two *Switch Matrix* PCB layers.

3.6 Summary and Outlook

This chapter presented a new concept for a multibeam antenna system designed for a geostationary data relay. The antenna provides up to 15 LEO-GEO inter-satellite links concurrently. A visualization of the antenna system is shown in Figure 3.27.

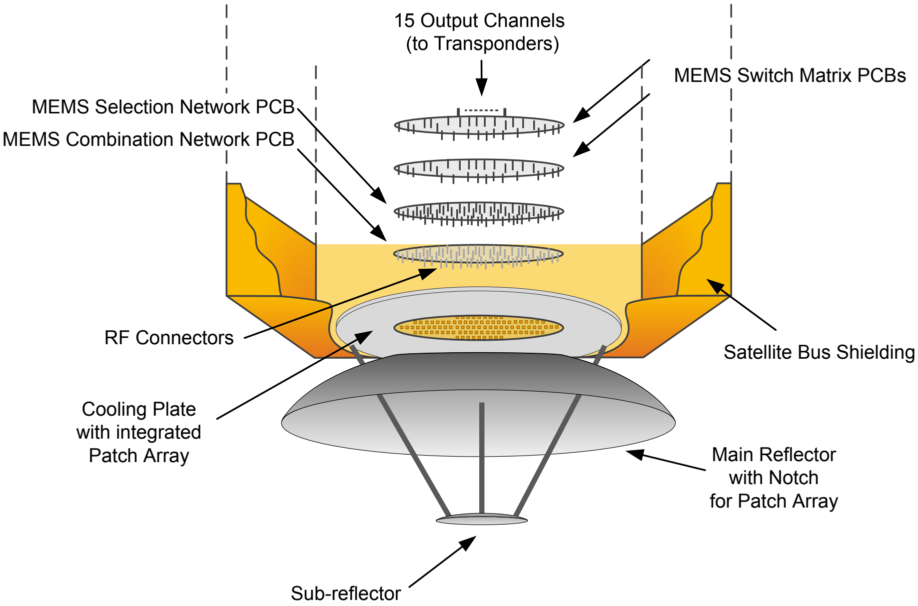

Figure 3.27: Exploded view drawing of the baseline antenna design. The *Ritchey-Chrétien* dual-reflector setup installed at the Earth deck of the satellite bus focuses the incoming radiation on a planar microstrip patch array. The antenna array is mounted on a cooling plate which is connected to the reflector to dissipate heat. The thermal shield of the satellite bus is connected to the rim of the cooling plate. The switch unit is located directly attached to the antenna array, but inside the thermally stable satellite bus. A planar design of the switch unit reduces space consumption and enables a compact setup.

The antenna system consists of an aplanatic dual-reflector setup as proposed by *Ritchey and Chrétien*. It compensates *Coma* and therefore provides a substantial gain over the complete field of view of ±10°. The reflector setup maps the sources typically on separate "spots" on the focal plane. The latter is covered by 1600 patch antenna elements, which are dynamically grouped into 2x2 sub-arrays. The grouping follows the image of the LEO satellites over the field of patches. A switch matrix routes the signals of the active 2x2 sub-arrays to the transponders. The number of transponders matches the number of maximum supported LEO satellites, which is cost and power efficient. The grouping as well as the routing of the signals to the RF-front-ends are done by a new switch unit using RF-MEMS switches. MEMS devices save space and weight and reduce the signal losses.

A dimensioning with a primary reflector of 1.2 meters leads to a homogeneous gain profile exceeding the required gain of 31.0 dBi to 40.1 dBi for achieving data rates of $30 - 100$ Mbit/s. The hardware complexity is proportional to the number of concurrently served satellites rather than to the served area. The switch unit can be combined with the antenna array to a sandwich like structure of PCBs. Ideally all layers are implemented on one PCB. The whole antenna concept is designed as a center aligned dual-reflector setup, which provides several advantages:

- The compact reflector system has no swiveling parts and can be integrated in a small GEO.
- Long antenna cables or wave guide connections between the antenna elements and the satellite bus are avoided. This makes the setup comparatively lightweight.
- The RF front-end components as well as the switch unit need stable thermal conditions and can be located behind the antenna array inside the satellite bus.
- The antenna array can be thermally connected to the primary reflector, which can be used to dissipate the heat produced by the LNAs and the collimated sunlight.

The theoretical antenna concept presented in this chapter shall be validated in future hardware demonstrations. A reduced version of a patch array consisting of 16 antenna elements will be part of an experimental payload on the German geostationary satellite "Heinrich-Hertz". The launch is scheduled for 2016 (cf. Wilke et al. [2013]). The experiment additionally includes the space qualification of the RF-MEMS switches.

Chapter 4

Attitude Determination Concept for Geostationary Data Relays

4.1 Introduction

The antenna system described in the previous chapter follows the LEO satellite movements by dynamically activating the corresponding 2x2 sub-arrays. Thereby, the timing of the hand-over from one 2x2 sub-array to the next is decisive. If the timing is incorrect, a fraction of the signal power is not mapped on the active 2x2 sub-arrays, but on adjacent inactive 2x2 sub-arrays. This leads to a loss in the signal-to-noise ratio and can cause an interruption of the LEO-GEO link.

The optimum timing of the hand-over can be determined by the LEO satellite positions, the GEO satellite position and the GEO satellite antenna pointing. The LEO satellite positions are known with accuracies of < 1 m using onboard GNSS receivers (cf. Section 5.2.2). Different concepts for the GEO satellite positioning are discussed in Chapter 5. They provide a positioning accuracy of < 1000 m. Since the distance between the LEO satellites and the GEO satellite is at least 34 000 km, such a deviation in the satellite positions only leads to a pointing error of $< 0.005°$. This translates into a loss in gain of < 0.05 dB (see Figure 3.21).

The GEO satellite attitude is typically determined using at least two star trackers. The accuracies can reach up to 0.005° (cf. Liebe [2002]). The GEO satellite antenna pointing can be approximated by the attitude of the GEO satellite. However, calibration inaccuracies between the star trackers and the antenna or any deviation from the calibration lead to a degradation in the antenna pointing accuracy. Deviations from the calibration can especially happen due to shocks and vibrations during launch.

The following section shows a new concept of antenna attitude determination developed in Günther and Knogl [2014]. It uses the information of the LEO satellite positions and measurements of the signal distribution on the antenna array. Since the attitude determination is performed directly with the antenna, calibration inaccuracies like in conventional approaches are excluded. Furthermore, hardware in addition to the existing communications hardware becomes dispensable.

4.2 Attitude Determination

The attitude of the antenna system can be described by the orientation of the spacecraft coordinate frame with respect to a reference coordinate frame (e.g. the ECEF reference coordinate frame). The axes of the spacecraft coordinate frame are in line with the satellite's symmetry axes while the origin of the coordinate system matches the satellite's center of mass (see Figure 4.1).

The satellite's attitude can be expressed by a rotation of the spacecraft coordinate frame around the satellite's center of mass with respect to a reference direction. Figure 4.1 shows such a 3-dimensional rotation composed by three concatenated rotations around the axis z, x' and again z''.

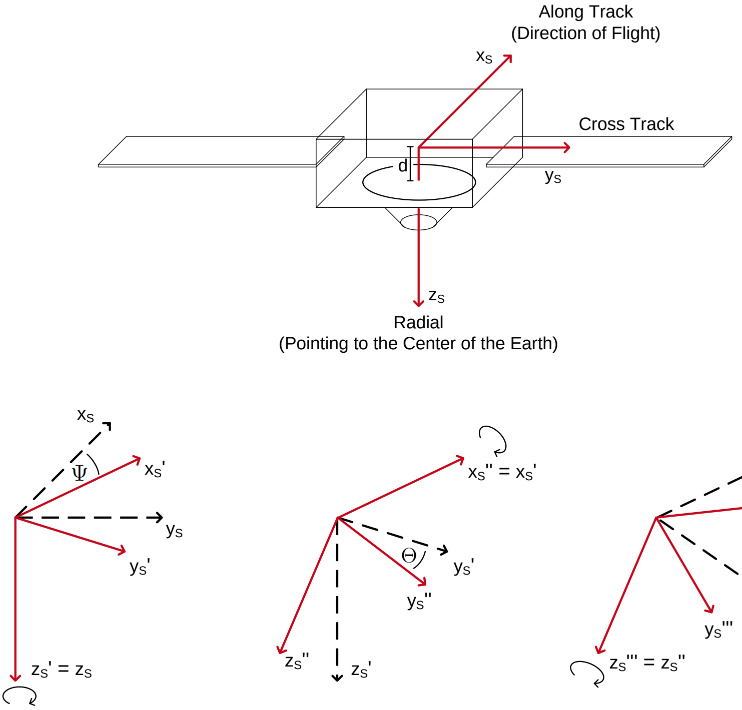

Figure 4.1: The spacecraft coordinate system is in line with the satellite's symmetry axes and has its origin at the satellite's center of mass. The antenna patch array is located at distance d from the satellite's center of mass. Three independent rotations with the associated Euler angles Ψ, Θ and Φ can be used to express a 3-dimensional rotation of the spacecraft coordinate frame.

In mathematical form this means that the rotation is decomposed in the following manner

$$R(\Psi, \Theta, \Phi) = R_z(\Psi) R_{x'}(\Theta) R_{z''}(\Phi), \tag{4.1}$$

where Ψ, Θ and Φ are the three associated Euler angles.

The rotation matrices are

$$R_z(\Psi) = \begin{pmatrix} \cos\Psi & \sin\Psi & 0 \\ -\sin\Psi & \cos\Psi & 0 \\ 0 & 0 & 1 \end{pmatrix} \quad \text{and} \quad R_x(\Theta) = \begin{pmatrix} 1 & 0 & 0 \\ 0 & \cos\Theta & \sin\Theta \\ 0 & -\sin\Theta & \cos\Theta \end{pmatrix}. \tag{4.2}$$

The reflector of the antenna presented in Chapter 3 maps the incoming signals of the LEO satellites to the focal plane. If the positions of the LEO satellites and the GEO satellite are known and the attitude of the GEO satellite antenna is not disturbed, nominal points $\overline{u}^k = (u_x^k, u_y^k)^{\mathrm{T}}$ on the antenna array can be determined where the signal power distributions of the LEO satellite signals have their maximum.

Explicit measurements of $\overline{u}^k$ during deviated attitude are not possible due to the ambiguous 2x2 sub-array gain profile (see Figure 3.20 and 3.21). However, searching for the 2x2 sub-arrays with the highest significant power level gives a rough signature in the form of the centers $\overline{c}^k$ of the sub-arrays. The power levels are resolved using an analog to digital (A/D) converter with a high resolution, e.g. 14 bits. If the function $\overline{f}(\xi; \overline{u})$ which transforms the K nominal points $\overline{u}^k$ on the focal plane under a rotation $R(\xi)$ with the angles $\xi = (\Psi, \Theta, \Phi)^{\mathrm{T}}$ can be determined, the antenna attitude estimation can be written as a discretized non-linear Least-Squares problem

$$\arg\min_{\xi} \sum_k \left\| \overline{f}(\xi; \overline{u}^k) - \overline{c}^k \right\|^2_{\Sigma^{-1}}. \tag{4.3}$$

The errors in the position of the 2x2 sub-array centers are approximated to be Gaussian with the covariance matrix Σ^k. The covariance matrix is defined as

$$\Sigma = \begin{pmatrix} \Sigma^1 & & \\ & \ddots & \\ & & \Sigma^K \end{pmatrix} \quad \text{with} \quad \Sigma^K = \begin{pmatrix} \sigma_{\mathrm{x}}^2 & 0 \\ 0 & \sigma_{\mathrm{y}}^2 \end{pmatrix}. \tag{4.4}$$

The standard deviations σ_{x}^2 and σ_{y}^2 are chosen to be proportional to $1/P^k$, where P^k is the received signal power level. Since measurements with high signal power are statistically closer to the 2x2 sub-array centers $\overline{c}^k$, they are weighted stronger. This mitigates the biases introduced by the discretized search for the 2x2 sub-array centers.

The transformation function $\overline{f}(\xi;\overline{u}^k)$ can be derived as follows.

An arbitrary 3-dimensional vector $\vec{u} = (u_x, u_y, u_z)^{\mathrm{T}}$ is mapped on the xy-plane by the following projection matrix P:

$$P = \begin{pmatrix} 1 & 0 & 0 \\ 0 & 1 & 0 \\ 0 & 0 & 0 \end{pmatrix} \tag{4.5}$$

The antenna concept of Chapter 3 assumes that the antenna patch array is mounted parallel to the xy-plane at distance d from the satellite's center of mass. A projection to any plane parallel to the xy-plane, described in 2-dimensional coordinates on that plane (i.e. eliminating the z-coordinate), is achieved applying the following matrix:

$$P_2 = \begin{pmatrix} 1 & 0 & 0 \\ 0 & 1 & 0 \end{pmatrix} \tag{4.6}$$

Accordingly, the transformation of an arbitrary point $\vec{u} = (u_x, u_y, d)^{\mathrm{T}}$ on the antenna patch array under a 3-dimensional rotation can be expressed in 2-dimensional coordinates as follows

$$P_2(R(\Psi, \Theta, \Phi)\vec{u}) = P_2(R_z(\Psi)R_x(\Theta)R_z(\Phi)\vec{u}) = \overline{v}, \tag{4.7}$$

where $\overline{v} = (v_x, v_y)^{\mathrm{T}}$ is a 2-dimensional vector.

Due to the projective character of the matrix P_2, Equation (4.7) can be expressed as

$$\begin{aligned} P_2(R_z(\Psi)R_x(\Theta)R_z(\Phi)\vec{u}) &= P_2R_z(\Psi)P_2\left(R_x(\Theta)R_z(\Phi)\right)\vec{u} = \\ = \underbrace{\begin{pmatrix} \cos\Psi & \sin\Psi \\ -\sin\Psi & \cos\Psi \end{pmatrix}}_{R_z^{(2)}(\Psi)} & \left[\begin{pmatrix} 1 & 0 \\ 0 & \cos\Theta \end{pmatrix} \underbrace{\begin{pmatrix} \cos\Phi & \sin\Phi \\ -\sin\Phi & \cos\Phi \end{pmatrix}}_{R_z^{(2)}(\Phi)} \begin{pmatrix} u_x \\ u_y \end{pmatrix} + d\begin{pmatrix} 0 \\ \sin\Theta \end{pmatrix}\right] = \\ = \overline{f}(\xi;\overline{u}). \end{aligned} \tag{4.8}$$

Thereby, $\overline{f}$ is a 2D vector function that is linear in the 2D coordinate $\overline{u}$ and non-linear in the variable $\xi = (\Psi, \Theta, \Phi)^{\mathrm{T}}$ defining the rotation.

Applying Equation (4.8), Equation (4.3) can be written as

$$\arg\min_{\xi} \sum_k \left\| P_2R\overline{u}^k - \overline{c}^k \right\|^2_{\Sigma^{-1}}. \tag{4.9}$$

This looks similar to a problem expressed by Grace Wahba in 1965 (cf. Whaba [1965]), where a rotation R has to be found which minimizes the metric $\sum_k \left\| R\overline{u}^k - \overline{c}^k \right\|^2_{\Sigma^{-1}}$. A number of solutions to the Wabha-Problem were developed which all rely on the orthogonality of R (see e.g. Davenport [1968], Markley and Mortari [2000]). Since $R^{\mathrm{T}}P_2^{\mathrm{T}}P_2R \neq 1$, these solutions are not applicable here.

Single Epoch Solution

The solution to Equation (4.3) can be found applying a Newton-Raphson iterative search of zeros. In the $s+1$-th step, the function $\overline{f}$ is linearized around ξ_s for computing the new state ξ_{s+1}. The corresponding derivatives for a linearization by Taylor expansion around a certain point $\xi_s = (\Psi_s, \Theta_s, \Phi_s)^{\mathrm{T}}$ are:

$$\begin{aligned}
\left.\frac{\partial f^k}{\partial \Psi}\right|_{\xi_s} &= R_z^{(2)}(\Psi_s)\left[\begin{pmatrix} 0 & \cos\Theta_s \\ -1 & 0 \end{pmatrix} R_z^{(2)}(\Phi_s)\begin{pmatrix} u_x^k \\ u_y^k \end{pmatrix} + d\begin{pmatrix} \sin\Theta_s \\ 0 \end{pmatrix}\right] \\
\left.\frac{\partial f^k}{\partial \Theta}\right|_{\xi_s} &= R_z^{(2)}(\Psi_s)\left[\begin{pmatrix} 0 & 0 \\ 0 & -\sin\Theta_s \end{pmatrix} R_z^{(2)}(\Phi_s)\begin{pmatrix} u_x^k \\ u_y^k \end{pmatrix} + d\begin{pmatrix} 0 \\ \cos\Theta_s \end{pmatrix}\right] \\
\left.\frac{\partial f^k}{\partial \Phi}\right|_{\xi_s} &= R_z^{(2)}(\Psi_s)\left[\begin{pmatrix} 0 & 1 \\ -\cos\Theta_s & 0 \end{pmatrix} R_z^{(2)}(\Phi_s)\begin{pmatrix} u_x^k \\ u_y^k \end{pmatrix}\right].
\end{aligned} \tag{4.10}$$

The linearized problem in point $\xi_s = (\Psi_s, \Theta_s, \Phi_s)^{\mathrm{T}}$ is subsequently written as

$$\arg\min_{\xi} \left\| \underbrace{\begin{pmatrix} f_\Psi^1 & f_\Theta^1 & f_\Phi^1 \\ f_\Psi^2 & f_\Theta^2 & f_\Phi^2 \\ \vdots & \vdots & \vdots \\ f_\Psi^K & f_\Theta^K & f_\Phi^K \end{pmatrix}}_{J} \underbrace{\begin{pmatrix} \Psi_{s+1} - \Psi_s \\ \Theta_{s+1} - \Theta_s \\ \Phi_{s+1} - \Phi_s \end{pmatrix}}_{\Delta\xi} + \underbrace{\begin{pmatrix} f^1(\xi_s; \overline{u}^1) - \overline{c}^1 \\ f^2(\xi_s; \overline{u}^2) - \overline{c}^2 \\ \vdots \\ f^K(\xi_s; \overline{u}^K) - \overline{c}^K \end{pmatrix}}_{\rho} \right\|_{\Sigma^{-1}}^2, \tag{4.11}$$

where e.g. $f_\Psi^k = \frac{\partial f^k}{\partial \Psi}$.

The iteration process of the Newton-Raphson approach is defined as

$$\xi_{s+1} = \xi_s - \left(J^{\mathrm{T}}\Sigma^{-1}J\right)^{-1} J^{\mathrm{T}}\Sigma^{-1}\rho, \tag{4.12}$$

provided that $J^{\mathrm{T}}\Sigma^{-1}J$ is non-singular.

Equation (4.3) can be solved for $K \geq 2$ independent signals, since the Euler angles Ψ, Θ and Φ count three unknown variables, while $2 \cdot K$ equations exist. Thereby, independent means that the two 2x2 sub-array centers are different.

Kalman Filter Solution

The single epoch solutions of Equation (4.3) are noisy (see Section 4.3). The estimation results are improved performing the measurements of the 2x2 sub-array centers $\overline{c}^k$ not just once but rather in a quasi-continuous manner for the time steps s while applying a Kalman filter (cf. Brown and Hwang [1997]).

In a Kalman filter, earlier estimates provide an a-priori information for later estimates. The relation between a-priori information and present time is established through a movement model. The model can reach different levels of sophistication depending on the knowledge about the moment of inertia of the satellite, the application of external torques by reaction wheels and the like. But even a simple linear model of movement usually provides a significant improvement.

The generalized Kalman filter for the attitude estimation can be described by the following equations

$$\begin{array}{rrcl} \text{Prediction:} & \hat{x}_s^- & = & F_s \hat{x}_{s-1}^+ \\ & P_{\hat{x}_s^-} & = & F_s P_{\hat{x}_{s-1}^+} F_s^{\mathrm{T}} + Q_s \\ & & & \\ \text{Update:} & \hat{x}_s^+ & = & \hat{x}_s^- - K_s y_s \\ & P_{\hat{x}_s^+} & = & \left(\mathbb{1} - K_s H_s\right) P_{\hat{x}_s^-} . \end{array} \tag{4.13}$$

with the state vector $\hat{x}_s^- = (\xi \ \Delta\xi)^{\mathrm{T}}$, the innovation $y_s = \overline{f}(\hat{x}_s^-; \overline{u}_s^k) - \overline{c}_s^k$, the observation matrix $H = (J \ 0^{2K \times 3})$, the Kalman gain $K_s = P_{\hat{x}_s^-} H_s^{\mathrm{T}} \left(H_s P_{\hat{x}_s^-} H_s^{\mathrm{T}} + W_s^{-1} \right)^{-1}$, the observation noise $W_s = \Sigma$, the state transition matrix for an approximated linear movement

$$F_s = \begin{pmatrix} \mathbb{1}^{3\times3} & \Delta t \cdot \mathbb{1}^{3\times3} \\ 0^{3\times3} & \mathbb{1}^{3\times3} \end{pmatrix} \tag{4.14}$$

and the covariance matrix describing the Gaussian noise of the process

$$Q_s = \begin{pmatrix} \sigma^2 \frac{\Delta t^3}{3} \cdot \mathbb{1}^{3\times3} & \sigma^2 \frac{\Delta t^2}{2} \cdot \mathbb{1}^{3\times3} \\ \sigma^2 \frac{\Delta t^2}{2} \cdot \mathbb{1}^{3\times3} & \sigma^2 \Delta t \cdot \mathbb{1}^{3\times3} \end{pmatrix} . \tag{4.15}$$

The process noise σ^2 is chosen to track all higher order derivative terms.

The predicted or *a priori* estimate covariance matrix $P_{\hat{x}_s^-}$ is initialized by the covariance matrix $P_{\hat{x}_0^-} = \left(H_0^{\mathrm{T}} W_0 H_0\right)^{-1}$ of the Least-Squares estimation in the first step. Also the state estimate $\hat{x}_s^+$ is initialized by the Least-Squares estimate in the first step.

4.3 Simulation and Results

The algorithm for estimating the GEO satellite attitude was tested in a simulation. The representative LEO satellite constellation shown in Table 5.5 and the communication parameters from Section 2.2 were applied for simulating the LEO satellite signal distributions.

The antenna is mounted with distance of $d = 1.2$ m to the satellite center of mass. The antenna pattern of the GEO satellite patch array is shown in Figure 3.20. Each 2x2 sub-array group covers approximately ±0.25° of the antenna FOV. The 2x2 sub-arrays are located on a discrete grid with spacing of $a \approx 0.7{\cdot}\lambda$, i.e. approximately 1 cm.

A time dependent simulation with an assumed linear drift of the GEO satellite attitude of $0.01°/s$ was performed. The measurement rate was selected to 5 Hz since on average the allocation of the 2x2 sub-arrays changes with a frequency of 5 Hz (see Section 3.5). The results are plotted in Figure 4.2. The Least-Squares estimation of Ψ, Θ and Φ shows a mean error of $\sqrt{\Delta\Phi^2 + \Delta\Theta^2 + \Delta\Psi^2}/3 = 0.15°$.

The Kalman filter estimation reaches accuracies of $< 0.05°$ after a convergence time of approximately 50 epochs, i.e. 250 s. The accuracy depends on the available number and distribution of the LEO satellite signals. An error of 0.05° in the satellite attitude in worst case causes a loss in gain of 0.9 dB for a center antenna element and 0.2 dB for an edge antenna element (see gain profile in Figure 3.20). The resulting worst case gain of > 39 dB still enables data rates of > 85 Mbit/s.

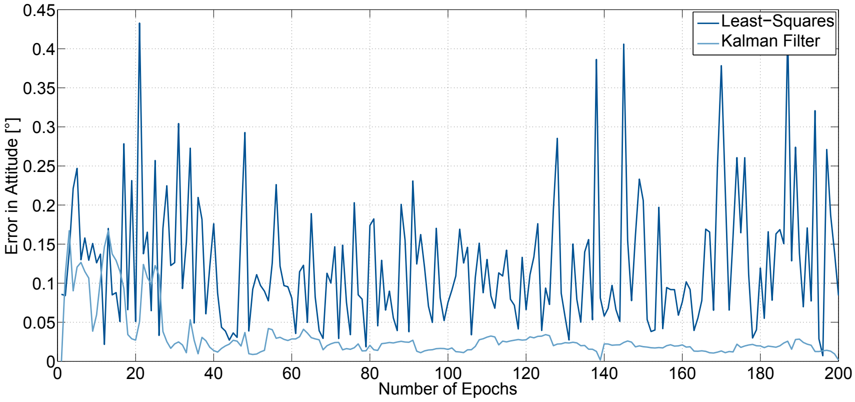

Figure 4.2: Error in the attitude estimation for the Least-Squares solution and the Kalman filter solution.

4.4 Summary

This chapter presented a new concept for the attitude determination of geostationary data relay satellite antennas. The concept makes use of the characteristics of the GEO satellite antenna to map the LEO satellite signals from different directions on different 2x2 sub-arrays on the antenna array. A variation in the GEO satellite attitude leads to a displacement of the LEO satellite signals on the antenna array. The information about the displacement is used to estimate the variation in the GEO satellite attitude. The points, where the LEO satellite signal power distributions have their maxima, can not be measured directly due to the ambiguous gain profile of the 2x2 sub-arrays. Instead, the centers of the 2x2 sub-arrays where the highest signal levels are measured are used. This approximation leads to a biased estimation of the attitude. In order to reduce the bias, a weighting of the measurements was applied. The LEO satellite signals which are closer to the 2x2 sub-array centers, i.e. which show a higher signal power level, are weighted stronger.

An estimation of the GEO satellite attitude based on the active 2x2 sub-array centers was performed applying an iterative Least-Squares algorithm. A simulation shows mean estimation accuracies in the order of $0.15°$. A discrete time-continuous estimation of the GEO satellite attitude applying a Kalman filter enabled to increase the estimation accuracy to $< 0.05°$. This accuracy is sufficient to determine the handover of the received LEO satellite signals from one 2x2 sub-array to the next with a sufficient accuracy to provide a GEO satellite antenna gain for enabling data rates of > 85 Mbit/s.

Chapter 5

Precise Positioning Concept for Geostationary Data Relays

5.1 Introduction

In the introduction of the previous chapter is explained that the determination of the correct hand-over timing from one 2x2 sub-array to the next requires the knowledge of the GEO satellite position. GEO satellite position determination is mainly based on range, or range and angular measurements from the ground (cf. Rosengren et al. [2004]). Methods in operational use and methods in experimental status are explained in the following section. Positioning accuracies reached by the most common RF methods range between $0.1 - 1000$ m (see Table 5.1). The error introduced to the hand-over timing due to these positioning inaccuracies leads to errors in the antenna gain of < 0.05 dB and is therefore negligible (see Section 4.3).

But ground station networks are expensive and produce a dependency. Since the geostationary data relay only requires one ground station for data downlink, it is beneficial to only use this station for the GEO satellite positioning. Single station position estimation using RF range and angular measurements however show the worst positioning accuracy of all concepts. Therefore, a new variant of positioning for geostationary data relays was developed. The main idea is to use the LEO satellites as navigation satellites for the GEO satellite and support the measurements by the ground station. The concept is explained after an introduction to conventional positioning methods in the next section.

Method of Geostationary Satellite Positioning	Number of Ground Stations	Magnitude of Accuracy	Ref.
Ground based range and angular measurements			
- RF range measurements	≥ 3	$0.1 - 100$ m	1
- Optical range measurements	≥ 3	$0.1 - 10$ m	2
- RF range and angular measurements	≥ 1	1000 m	3
- Passive optical angular measurements	≥ 2	$10 - 100$ m	4
Onboard GNSS receivers	-	$10 - 100$ m	5
Pseudolites	≥ 4	$1 - 100$ m	6

Table 5.1: Overview of demonstrated or proposed methods for the positioning of GEO satellites. The table also shows the necessary number of ground stations involved and the estimated accuracies.

---

[1] Huang et al. [2011], Dang et al. [2005], [2] Nakamura et al. [2010], [3] Hwang et al. [2008], Hajiyev and Ata [2011], [4] Tombasco [2011], Visser et al. [2005], [5] Ruiz and Frey [2005], [6] Derived from Theil [1998] (see Section 5.1.1).

5.1.1 Ground Based Range and Angular Measurements

The different ground based approaches for GEO satellite positioning can be characterized by their use of radio frequency or optical measurements as well as by the number of ground stations involved (see Figure 5.1).

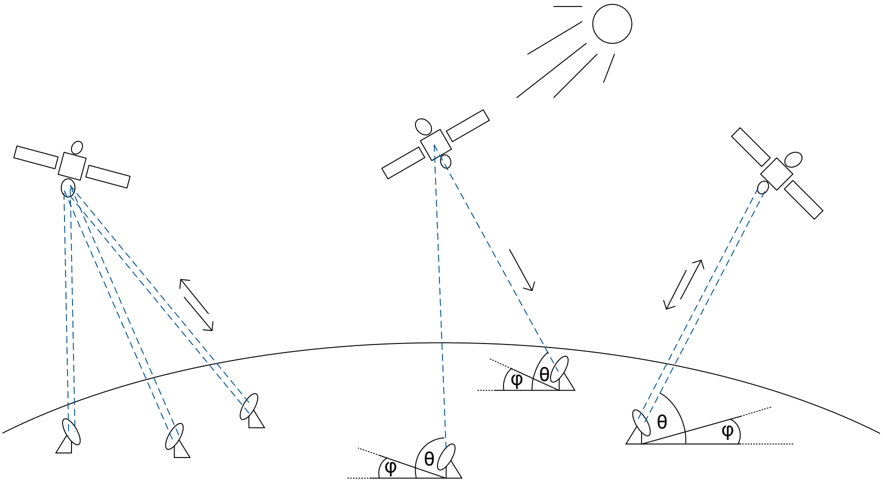

Figure 5.1: Ground based GEO satellite positioning can be performed by range measurements with a network of ground stations in the optical or RF domain (*left*), passive optical angular measurements with a network of ground stations (*center*) and range and angular measurements with a single ground station (*right*).

RF range measurements applying a network of ground stations

Probably the most common method to determine the position of GEO satellites uses range measurements performed by a network of ground stations. At least three stations are necessary to determine the position. Thereby, an onboard transponder has to re-transmit ground based ranging signals (see ECSS-E-ST-50-02C [2008]). The Flight Dynamics Facility (FDF) of the US Goddard Space Flight Center (GSFC) uses this method for the TDRSS satellites. Four ground stations located at White Sands Missile Range (WSC), American Samoa (AMS), Ascension Island (ACN), and Alice Springs in Australia (ALS) are providing the ranging signals (cf. Downs [2008]). This so called Bilateral Ranging Transponder System (BRTS) achieves nominal orbit accuracies of approximately $60 - 100$ m as presented in Dang et al. [2005] using S-band signals. Recent studies for C-band ranging with four stations showed positioning accuracies of GEO satellites below 1 m in radial direction (cf. Huang et al. [2011]). The propagation times include biases due to hardware and atmospheric delays, which limit the positioning accuracies (cf. Dang et al. [2005]).

RF range and angular measurements using a single ground station

Since GEO satellites hardly move relative to the tracking station, it is not possible to apply range and range rate measurements for accurate position estimation like applied for LEO satellites. Therefore, angular measurements of the pointing direction to the GEO satellite have to support the range measurement. The accuracy of the angular measurement mainly depends on the size of the antenna, which determines the beamwidth. But also large antennas only achieve accuracies of 0.01° level (e.g. $\Theta_{3\text{dB}} \approx 0.07°$ for a 10 m Ka-band antenna), which translates to several kilometers in geostationary orbit (see Rosengren et al. [2004]). Experiments showed that positioning accuracies of 1.5 km can be reached (cf. Hwang et al. [2008] and Hajiyev and Ata [2011]).

Passive optical angular measurements applying a network of ground based telescopes

Passive optical angular measurements make use of sunlight reflections from GEO satellites. The illuminated objects have to be tracked by at least two optical telescopes to determine their angular position. Advantageous is the passivity of the method, which does not require additional onboard hardware and ground based signal sources. The method therefore is perfectly suited for intelligence tasks aiming at the identification of the position of unknown objects. Disadvantageous are the limited observation periods only possible during night, clear sky conditions and proper illumination of the spacecraft by the sun or moon. In addition, the size and attitude of the object determines the reflectivity. Tombasco [2011] analyzed passive ground based optical methods and gives the maximum achievable accuracy to approximately 10 m. Common accuracies are stated to be in the range of 100 m, which is in agreement with Visser et al. [2005]. The positioning accuracy is limited by the accuracy of the angular measurements (cf. Tombasco [2011]).

Active optical range measurements applying a network of laser ground terminals

A method, only tested in experimental operation yet, is GEO satellite position determination by ground based Satellite Laser Ranging (SLR). The ETS-VIII geostationary satellite launched in December 2006 carries a 26 cm × 30 cm laser onboard reflector serving for laser ranging experiments (cf. Nakamura [2006]). Accordingly, one of its main purposes is the establishment of the SLR skills for the geostationary orbit. For the experiment, several satellite laser ranging ground stations, including the International Laser Ranging Service (ILRS) stations (cf. Pearlman et al. [2002]), served for data acquisition. The accuracy of satellite positioning was estimated to several centimeters in radial direction and approximately 10 m in cross-track and along-track direction (cf. Nakamura et al. [2010]). The accuracy is limited by the sensor biases and measurement errors (cf. Tombasco [2011]).

5.1.2 Onboard GNSS receivers

GNSS receivers have become a standard payload for LEO satellites and GNSS navigation is a common method to accurately position LEO satellites (e.g. Kuang et al. [2001]). Accuracies in the order of centimeters are reached applying additional external information, like atmospheric measurement data, for post-processing (see Table 5.3 in Section 5.3.1). Since GNSS satellite antennas are pointing to the Earth, LEO satellites can properly receive their signals. They orbit at < 1500 km altitude and therefore below GNSS constellations at approximately 20 000 km. GEO satellites have altitudes of 35 786 km and orbit higher than GNSS satellites. They can not receive signals from the most nearby GNSS satellites. Instead, only signals from GNSS satellites passing the Earth on the opposite side of the GEO satellite can be received (see Figure 5.2). Since the GNSS satellite antennas have a limited 3 dB beamwidth of e.g. approximately ±15° for GPS satellites (see Figure 5.4), the signals are only slightly exceeding the rim of the Earth.

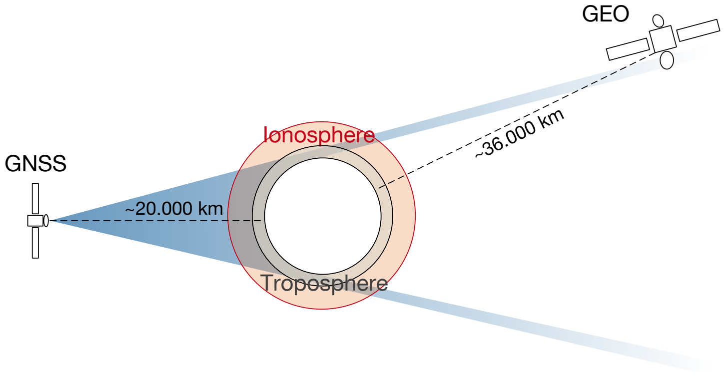

Figure 5.2: The schematic overview (not true to scale) shows the small fraction of the GNSS antenna main lobe which passes the Earth. A GEO satellite can only receive signals from GNSS satellites on the opposite side of the Earth as GEO satellite orbits are located above GNSS orbits. This leads to a large free-space loss as well as signal delays by the atmosphere.

Several disadvantages compared to GNSS signal reception on the ground or in LEO satellite orbits characterize the signal reception in geostationary orbits:

- GNSS signals from four satellites or more are only visible simultaneously for a few moments per day (see Figure 5.3). Since four satellites are the minimum number to derive a navigation solution based on GNSS services, the availability of the positioning service is very low.
- The GNSS signals which can be received in geostationary orbit emerge from a small solid angle. Therefore, the Positional Dilution of Precision (PDOP) is high at approximately 25 (cf. Ebinuma et al. [2004]) (for theoretical background see Section 5.3.2). This corrupts the achievable positioning accuracy.
- The distance between the receivable GNSS satellites and the GEO satellite is almost two times the Earth radius plus the GEO orbital altitude plus the GNSS orbital altitude. It sums up to almost 70 000 km compared to 20 000 for GNSS receivers on the ground. The free-space loss is more than 10 times larger than for GNSS signals on ground. Only faint signals at approximately -166 dBW are received in geostationary orbits (cf. Zentgraf et al. [2010]). This enlarges the Cramér-Rao Bound (see Equation (5.3)) and therefore reduces the achievable positioning accuracy.
- The GNSS signals which can be received in geostationary orbits pass close to the Earth. They are propagating through a large fraction of the atmosphere facing signal delay and phase advance.

Theoretical, as well as experimental research was performed, in order to develop operational geostationary onboard GNSS receivers. The quality of GNSS signals received in geostationary orbit has been determined in experiments (cf. Balbach et al. [1998] and Kronman [2003]). In future, tests with fully functional onboard receivers shall follow like proposed by Zentgraf et al. [2010].

EADS Astrium expects their MosaicGNSS Receiver to reach accuracies of approximately 150 m. In order to extend the signal reception times and therefore to increase the number of concurrently visible GNSS satellites, also methods able to deal with the low side-lobe signals are discussed (see Figure 5.4). Ruiz and Frey [2005] estimate a theoretical positioning accuracy of 160 m for main-lobe single frequency use and 4 m for dual frequency with side-lobe reception.

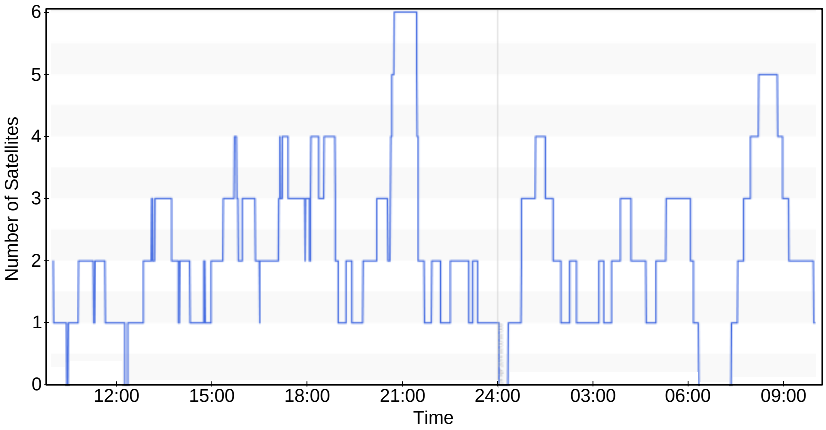

Figure 5.3: Example of the number of available pseudorange measurements for a GPS receiver on a GEO satellite considering a GPS beamwidth of ±25°, i.e. FOV of the main lobe.

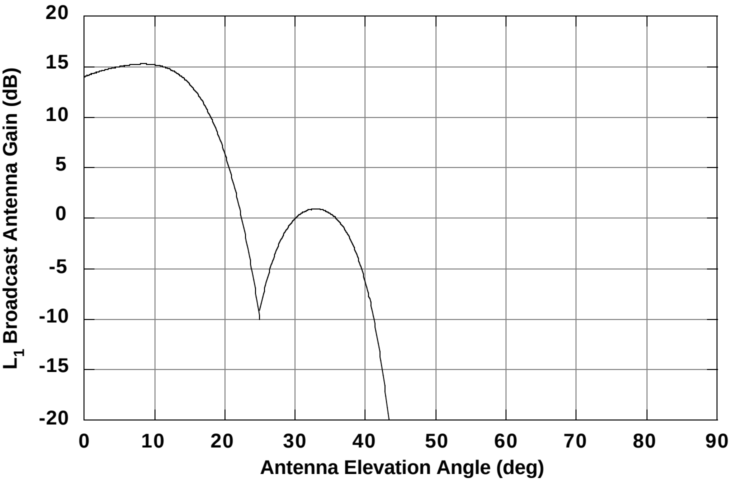

Figure 5.4: GPS II/II-A gain pattern as shown in Powell et al. [1999].

5.1.3 Pseudolites

As discussed in the previous section, GNSS positioning in geostationary orbits is challenging also due to a limited number of concurrently visible GNSS signals. As a consequence, a variant of the method was proposed in the late 90's (cf. Theil [1998] and cf. Gregorwich et al. [2002]). Fixed signal sources on the ground shall additionally transmit GNSS signals. This increases the number of available signal sources for onboard GNSS receivers. These ground based sources are called pseudolites, a contraction of the term "pseudo-satellite".

Compared to GNSS satellites, the positioning accuracy of the signal sources on the ground is high (centimeter level, cf. IGS Central Bureau [2013]). Applicable RF equipment calibration techniques as used in time-transfer stations (cf. Fujieda et al. [2007]) further helps reducing the transmitter biases. In addition, a large Equivalent Isotropically Radiated Power (EIRP) can be provided on the ground. In comparison to satellites, power is not a limiting factor. A disadvantage of pseudolites is its fixed position. It inhibits an effective bias estimation as shown in Section 5.3.4.

Figure 5.5: The blue area shows the maximum region a GEO satellite at 10° longitude can cover on the ground. In addition, the visible ground stations of the ESA ESTRACK ground station network are marked.

Theil [1998] performed a study about a pseudolite configuration of four pseudolites located at North Cape, Washington, Cape Horn and Cape Town serving a GEO satellite above the Atlantic ocean. Analysis on the dilution of precision of a pure pseudolite navigation concept shows DOP values of 400 in radial direction and 5 and 10 in cross-track and along-track direction of a GEO satellite above the Atlantic ocean. An extension with one additional pseudolite could reduce the DOP to 125 in radial direction and 4 and 9 in cross-track and along-track direction. The high DOP values, especially in radial direction, are based on the concentration of pseudolites in a very small solid angle of only ±10 degrees as seen from the GEO satellite (see Figure 5.5). Investigating the geometry H-matrix (cf. Section 5.3.2) of a pseudolite distribution with five pseudolites shows a bad conditioning. The radial component of the unit vectors, pointing from the pseudolites to the GEO satellite, and the fourth column for mapping the clock offset into the range domain are almost linearly dependent:

$$H = \begin{pmatrix} -0.1092 & 0.2040 & 0.9729 & 1.0000 \\ 0.0944 & 0.1140 & 0.9890 & 1.0000 \\ -0.1463 & 0.1605 & 0.9761 & 1.0000 \\ -0.0146 & 0.3121 & 0.9499 & 1.0000 \\ 0.0090 & 0.0873 & 0.9961 & 1.0000 \end{pmatrix} \tag{5.1}$$

A combined constellation of GNSS satellites and a pseudolite network for positioning of GEO satellites can improve the geometrical DOP. Possible locations for pseudolites serving a GEO satellite above Europe (10° East) could be in vicinity to the ESA ESTRACK network ground stations. Figure 5.5 shows such a distribution. The DOP values by the ESTRACK network alone are 136 in radial direction, 4 in cross-track direction and 31 in the along-track direction. The best case DOP of the GPS constellation in combination with the ESA ESTRACK pseudolite distribution is 49 in radial direction, 2 in cross-track direction and 10 in the along-track direction.

For signal broadcast in the GNSS L1-band at 1.575 GHz, the ionospheric influences are proposed to be estimated by using a dual frequency receiver on the ground and analyzing the received GNSS signals. They more or less have the same signal paths through the ionosphere as the upwards transmitted pseudolite signals. In order to achieve a minimum usable signal power level of -160 dBW, a transmit power of at least 19 dBW is required using an antenna with 23 dB gain (e.g. reflector antenna with 1.1 m diameter and beamwidth $\Theta_{3\mathrm{dB}} \approx 12°$).

A final conclusion about the achievable positioning accuracies is not presented in Theil [1998], but can be estimated considering the error parameters. Assuming a GPS code measurement noise σ of $0.2-0.8$ m and a PDOP of approximately 140, the positioning uncertainty σ_{pos} is estimated applying $\sigma_{\mathrm{pos}} = \sigma \cdot \mathrm{PDOP}$ to $28-112$ m. For the application of Galileo signals with approximately $0.02-0.2$ m code measurement noise, the estimated positioning uncertainty is approximately $2.8-28$ m.

5.2 LEO Satellite Based Concept

5.2.1 Characterization of the Concept

After an overview of different methods for GEO satellite positioning, this section explains the new variant of a LEO satellite based positioning concept. The concept uses the low data rate TT&C links between the LEO satellites and the GEO satellite which were introduced in Section 2.2 (cf. also Katona [2012]). The global horn antenna for the low data rate link on the GEO satellite, in contrast to the multibeam antenna with the switch unit, provides the same signal paths for each LEO satellite signal. This is advantageous for the bias estimation, which is explained in Section 5.2.2.

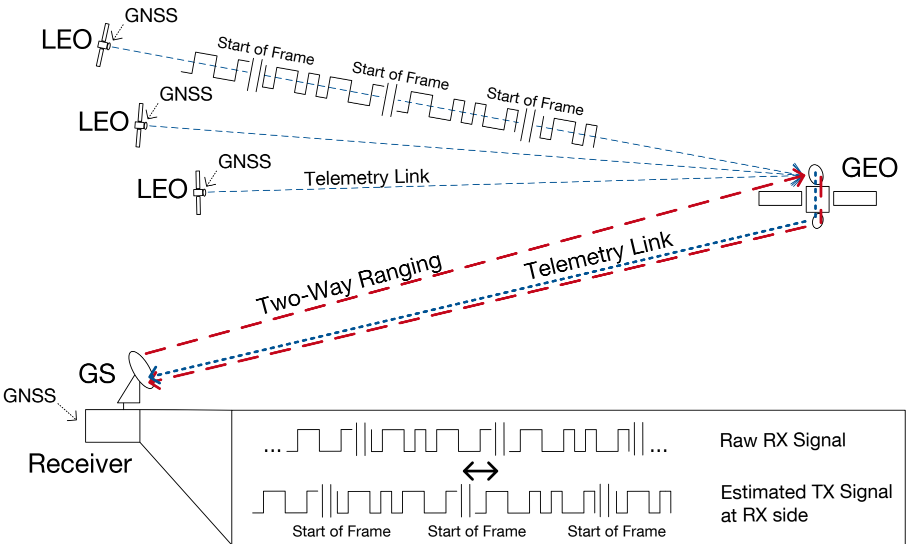

Figure 5.6: Concept for the precise positioning of geostationary data relays. Correlating the recovered LEO satellite TX signal with the raw RX signal enables to estimate the LEO-GEO-Earth pseudoranges. An additional two-way range measurement between the GEO satellite and the ground station enables to separate the LEO-GEO-Earth pseudoranges in a GEO-Earth pseudorange and a LEO-GEO pseudorange. The LEO-GEO pseudoranges are used to estimate the GEO satellite position. LEO satellite positioning and time synchronization between the LEO satellite and the ground station shall be performed with the help of GNSS services.

The main idea of the positioning concept is to use the low data rate links for pseudorange and range measurements. The pseudorange measurements are performed between the LEO satellites and the ground station via the transparent transponder of the GEO satellite (see Figure 5.6). Additional two-way range measurements are performed between the ground station and the GEO satellite.

The range measurements enable a separation of the LEO-GEO-Earth pseudoranges in a GEO-Earth pseudorange and a LEO-GEO pseudorange. The LEO-GEO pseudoranges are used to estimate the GEO satellite position similar to GNSS positioning, where pseudoranges between the GNSS satellites and the receiver are used. Only difference is the clock estimation. In contrast to GNSS positioning, the receiver clock is not estimated using the pseudorange measurements, but synchronized to the transmitter clock. This overcomes the problem explained in Section 5.1.3 for the pseudolites, where a strong correlation between the position and clock estimation of a GEO satellite leads to large dilution of precision. This idea of separated clock synchronization already was proposed by Misra and Pratt [1994] for GPS accuracy improvement. The synchronization between the LEO satellite transmitter clock and the ground station receiver clock is performed via GNSS services, while the GNSS onboard receiver is additionally used to estimate the LEO satellite positions (see Figure 5.6).

Equation (5.2) shows the pseudorange model for the LEO-GEO-Earth (LGE) measurements

$$\begin{aligned}\rho^n_{\mathrm{LGE}} = c\,(t^n_{\mathrm{E}} - t^n_{\mathrm{L}}) + \eta^n_{\mathrm{LGE}} =& \|\vec{r}_{\mathrm{G}} - \vec{r}^{\,n}_{\mathrm{L}}\| + \|\vec{r}_{\mathrm{E}} - \vec{r}_{\mathrm{G}}\| + I^n_{\mathrm{LG}} + b^n_{\mathrm{L}} \\ &+ b^n_{\mathrm{G}} + I^n_{\mathrm{GE}} + T_{\mathrm{GE}} + b^n_{\mathrm{E,RX}} + \eta^n_{\mathrm{LGE}},\end{aligned} \tag{5.2}$$

with the indices E for Earth station, G for GEO satellites and L for LEO satellite. c is the speed of light, t^n_{L} is the time of signal transmission on the nth LEO satellite and t^n_{E} is the time of signal reception at the Earth station. For an FDMA scheme without frequency reuse on the telemetry link, the number of LEO satellites is equal to the number of frequencies. Thereby, the nth frequency on the LEO-GEO link and the nth frequency on the GEO-Earth link are different due to the frequency transposition on the GEO satellite. I^n_{LG} is the ionospheric bias on the LEO-GEO link and I^n_{GE} on the GEO-Earth link. b^n_{L} is the LEO satellite bias and b^n_{G} is the correspondent GEO satellite bias for each LEO satellite carrier frequency. $b^n_{\mathrm{E,\,RX}}$ is the ground station receiver bias, T_{GE} is the tropospheric path delay on the GEO-Earth link and η^n_{LGE} is the ground station receiver noise. The clock synchronization biases are absorbed in b^n_{L}. The influences of the different terms are explained in the next section.

5.2.2 Analysis of the Pseudorange Noise and Error Statistics

The positioning accuracy of the pseudorange based concept explained in the previous section is limited by the pseudorange noise and errors. The main noise phenomena are the receiver noise and the clock noise, which contribute to it as Gaussian noise. In addition, biases like clock biases, internal satellite path delays, phase center variations and atmospheric path delays contribute with a constant offset.

Receiver Noise

The receiver noise of the LEO-GEO-Earth link is characterized by the Carrier Power to Noise Spectral Density Ratio C/N_0 which is determined by the link budget. An overview of the link budget calculations is presented in Appendix A. The GEO-Earth link shows a much higher C/N_0 than the LEO-GEO links as ground antennas can be larger than space antennas. This makes the LEO-GEO links the limiting link for the overall C/N_0 (see Table 5.2).

The C/N_0 at the receiver constrains the maximum achievable accuracy of the timing estimation and therefore influences the positioning accuracy. The Cramér-Rao Bound (CRB) provides a bound on the achievable accuracy (cf. Kay [1993]):

$$\sigma_\rho \geq \sqrt{\frac{c^2}{\frac{C}{N_0} T_\mathrm{i} \cdot \frac{\int (2\pi f)^2 |S_\mathrm{m}(f)|^2 df}{\int |S_\mathrm{m}(f)|^2 df}}}, \tag{5.3}$$

with c the speed of light, T_i the receiver integration time and $S_\mathrm{m}(f)$ the Power Spectral Density dependent on the carrier frequency f.

The maximum integration time is determined by the maximum tolerable frequency drift Δf, which leads to a phase error $\Delta\phi$ during the integration time according to $T_\mathrm{i} = \frac{2\pi \cdot \Delta\phi}{\Delta f}$. GNSS receivers typically achieve residual frequency drifts due to Doppler pre-compensation of approximately 1 Hz. This leads to integration times in the range of several milliseconds up to one second.

For the pseudorange measurement concept presented in this thesis the LEO satellites apply a Doppler pre-compensation. In addition, a fixed ground receiver with high computation power is used. The receiver is able to store the signal samples, estimate the frequency drift of the unknown GEO Doppler and perform a post-processed correlation. Therefore, integration times of 60 s or more are possible. Limitation is mainly due to the available memory and computation power to handle the data for the correlation algorithms. Standard telemetry transfer frame protocols like described in the ECSS-E-ST-50-03C standard (cf. ECSS-E-ST-50-03C [2008]) can be used. They carry the navigation messages containing the information about the positions and the clocks of the LEO satellites.

Table 5.2 shows an overview of different LEO satellite onboard communication systems and the corresponding Cramér-Rao Bounds defined by the parameters C/N_0, carrier frequency and bandwidth, symbol rate and integration time. For comparison, also a typical GPS-Earth link at the L1 frequency band is listed. The link budgets are calculated following the formalism presented in Appendix A. A detailed link budget for the GEO-Earth link is presented in Table 5.7.

Parameter	System 1	System 2	System 3	System 4	GPS-Earth
Carrier Frequency	27 GHz				1.575 GHz
Modulation	BPSK				BPSK
Symbol Rate	2 MBd/s		1 MBd/s		1.023 MBd/s
Carrier Bandwidth	36 MHz	2.3 MHz	2.3 MHz	2.3 MHz	2.0 MHz
TX Reflector Diameter	0.5 m	0.5 m	0.5 m	0.25 m	-
TX Antenna Gain	40.8 dBi	40.8 dBi	40.8 dBi	34.8 dBi	11.8 dBi
TX Power	50 W	50 W	10 W	10 W	44.8 W
TX EIRP	56.8 dBW	56.8 dBW	49.8 dBW	43.8 dBW	27.3 dBW
RX Antenna Gain	18 dBi				3.0 dBi
RX Sys. Noise Temp.	550 K				320 K
RX G/T	−10.1 dB/K				−27.4 dB/K
Free Space Loss	213.4 dB				182.5 dB
Atmospheric Loss	-				1.0 dB
C/N_0 LEO-GEO	61.9 dBHz	61.9 dBHz	54.9 dBHz	48.9 dBHz	-
C/N_0 GEO-Earth	93.0 dBHz				-
Overall C/N_0	61.9 dBHz	61.9 dBHz	54.9 dBHz	48.9 dBHz	45.0 dBHz
CRB ($T_\mathrm{i} = 1$ s)	2.0 cm	6.8 cm	25.4 cm	50.6 cm	78.3 cm
CRB ($T_\mathrm{i} = 60$ s)	0.3 cm	0.9 cm	3.3 cm	6.5 cm	-

Table 5.2: Different system parameters for LEO satellite onboard equipment and their influence on the LEO-GEO link and the resulting Cramér-Rao Bound for the LEO-GEO-Earth pseudorange measurements. The Cramér-Rao Bound is limited by the LEO-GEO link, since the C/N_0 on the GEO-Earth link is much higher than the C/N_0 on the LEO-GEO link. In comparison, the last column shows the values for a typical GPS-Earth link. The RX parameters are for the GEO satellite onboard equipment, respectively the GPS ground receiver equipment. The receiver integration time was assumed to be 1 s and 60 s for the LEO-GEO-Earth link. An integration time of 60 s is not feasible for GPS receivers.

Ground Station Position Error

The ground station is assumed to be positioned using geodetic GNSS receivers. The accuracies are comparable to geocentric coordinates of IGS tracking stations, which can be determined to < 1 cm according to the IGS Central Bureau [2013]. Thereby, models considering Earth tides, plate tectonics, etc. are applied. Additional errors introduced by the RF equipment are explained under "Antenna and RF-Equipment Biases".

LEO Satellite Position Error

The LEO satellites serving as navigation satellites are proposed to be positioned by onboard GNSS receivers. Such payload has become standard since several years (e.g. NASA's JPL BlackJack GPS receiver). The accuracies achieved are specified in Roselló et al. [2012] to $3 - 10$ m in real-time and < 2 cm after post-processing. For near real-time precise positioning, see Haines et al. [2010]. An overview of currently achieved LEO satellite accuracies is presented in Table 5.3.

Mission	RT	NRT (1-3 h)	STC (1-2 days)	NTC (1 month)
GOCE (launched 2009)		$<$ 50 cm rms (req.)	$<$ 10 cm rms (achieved $\approx$ 4 cm)	$<$ 2 cm rms (achieved)
Swarm		$<$ 10 cm rms	$<$ 10 cm rms	$<$ 10 cm rms
Sentinel-1 (SAR interferom.)	10 m (3 s) (xyz)	5 cm rms (xyz)	5 cm rms (xyz)	5 cm rms (xyz)
Sentinel-3 (Altimetry)	3 m rms (radial)	8 cm rms (radial)	3 cm rms (radial)	2 cm rms (radial)
SAC-C	approx. 1 m (achieved)			

Table 5.3: Required and achieved LEO satellite positioning accuracies for Real-Time (RT), Non Real-Time (NRT), Slow-Time Critical (STC) and Non-Time Critical (NTC) applications as presented in Roselló et al. [2012] and Zumberge et al. [2003].

Clock Synchronization Error

In addition to the position determination, the onboard and geodetic GNSS receivers shall also serve for clock synchronization among the LEO satellites and the ground station. According to Nie et al. [2007], accuracies of $2 - 3$ ns are achieved with existing GPS hardware. In future, the new Galileo signals will improve the time synchronization abilities. Accuracies of < 1 ns are expected, which corresponds to an error of < 30 cm (cf. Furthner et al. [2003]).

Ionospheric Bias

Services, like the European Geostationary Navigation Overlay Service (EGNOS) or the Wide Area Augmentation System (WAAS), provide amongst others correction data for the ionospheric path delay for GNSS receivers on the ground. Allain and Mitchell [2008] estimate an upper bound for the ionospheric path delay at GNSS frequencies of 1.5 m (90% 3 m) applying appropriate models of the ionospheric electron density. Due to the frequency dependency of the ionospheric refraction group index of $n_{\mathrm{gr}} \approx 1 + \frac{40.3\, n_{\mathrm{e}}}{f^2}$, the ionospheric path delay for Ka-band frequencies of $f = 27$ GHz is by more than a factor of 300 smaller than for GNSS frequencies in L-band at 1.5 GHz. Therefore, the ionospheric influences can be considered to be < 1 cm.

Tropospheric Bias

For Ka-band signals, the wet component of the troposphere causes path delay variations of up to 30 cm in zenith direction (cf. Elgered [1982]). Applying appropriate atmospheric models can limit the tropospheric biases. The accuracy of blind models is significantly enhanced if current atmospheric radiosonde or radiometer measurement data are available as input. Martellucci [2002] shows accuracies in the order of centimeters for Ka-band. Tropospheric effects on the GEO-Earth link are canceled applying the two-way measurements for the LEO satellite based concept. For ground based positioning concepts, the tropospheric bias remains.

Antenna and RF-Equipment Biases

Main contributions to the LEO and GEO satellite biases and the ground station biases are internal delays of the TX and RX RF-chains as well as phase center variations of the antennas. The ground antenna TX/RX equipment delay can be calibrated with a remaining error of < 0.1 ns, which corresponds to an error of < 3 cm. This was already successfully done for Two-Way Satellite Time and Frequency Transfer (TW-STFT) experiments (cf. Fujieda et al. [2007]). The onboard LEO satellite and GEO satellite equipment can be pre-calibrated on the ground prior to launch and have to be estimated during operation applying thermal models. The LEO satellite attitude as well as the ground station pointing is known. The antenna biases like phase center variations and phase-wind up therefore can be modeled with errors < 1 cm for Ka-band frequencies (cf. Montenbruck et al. [2009] and Wu et al. [1993]).

Table 5.4 summarizes the different noise and error contributions to the pseudorange measurements. Compared to the clock synchronization errors based on the GNSS time synchronization and the LEO satellite positioning accuracy, all remaining contributions are negligible.

		Real-Time	Non-Time Critical	Reference
Stochastic Noise		Standard Deviation		
η^{n}_{LGE}	Pseudorange Measurement Noise	0.3 – 7.4 cm	0.3 – 7.4 cm	[1]
$\delta\vec{r}^{\,n}_{\mathrm{L}}$	GPS-Position of LEO satellite	100 cm[a]	2 cm[a]	[2]
η^{n}_{2W}	Noise of 2W Range Measurement	< 0.5 cm	< 0.5 cm	[3]
Biases		Magnitude		
b^{n}_{L}	TX-Antenna Phase	< 1 cm	< 1 cm	[4]
	TX-Equipment Delay	< 3 cm	< 3 cm	[5]
	GPS-Clock Uncertainty	30 – 90 cm	30 – 90 cm	[6]
b^{n}_{G}	RX-Antenna Phase	< 1 cm	< 1 cm	[4]
	RX-Equipment Delay	< 3 cm	< 3 cm	[5]
	TX-Antenna Phase	< 1 cm	< 1 cm	[4]
	TX-Equipment Delay	< 3 cm	< 3 cm	[5]
T_{GE}	Tropospheric Delay	1 – 10 cm[b]	1 – 10 cm[b]	[7]
I_{GE}	Ionospheric Delay	< 1 cm[b]	< 1 cm[b]	[8]
I_{LG}	Ionospheric Delay	< 1 cm	< 1 cm	[8]
$b^{n}_{\mathrm{E,RX}}$	RX-Equipment Delay	< 3 cm	< 3 cm	[4]
	RX/TX-Antenna Phase	< 1 cm	< 1 cm	[5]
	Ground Station Position	< 1 cm	< 1 cm	[9]
	GPS-Clock Uncertainty	- [c]	- [c]	[4]
$b^{n}_{\mathrm{E,TX}}$	TX-Equipment Delay	< 3 cm	< 3 cm	[4]
	RX/TX-Antenna Phase	< 1 cm	< 1 cm	[5]
	Ground Station Position	< 1 cm	< 1 cm	[9]
	GPS-Clock Uncertainty	- [c]	- [c]	[4]

[a] The LEO satellite position is assumed to be measured for each epoch. Therefore its error is treated as white Gaussian noise in the simulations. [b] Not relevant for the LEO satellite based positioning concept. [c] The clock synchronization error between the LEO satellites and the ground station is completely mapped into the clock error on the LEO satellites.

Table 5.4: Influences of the different noise and error terms on the pseudorange accuracy. The atmospheric influences on the LEO-GEO-Earth (LGE) pseudorange are canceled due to the Earth-GEO two-way measurement.

---

[1] cf. Table 5.2, [2] Roselló et al. [2012], [3] CRB of GEO-Earth link (cf. Table 5.2), [4] Montenbruck et al. [2009], Wu et al. [1993], [5] Fujieda et al. [2007], [6] Nie et al. [2007], Furthner et al. [2003], [7] Martellucci [2002], [8] See frequency dependency of the ionosphere, cf. Allain and Mitchell [2008], [9] IGS Central Bureau [2013]

5.2.3 Pseudorange Models

The analysis of the pseudorange noise and error statistics in the previous section showed that some terms in the pseudorange model of Equation (5.2) for the LEO-GEO-Earth (LGE) measurements have only negligible influence. Considering these results, the pseudorange models for the LEO-GEO-Earth link, the two-way Earth-GEO link and the GNSS-LEO link are described and simplified in the following paragraph. For completeness, the LEO-GEO-Earth pseudorange model is shown again.

LEO-GEO-Earth link

$$\begin{aligned}\rho^n_{\mathrm{LGE}} =& \|\vec{r}_{\mathrm{G}} - \vec{r}^{\,n}_{\mathrm{L}}\| + \|\vec{r}_{\mathrm{E}} - \vec{r}_{\mathrm{G}}\| + I^n_{\mathrm{LG}} + b^n_{\mathrm{L}} \\ &+ b^n_{\mathrm{G}} + I^n_{\mathrm{GE}} + T_{\mathrm{GE}} + b^n_{\mathrm{E,RX}} + \eta^n_{\mathrm{LGE}},\end{aligned} \tag{5.4}$$

The ionospheric path delay in Ka-band can be bound to < 1 cm as explained in the previous section and has only a negligible impact. Under this assumption the pseudorange model is simplified to

$$\rho^n_{\mathrm{LGE}} = \|\vec{r}_{\mathrm{G}} - \vec{r}^{\,n}_{\mathrm{L}}\| + \|\vec{r}_{\mathrm{E}} - \vec{r}_{\mathrm{G}}\| + b^n_{\mathrm{L}} + b^n_{\mathrm{G}} + T_{\mathrm{GE}} + b^n_{\mathrm{E,RX}} + \eta^n_{\mathrm{LGE}}. \tag{5.5}$$

GEO-Earth two-way link

The pseudorange model for the two-way Earth-GEO measurements is defined as

$$\rho^n_{\mathrm{2W}} = 2\left(\|\vec{r}_{\mathrm{E}} - \vec{r}_{\mathrm{G}}\| + T_{\mathrm{GE}}\right) + I^n_{\mathrm{GE,up}} + I^n_{\mathrm{GE,down}} + b^n_{\mathrm{E,TX}} + b^n_{\mathrm{G}} + b^n_{\mathrm{E,RX}} + \eta^n_{\mathrm{2W}}, \tag{5.6}$$

with $b^n_{\mathrm{E,TX}}$ the ground station transmitter bias and η^n_{2W} the ground station receiver noise for the two-way measurements at each n frequencies. In Equation 5.6 the rotation of the Earth is neglected but has to be considered by an approximation like applied for GNSS positioning.

As the time between the uplink and downlink of the signal is very short, the troposphere and ionosphere are treated as static. The ionospheric path delay in Ka-band can be neglected as explained above. Therefore, Equation (5.6) is simplified to

$$\rho^n_{\mathrm{2W}} = 2\left(\|\vec{r}_{\mathrm{E}} - \vec{r}_{\mathrm{G}}\| + T_{\mathrm{GE}}\right) + b^n_{\mathrm{E,TX}} + b^n_{\mathrm{G}} + b^n_{\mathrm{E,RX}} + \eta^n_{\mathrm{2W}}, \tag{5.7}$$

GNSS-LEO link

The LEO satellites are assumed to carry space born high precision GNSS receivers. The pseudoranges $\rho^{k,n}_{\mathrm{SL}}$ between the kth GNSS satellite and the nth LEO satellite, used to estimate the nth LEO satellite position and clock, are

$$\rho^{k,n}_{\mathrm{SL}} = \|\vec{r}^{\,n}_{\mathrm{L}} - \vec{r}^{\,k}_{\mathrm{S}}\| + c\left(\delta^n_{\mathrm{L}} - \delta^k_{\mathrm{S}}\right) + b^{k,n}_{\mathrm{SL}} + \eta^{k,n}_{\mathrm{SL}}, \tag{5.8}$$

with the index S for the GNSS satellite related variables.

In order to reduce the complexity of the system of equations, the following simplifications are applied:

- The LEO satellite position estimation is performed separately and no longer part of the system of equations. The $\vec{r}_{\mathrm{L}}^{n}$ are assumed to be known with uncertainties $\delta\vec{r}_{\mathrm{L}}^{n}$ of standard deviation $(\sigma_{\mathrm{L}}^{n})^2$.
- The biases are approximated to be constant for a sufficient amount of time (see explanation in Section 5.3.1).
- The two-way pseudorange measurements ρ_{2W}^{n} are used to separate the LEO-GEO pseudoranges from the LEO-GEO-Earth pseudoranges. The result is a simplified model for the LEO-GEO pseudoranges:

  $$\rho_{\mathrm{LG}}^{n} = \rho_{\mathrm{LGE}}^{n} - \frac{1}{2}\rho_{\mathrm{2W}}^{n} = \|\vec{r}_{\mathrm{G}} - \vec{r}_{\mathrm{L}}^{n}\| + \widetilde{b}_{\mathrm{LG}}^{n} + \widetilde{\eta}_{\mathrm{LG}}^{n}, \tag{5.9}$$

  where combined biases $\widetilde{b}_{\mathrm{LG}}^{n} = b_{\mathrm{L}}^{n} - \frac{1}{2}(b_{\mathrm{E,TX}}^{n} - b_{\mathrm{E,RX}}^{n} - b_{\mathrm{G}}^{n})$ and a combined noise $\widetilde{\eta}_{\mathrm{LG}}^{n}$ with standard deviation $\sigma_{\mathrm{LG}}^{n} = \sqrt{(\sigma_{\mathrm{LGE}}^{n})^2 + (\sigma_{\mathrm{2W}}^{n})^2}$ remain. The biases $\widetilde{b}_{\mathrm{LG}}^{n}$ are dominated by the LEO satellite biases b_{L}^{n} with main contribution of the clock biases.

The proposed simplifications slightly reduce the accuracy of the positioning solution, but are used for determining a lower bound on the achievable positioning error.

For a set of measurements of T time steps and N LEO satellites,

$$T \cdot N \quad \text{Equations} \quad \rho_{\mathrm{LG}}^{n} = \|\vec{r}_{\mathrm{G}} - \vec{r}_{\mathrm{L}}^{n}\| + \widetilde{b}_{\mathrm{LG}}^{n} + \widetilde{\eta}_{\mathrm{LG}}^{n}$$

are available to solve for

$$T \cdot 3 \quad \text{slow varying components of the GEO satellite position } \vec{r}_{\mathrm{G}}(t)$$

and

$$N \quad \text{constant biases } \widetilde{b}_{\mathrm{LG}}^{n}.$$

For $T \geq \frac{N}{N-3}$ (for $N > 3$) equations, the system of equations is solvable. A method to solve the system is the standard Least-Squares estimation already applied in Section 4.2 and known from GNSS positioning problems. However, a Least-Squares solution only provides a noisy estimate of $\vec{r}_{\mathrm{G}}$ as it can not separate effectively the slow varying position estimates from the constant biases. In order to separate the biases from the positioning solution a Kalman filter approach is proposed. The algorithms are explained in the following section.

5.2.4 Positioning Solution

Least-Squares

The position estimation of the GEO satellite using the pseudorange measurements from Equation (5.9) is solved by linearization. The standard Least-Squares approach known from GNSS positioning solutions is applied (cf. Misra and Enge [2012] or Kaplan and Hegarty [2006]). The measurement model containing the measurements ρ of T time steps, the state vector ξ, the noise η and the mapping H of the state vector to the measurements, is defined as

$$\underbrace{\begin{pmatrix}\overline{\rho}_1\\ \vdots\\ \overline{\rho}_T\end{pmatrix}}_{\rho} = \underbrace{\left(\begin{array}{ccc|c}\overline{H}_1 & & & \mathbb{1}^{N\times N}\\ & \ddots & & \vdots\\ & & \overline{H}_T & \mathbb{1}^{N\times N}\end{array}\right)}_{H} \underbrace{\begin{pmatrix}\vec{r}_{\mathrm{G}}(1)\\ \vdots\\ \vec{r}_{\mathrm{G}}(T)\\ \overline{b}\end{pmatrix}}_{\xi} + \underbrace{\begin{pmatrix}\overline{\eta}_1\\ \vdots\\ \overline{\eta}_T\end{pmatrix}}_{\eta}, \tag{5.10}$$

where

$$\overline{\rho}_t = \begin{pmatrix}\rho^1_{\mathrm{LG}}(t) + \left(\vec{e}^{\,1}(t)\right)^{\mathrm{T}} \vec{r}^{\,1}_{\mathrm{L}}(t)\\ \vdots\\ \rho^N_{\mathrm{LG}}(t) + \left(\vec{e}^{\,N}(t)\right)^{\mathrm{T}} \vec{r}^{\,N}_{\mathrm{L}}(t)\end{pmatrix}$$

with

$$\|\vec{r}_{\mathrm{G}} - \vec{r}^{\,n}_{\mathrm{L}}\| = \frac{(\vec{r}_{\mathrm{G}} - \vec{r}^{\,n}_{\mathrm{L}})}{\|\vec{r}_{\mathrm{G}} - \vec{r}^{\,n}_{\mathrm{L}}\|} \cdot (\vec{r}_{\mathrm{G}} - \vec{r}^{\,n}_{\mathrm{L}}) = \vec{e}^{\,n} \cdot (\vec{r}_{\mathrm{G}} - \vec{r}^{\,n}_{\mathrm{L}})\,.$$

Furthermore, it is

$$\overline{H}_t = \begin{pmatrix}\left(\vec{e}^{\,1}_{\mathrm{LG}}(t)\right)^{\mathrm{T}}\\ \vdots\\ \left(\vec{e}^{\,N}_{\mathrm{LG}}(t)\right)^{\mathrm{T}}\end{pmatrix}, \quad \overline{b} = \begin{pmatrix}\widetilde{b}^1_{\mathrm{LG}}\\ \vdots\\ \widetilde{b}^N_{\mathrm{LG}}\end{pmatrix}, \quad \text{and} \quad \overline{\eta}_t = \begin{pmatrix}\widetilde{\eta}^1_{\mathrm{LG}}(t)\\ \vdots\\ \widetilde{\eta}^N_{\mathrm{LG}}(t)\end{pmatrix}. \tag{5.11}$$

A maximum likelihood estimation for Equation (5.10) is possible for $T \geq \frac{N}{N-3}$ (for the number of LEO satellites $N > 3$). It reads as

$$\arg\min_{\xi} \|\rho - H\xi\|^2_W \tag{5.12}$$

with a weighting matrix $W = C^{-1}$, where C includes the covariances of the pseudorange measurements ρ.

The solution to Equation (5.12), i.e. the estimate $\hat{\xi}$ of ξ, is calculated by

$$\hat{\xi} = \left(H^{\mathrm{T}}WH\right)^{-1} H^{\mathrm{T}}W\rho, \tag{5.13}$$

provided that $H^{\mathrm{T}}WH$ is non-singular and well conditioned.

Kalman Filter

Due to the high dynamics of the LEO satellite constellation, the residual biases $\widetilde{b}^n_{\mathrm{LG}}$ dominated by the LEO satellite biases can be estimated effectively by applying a filter. The relative movement of the GEO satellite in an Earth Centered Earth Fixed (ECEF) coordinate system is very small (< 25 cm/s). Therefore, a linear state space model is applied to describe the state transitions. Ideally, T is $T = 1$, but due to implementation constraints, T might also be $T > 1$:

$$\underbrace{\begin{pmatrix} \vec{r}_{\mathrm{G},s}(1) \\ \vdots \\ \vec{r}_{\mathrm{G},s}(T) \\ \dot{\vec{r}}_{\mathrm{G},s}(1) \\ \vdots \\ \dot{\vec{r}}_{\mathrm{G},s}(T) \\ \overline{b}_s \end{pmatrix}}_{x_s} = \underbrace{\begin{pmatrix} \mathbb{1}^{3T\times 3T} & \Delta t \cdot \mathbb{1}^{3T\times 3T} & 0^{3T\times N} \\ 0^{3T\times 3T} & \mathbb{1}^{3T\times 3T} & 0^{3T\times N} \\ 0^{N\times 3T} & 0^{N\times 3T} & \mathbb{1}^{N\times N} \end{pmatrix}}_{F_s} \underbrace{\begin{pmatrix} \vec{r}_{\mathrm{G},s-1}(1) \\ \vdots \\ \vec{r}_{\mathrm{G},s-1}(T) \\ \dot{\vec{r}}_{\mathrm{G},s-1}(1) \\ \vdots \\ \dot{\vec{r}}_{\mathrm{G},s-1}(T) \\ \overline{b}_{s-1} \end{pmatrix}}_{x_{s-1}} + \underbrace{\begin{pmatrix} \vec{w}_{\vec{r}_{\mathrm{G}},s}(1) \\ \vdots \\ \vec{w}_{\vec{r}_{\mathrm{G}},s}(T) \\ \vec{w}_{\dot{\vec{r}}_{\mathrm{G}},s}(1) \\ \vdots \\ \vec{w}_{\dot{\vec{r}}_{\mathrm{G}},s}(T) \\ \overline{w}_{b,s} \end{pmatrix}}_{w_s},$$

with the state transition matrix F_s and the Gaussian noise $w_s \sim \mathcal{N}(0, Q_s)$, where

$$Q_s = \begin{pmatrix} \sigma^2 \frac{\Delta t^3}{3} \cdot \mathbb{1}^{3T\times 3T} & \sigma^2 \frac{\Delta t^2}{2} \cdot \mathbb{1}^{3T\times 3T} & 0^{3T\times N} \\ \sigma^2 \frac{\Delta t^2}{2} \cdot \mathbb{1}^{3T\times 3T} & \sigma^2 \Delta t \cdot \mathbb{1}^{3T\times 3T} & 0^{3T\times N} \\ 0^{N\times 3T} & 0^{N\times 3T} & \sigma_b^2 \Delta t \cdot \mathbb{1}^{N\times N} \end{pmatrix}. \tag{5.14}$$

The process noise σ^2 and σ_b^2 is chosen to track all higher order derivative terms.

The measurement model shown in Equation (5.10) has to be adapted to

$$\underbrace{\begin{pmatrix} \overline{\rho}_{1,s} \\ \vdots \\ \overline{\rho}_{T,s} \end{pmatrix}}_{z_s} = \underbrace{\left(\begin{array}{ccc|ccc|c} \overline{H}_{1,s} & & & 0_1^{N\times 3} & & & \mathbb{1}^{N\times N} \\ & \ddots & & & \ddots & & \vdots \\ & & \overline{H}_{T,s} & & & 0_T^{N\times 3} & \mathbb{1}^{N\times N} \end{array}\right)}_{H_s} \underbrace{\begin{pmatrix} \vec{r}_{\mathrm{G,s}}(1) \\ \vdots \\ \vec{r}_{\mathrm{G,s}}(T) \\ \dot{\vec{r}}_{\mathrm{G,s}}(1) \\ \vdots \\ \dot{\vec{r}}_{\mathrm{G,s}}(T) \\ \overline{b}_s \end{pmatrix}}_{x_s} + \underbrace{\begin{pmatrix} \overline{\eta}_{1,s} \\ \vdots \\ \overline{\eta}_{T,s} \end{pmatrix}}_{v_s},$$

in order to include the velocity in the state vector.

A Kalman filter represents an optimum filter in the sense that it minimizes the mean square error for a Gauss-Markov sequence (cf. Brown and Hwang [1997]). It is therefore an optimum filter for the GEO satellite positioning estimation and is described by the following equations:

$$\begin{aligned} \text{Prediction:} \quad \hat{x}_s^- &= F_s \hat{x}_{s-1}^+ \\ P_{\hat{x}_s^-} &= F_s P_{\hat{x}_{s-1}^+} F_s^{\mathrm{T}} + Q_s \\[2em] \text{Update:} \quad \hat{x}_s^+ &= \hat{x}_s^- + K_s \left(z_s - H_s \hat{x}_s^- \right) \\ P_{\hat{x}_s^+} &= \left(\mathbb{1} - K_s H_s \right) P_{\hat{x}_s^-} . \end{aligned} \tag{5.15}$$

with $K_s = P_{\hat{x}_s^-} H_s^{\mathrm{T}} \left(H_s P_{\hat{x}_s^-} H_s^{\mathrm{T}} + W_s^{-1} \right)^{-1}$, where W_s includes the covariances of the pseudorange measurements.

The predicted or *a priori* estimate covariance matrix $P_{\hat{x}_s^-}$ is initialized by the covariance matrix $P_{\hat{x}_0^-} = \left(H_0^{\mathrm{T}} W_0 H_0 \right)^{-1}$ of the Least-Squares estimation in the first step. Also the state estimate $\hat{x}_s^+$ is initialized by the Least-Squares estimate in the first step.

Rauch-Tung-Striebel Smoother

The Kalman filter provides a statistically optimum estimate for the GEO satellite positions by recursively operating on a temporal stream of noisy measurement data. The algorithm considers the past states to find the solution for the future state. The filtered GEO satellite positions can be optimized further for non-time critical (NTC) applications by considering the progression of all states within a certain interval. This is achieved applying a Kalman smoother which recursively passes all Kalman filtered states backwards in time. An efficient implementation is the Rauch-Tung-Striebel (RTS) smoother (cf. Rauch et al. [1965]). The forward pass is the regular Kalman filter algorithm as explained in Equation (5.15). The filtered state and covariance predictions $\hat{x}_s^-, P_{\hat{x}_s^-}$ and state and covariance estimates $\hat{x}_s^+, P_{\hat{x}_s^+}$ are saved during the Kalman filter process and are used in the subsequent backward pass. The backward pass leading to the smoothed states $\hat{x}_s$ reads as follows

$$\begin{aligned} \hat{x}_s &= \hat{x}_s^+ + C_s (\hat{x}_{s+1} - \hat{x}_{s+1}^-) \\ P_{\hat{x}_s} &= P_{\hat{x}_s^+} + C_s (P_{\hat{x}_{s+1}} - P_{\hat{x}_{s+1}^-}) C_s^{\mathrm{T}}, \end{aligned}$$

with the smoother gain $C_s = P_{\hat{x}_s^+} F_s^{\mathrm{T}} (P_{\hat{x}_{s+1}^-})^{-1}$.

The initial values for $\hat{x}_s$ and $P_{\hat{x}_s}$ in the first step of the algorithm are the Kalman filtered state vector and covariance matrix $\hat{x}_s^+, P_{\hat{x}_s^+}$ of the last time step of the considered interval.

5.3 Simulation and Results

5.3.1 Simulation Environment and Scenario

The applied scenario for the following simulations consists of a LEO satellite constellation containing 15 satellites (cf. Table 5.5) and one GEO satellite above Europe (longitude of 10°). It is visualized in Figure 5.7. The LEO constellation forms a representative selection considering altitude and inclination out of all approximately 400 LEO satellites currently in space (see Section 2.1.1). The LEO satellites appear in a cone of ±10° as seen from the GEO satellite. An antenna located at the campus of the Technische Universität München (TUM) (N 48.151041°, E 11.568431°) in Munich is assumed as ground station.

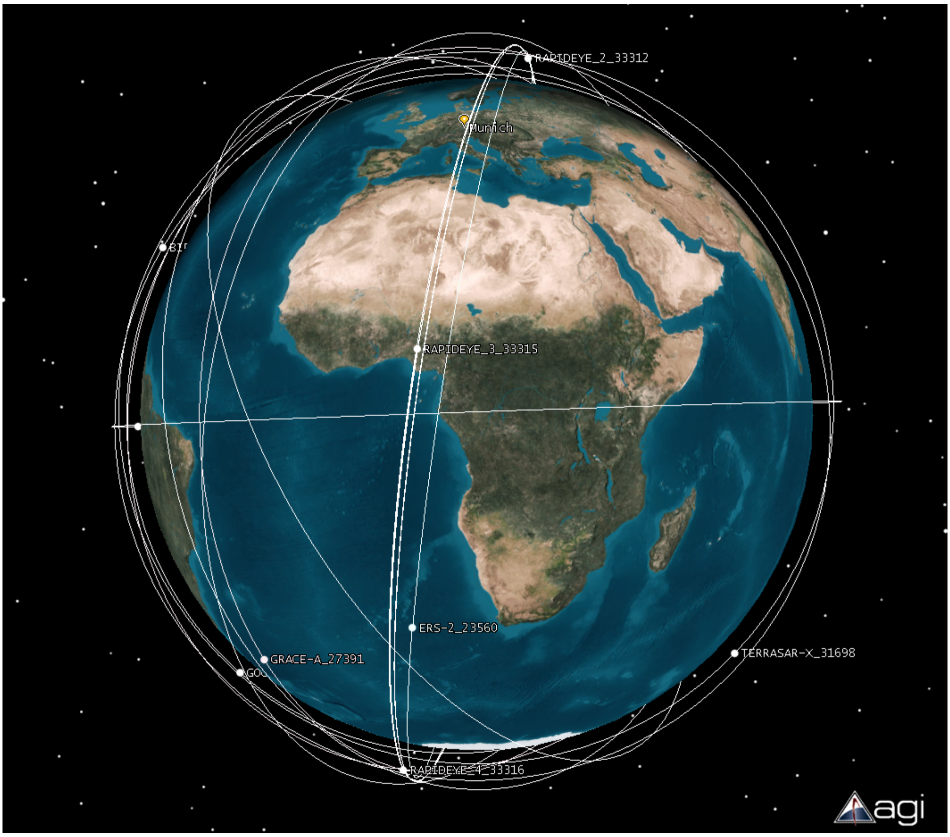

Figure 5.7: The 15 LEO satellite constellation shown in Table 5.5 used for the simulation scenario. The satellites form a representative selection according to the results of Section 2.1.1.

LEO Satellite Name	Apogee	Perigee	Inclination
AGILE	540 km	513 km	2.5 deg
BIRD_2	536 km	514 km	97.8 deg
ERS-2	785 km	783 km	98.5 deg
GOCE	265 km	251 km	96.6 deg
GRACE-A	474 km	452 km	89.0 deg
METOP-A	821 km	820 km	98.7 deg
PROBA	655 km	542 km	97.6 deg
RAPIDEYE_1	648 km	611 km	98.0 deg
RAPIDEYE_2	639 km	620 km	98.0 deg
RAPIDEYE_3	639 km	620 km	98.0 deg
RAPIDEYE_4	638 km	621 km	98.0 deg
RAPIDEYE_5	642 km	617 km	98.0 deg
RUBIN-2	711 km	592 km	64.6 deg
TERRASAR-X	509 km	507 km	97.5 deg
TOPSAT	706 km	682 km	98.0 deg

Table 5.5: Representative selection of 15 LEO satellites used in the following simulations for geostationary data relay position estimation.

The LEO-GEO pseudoranges are modeled using Equation (5.9). The parameters for the creation of the pseudoranges are shown in Table 5.6. In order to consider the uncertainty of the estimated LEO satellite position in the GEO satellite position estimation process, the implemented measurement model for the pseudorange estimation reads as

$$\rho_{\mathrm{LG}}^{n} = \|\vec{r}_{\mathrm{G,\ true}} - (\vec{r}_{\mathrm{L,true}}^{\,n} + \delta\vec{r}_{\mathrm{L}}^{\,n})\| + \widetilde{b}_{\mathrm{LG}}^{n} + \widetilde{\eta}_{\mathrm{LG}}^{n}, \tag{5.16}$$

where the LEO satellite position uncertainty $\delta\vec{r}_{\mathrm{L}}^{\,n}$ is considered as zero mean Gaussian noise on the true LEO satellite position.

Stochastic Noise	Standard Deviation
$\widetilde{\eta}_{\mathrm{LG}}^{n}$, Combined Receiver Noise	1 cm
$\delta\vec{r}_{\mathrm{L}}^{\,n}$, LEO Satellite Position Error:	
- Real-Time	100 cm
- Slow-Time Critical (1-2 days)	5 cm
- Non-Time Critical (1 month)	2 cm
Biases	**Magnitude**
$\widetilde{b}_{\mathrm{LG}}^{n}$, Worst Case Sum of all Biases	113 cm

Table 5.6: Error models for the pseudorange simulations with assumed real-time, slow-time critical and non-time critical provision of the LEO satellite positions.

Ranges

The true GEO and LEO satellite positions are determined according to the AGI STK satellite orbits. The orbits are calculated using the High Precision Orbit Propagator (HPOP) (cf. AGI STK [2013]) including the following models:

- The Earth geoid is based on the EGM96 model with degree and order 21, full solid tides and ocean tides.
- Third body gravitational influences from all planets are considered as well as solar radiation pressure and atmospheric drag.

The uncertainty in the assumed LEO satellite positions is considered according to the overview shown in Section 5.2.2.

Biases

The biases are modeled following the derivations in Section 5.2.2, summarized in Table 5.6. The dominant contribution is the clock synchronization error of approximately 90 cm. Summing up all biases of Table 5.4 leads to a worst case bias of 113 cm. The biases are approximated to be constant during the measurement process, which can be considered a good approximation for sun synchronous satellites (cf. Section 2.1). Sun synchronous satellites are illuminated by the sun constantly. They don't experience large variations in temperature, which are assumed to be the main source for non-modeled bias drifts.

Receiver Noise

The LEO-GEO link is modeled as a telemetry link with 2.3 MHz bandwidth per satellite and a LEO satellite equipment as defined for "System 2" in Table 5.2. The GEO-Earth link is modeled applying the ITU-Recommendations for atmosphere models, i.e. the rain model according to ITU-R P.618-9 and the atmospheric absorption model according to ITU-R P.675-5. A mean link budget for the LEO-GEO-Earth link calculated according to Appendix A is shown in Table 5.7. Since the C/N_0 on the LEO-GEO link is much smaller than the one on the GEO-Earth link, the LEO-GEO link dominates the overall link-budget. The C/N_0 of 61.9 dBHz enables to transmit data with a data-rate of at least 1 Mbit/s (cf. Katona [2012]).

The correlation block length is set to 60 s. The receiver noise $\widetilde{\eta}_{\mathrm{LG}}^{n}$ is simulated as zero mean Gaussian noise with standard deviation according to the Cramér-Rao bounds of the single measurements (cf. Section 5.2.1). The Cramér-Rao Bound for the LEO-GEO pseudoranges is approximately 0.9 cm and < 0.5 cm for the two-way measurement. This leads to a combined receiver noise in the measurement model of approximately 1 cm. Therefore, the timing estimation is not a limiting factor for achieving a high positioning accuracy.

Uplink: LEO-GEO	
Carrier Frequency	27 GHz
LEO TX Antenna Diameter	0.5 m
LEO TX Antenna Gain	40.8 dBi
LEO TX power	50.0 W
LEO EIRP	56.8 dBW
Worst Case Free Space Loss	213.4 dB
GEO RX Global Horn Gain	18.0 dBi
GEO RX System Noise Temperature	550 K
GEO RX G/T	-10.1 dB/K
C/N_0	61.9 dBHz
Downlink: GEO-Earth	
Carrier Frequency	27 GHz
GEO TX Antenna Diameter	0.8 m
GEO TX Antenna Gain	44.9 dBi
GEO TX power	25.0 W
GEO EIRP	57.9 dBW
Free Space Loss	212.7 dB
Atmospheric Loss	1.4 dB
Rain Loss (99.9% availability)	13.4 dB
Earth RX Antenna Diameter	5.0 m
Earth RX Gain	60.8 dBi
Earth RX System Noise Temperature	380 K
Earth RX G/T	34.0 dB/K
C/N_0	93.0 dBHz
Overall C/N_0	61.9 dBHz

Table 5.7: Link budget for the telemetry link of a LEO satellite via a geostationary data relay to a ground station at Munich.

The simulations are performed in Matlab with an interface to the System Tool Kit (STK) software from AGI. Figure 5.8 shows the flow of the simulation code. A Least-Squares estimation as well as a Kalman filter implementation are performed, in order to compare the solutions. For the NTC and STC scenarios, an RTS smoother was implemented in addition. The simulation results are presented in the following sections.

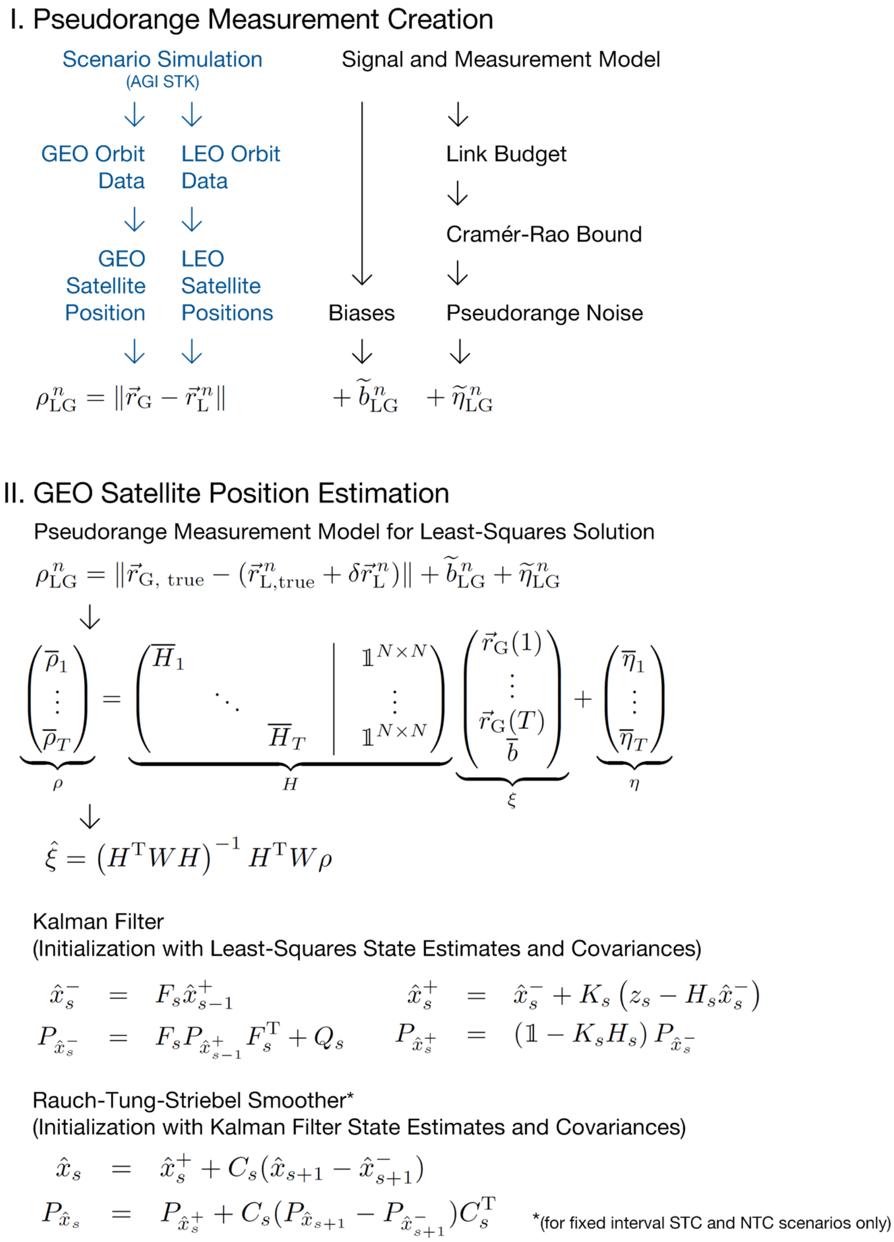

Figure 5.8: Flow chart illustrating the separate steps of the simulation algorithm. The satellite orbital positions and the noise are updated for each measurement step while the biases are fixed after initialization. Details about the Least-Squares algorithm, the Kalman filter and the RTS smoother are found in Section 5.2.4.

5.3.2 Simulation and Analysis of the Dilution of Precision

Besides the pseudorange noise and error, the orbital distribution of the satellites plays a decisive role for the reachable positioning accuracy. Before simulating the positioning solutions for the geostationary satellite, the dilution of precision is analyzed in the following section.

The Positional Dilution of Precision (PDOP) is a means of measure for the specific additional multiplicative effect of LEO satellite geometry on GEO positioning precision is. It is connected to the position uncertainty as

$$\sigma_{\text{pos}} = \sigma \cdot \text{PDOP}, \tag{5.17}$$

with σ the pseudorange uncertainty under assumption that all signal sources have the same standard deviation of noise.

The PDOP is derived as

$$\text{PDOP} = \text{Tr}\,[Q] = \sqrt{(Q_{11}^2 + Q_{22}^2 + Q_{33}^2)} \tag{5.18}$$

with $Q = R(H^{\text{T}}H)^{-1}R^{-1}$, where H is the geometry matrix defined in Equation (5.11) and R is a rotation matrix to transform the matrix $(H^{\text{T}}H)^{-1}$ into a specific coordinate frame. If the PDOP is separated in radial (RDOP), along-track (ADOP) and cross-track (CDOP) DOP for a geostationary satellite, the rotation matrix R performs a rotation around the z-axis about the longitude of the GEO satellite. The DOP in the different directions reads as

$$\text{RDOP} = \sqrt{Q_{11}^2}, \qquad \text{ADOP} = \sqrt{Q_{22}^2}, \qquad \text{CDOP} = \sqrt{Q_{33}^2}.$$

The following analysis considers a constellation of 15 LEO satellites as presented in Table 5.5. Figure 5.9 shows two extreme examples of the constellation geometry as seen from the geostationary orbit. The left figure shows a very good geometry with all LEO satellites visible, the right figure in contrast shows a very poor geometry with only four satellites visible. A calculation of the PDOP related to both geometries shows a PDOP of approximately 4 for the advantageous LEO satellite geometry with 15 visible satellites and a PDOP of more than 1000 for the poor geometry with only 4 visible LEO satellites.

A simulation of 24 hours leads to the PDOP evolution of Figure 5.10. The mean value for the overall positional dilution of precision over T time steps is defined as

$$\overline{\text{PDOP}} = \frac{1}{T} \cdot \sum_{t=1}^{T} \text{Tr}\,[Q]\,. \tag{5.19}$$

The simulation visualized in Figure 5.10 shows an average PDOP of 5.2.

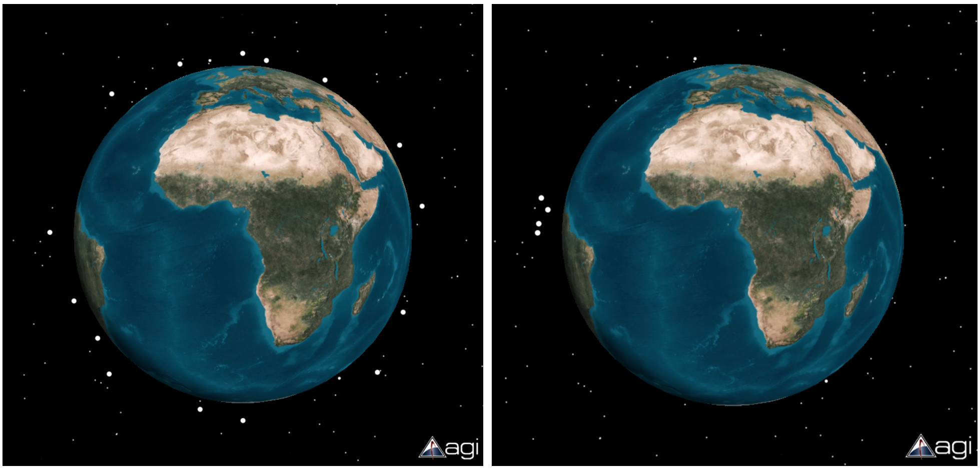

Figure 5.9: *Left:* Advantageous geometry of a 15 LEO satellite constellation for the positioning of a geostationary data relay leading to a PDOP of < 4. *Right:* Poor geometry of a 15 LEO satellite constellation with only 4 visible satellites concentrated within a narrow region leading to a PDOP of > 1000.

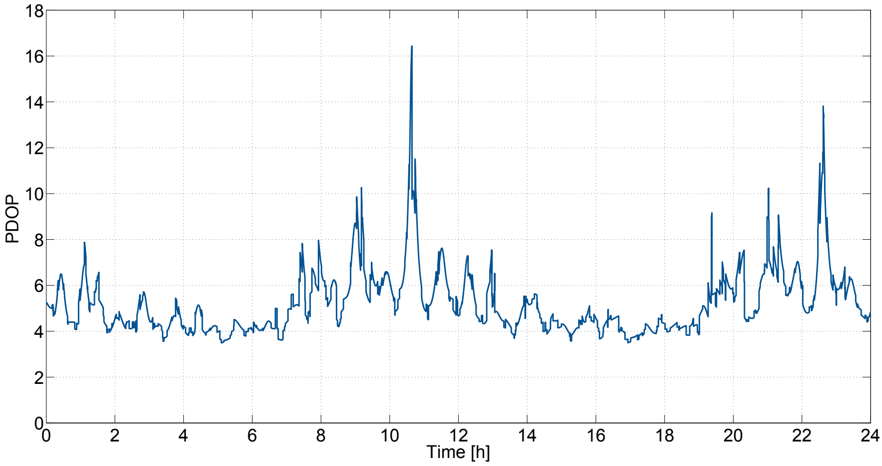

Figure 5.10: PDOP simulation of a 15 LEO satellite constellation. The average PDOP is 5.2.

In addition to the PDOP evolution, the RDOP, ADOP and CDOP evolution is shown in Figure 5.11. As most of the LEO satellites fly in polar orbits, the probability of LEO satellites above the Earth poles is much higher than above the equator (see Section 2.1.1). This leads to larger DOP values in the along-track component compared to the quite small DOP values in the cross-track component. The radial direction shows the largest DOP values since the LEO satellites are only located on one side of the GEO satellite in radial direction. The situation is similar to the one for the VDOP in GNSS positioning. In Figure 5.11, the evolution of the number of visible LEO satellites is shown in addition. A correlation between the number of visible LEO satellites and the change in the dilution of precision is obvious.

The simulation visualized in Figure 5.10 showed a mean PDOP of the 15 LEO satellite constellation of 5.2. A comparison with ground based sources instead of LEO satellites shows a PDOP of 6.2 for the ESA ESTRACK ground station network (9 stations) (cf. Figure 5.5). This is much smaller than the ESA ESTRACK network shows for a pure pseudolite approach, where the PDOP is 142 (cf. Section 5.1.3). The reason is the additional time DOP (TDOP) in the algorithm of the pseudolite approach. The PDOP for GPS receivers on GEO satellites is approximately 25 (cf. Ebinuma et al. [2004]). Common PDOP values for GPS receivers on ground range between $1 - 5$ (cf. Langley [1999]) and for Galileo receivers between $1.6 - 2.9$ (cf. Eissfeller et al. [2007]). Table 5.8 shows an overview of the PDOP of different approaches and constellations.

Constellation	PDOP
15 LEO Satellites ranging approach	
- Mean PDOP	5.2
- Best Case PDOP	< 4
- Worst Case PDOP	> 1000
ESA ESTRACK network (9 stations) for GPS-pseudolite approach	142
ESA ESTRACK network (9 stations) for ranging approach	6.2
GPS in GEO orbit	25
GPS on ground	$1 - 5$
Galileo on ground	$1.6 - 2.9$

Table 5.8: PDOP of the 15 LEO satellite ranging approach and for a ground based GPS-pseudolite and ranging approach. In comparison, the PDOP for the GPS and Galileo constellation for a receiver on the ground is shown.

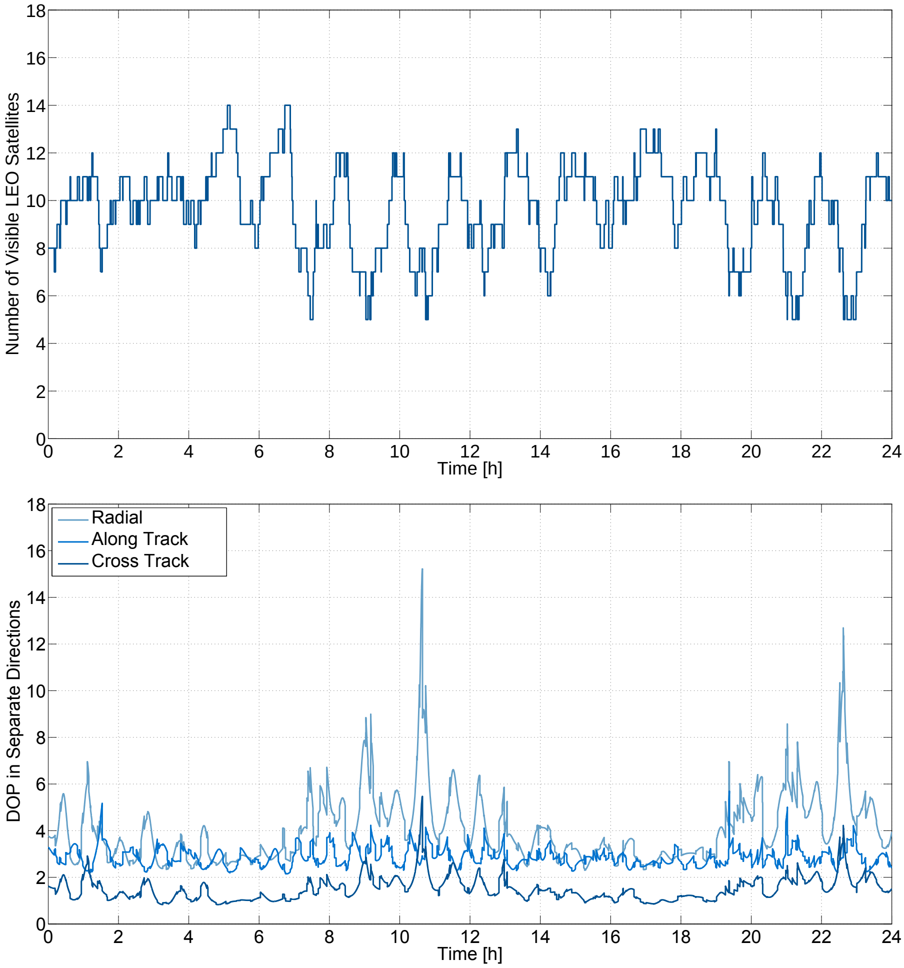

Figure 5.11: DOP of a 15 LEO satellite based positioning solution in radial, along track and cross track direction. The figure on top shows the number of visible LEO satellites over time. A correlation between the number of visible LEO satellites and the change in DOP is obvious.

5.3.3 Simulation and Analysis of the Positioning Solution

The positioning concept for geostationary data relays presented in this thesis was tested in simulations. For the Real-Time (RT), Slow-Time Critical (STC) (1-2 days) and Non-Time Critical (NTC) (1 month) scenarios, different LEO satellite positioning uncertainties were assumed. The simulations are based on the representative LEO satellite constellation containing 15 LEO satellites presented in Table 5.5 and the parameters described in Table 5.6.

The first investigation was about the achievable accuracy of the bias estimation. Figure 5.12 shows the simulation results. On average the estimated biases converge after a period of approximately $50 - 60$ min (measurement rate of 1 Hz). Biases of rising satellites during the bias estimation converge after the rise. The accuracy of the bias estimation is mainly dependent on the accuracy of the LEO satellite position. The biases converge to accuracies in the same order of magnitude as the LEO satellite positions. Simulations show accuracies of approximately 3 cm for the NTC scenario, 5 cm for the STC scenario and 100 cm for the RT scenario. If the approximation of constant biases is valid also for longer periods, like days or months, the biases for RT scenarios might be approximated by the biases with higher accuracy of former STC or even NTC estimation.

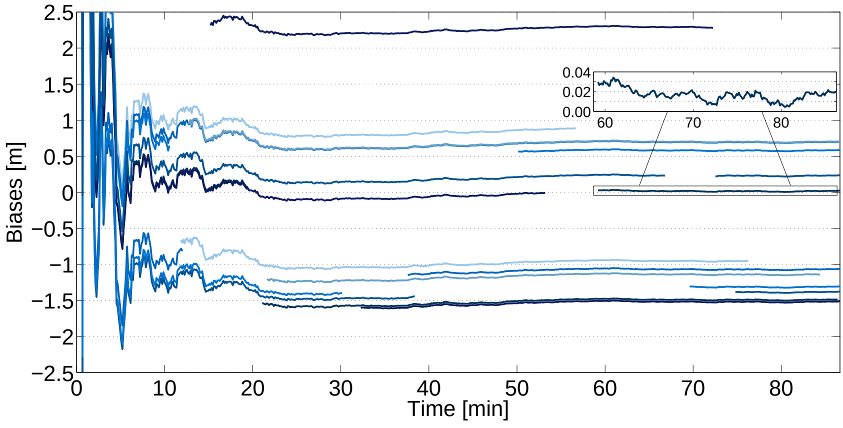

Figure 5.12: Convergence of biases during an NTC simulation with 15 LEO satellites. After approximately $50 - 60$ minutes, the biases of the visible LEO satellites converge with a remaining standard deviation of approximately 3 cm. The biases of LEO satellites rising after the start of the bias estimation converge faster.

After having investigated the bias estimation accuracy, the positioning accuracy is analyzed. Figures 5.13 to 5.15 show the simulation results for the RT, STC and NTC position estimation accuracy in radial, along track and cross track direction. The Least-Squares and Kalman filter results are presented. In addition, the RTS Kalman smoother results are shown for the STC and NTC scenario.

In Section 5.2.3 is derived that a minimum number of $T \geq \frac{N}{N-3}$ epochs for $N > 3$ LEO satellites have to be combined in order to enable a GEO satellite position estimation. If only the minimum number of epochs is combined, simulations show a poor conditioning of the Least-Squares problem, especially when the number of visible satellites is low. One solution is to fix the biases during such periods and only estimate the position. Another solution is to increase T. For the simulations in this thesis, the biases were estimated continuously, while T was selected to $T = 30$ for the NTC and STC scenario and to $T = 60$ for the RT scenario. The measurement rate was 1 Hz.

As expected, the NTC scenario shows the highest positioning accuracy. The GEO satellite positioning accuracy suffers when the LEO satellite position uncertainty increases. The mean values and their accordant standard deviation for the different scenarios are shown in Table 5.9.

The simulation results of all scenarios show the largest positioning uncertainty of the Least-Squares solution in radial direction and the smallest positioning uncertainty in the cross track directions. This is explained by the correlation of the positioning uncertainties σ_{pos} with the Dilution of Precision, $\sigma_{\text{pos}} = \sigma \cdot \text{PDOP}$. The reasons for the variations in the DOP and the differences in the magnitude in the separate directions are explained in the previous Section 5.3.2. The Kalman-Filter solution shows the smallest error in radial direction since the dynamics in the radial component is the lowest. Therefore, the linear filter model applies best.

In Section 5.2.3 simplifications to the positioning concept are applied in order to reduce the complexity. This implies a slight reduction of the positioning accuracy. An extension of the concept might improve the positioning accuracy in radial direction. The approach would be to explicitly exploit the information of the ranging measurements of Equation 5.7 by solving a system of equations including Equation 5.5 and Equation 5.7.

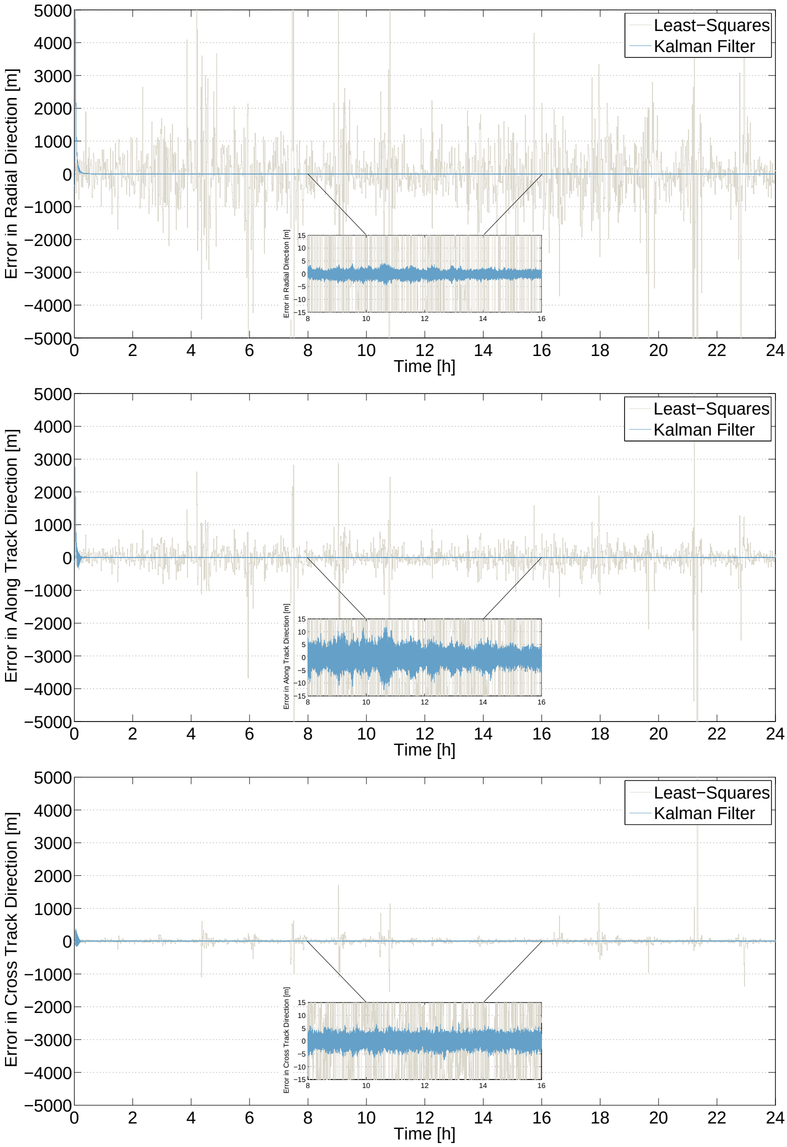

Figure 5.13: Positioning accuracy of a geostationary data relay in an RT simulation, based on the scenario presented in Section 5.3.1. The plots show the Least-Squares solution errors (gray line) and the Kalman filter solution errors (light blue line) in radial, along track and cross track direction. An RTS smoother solution is not applicable for RT scenarios.

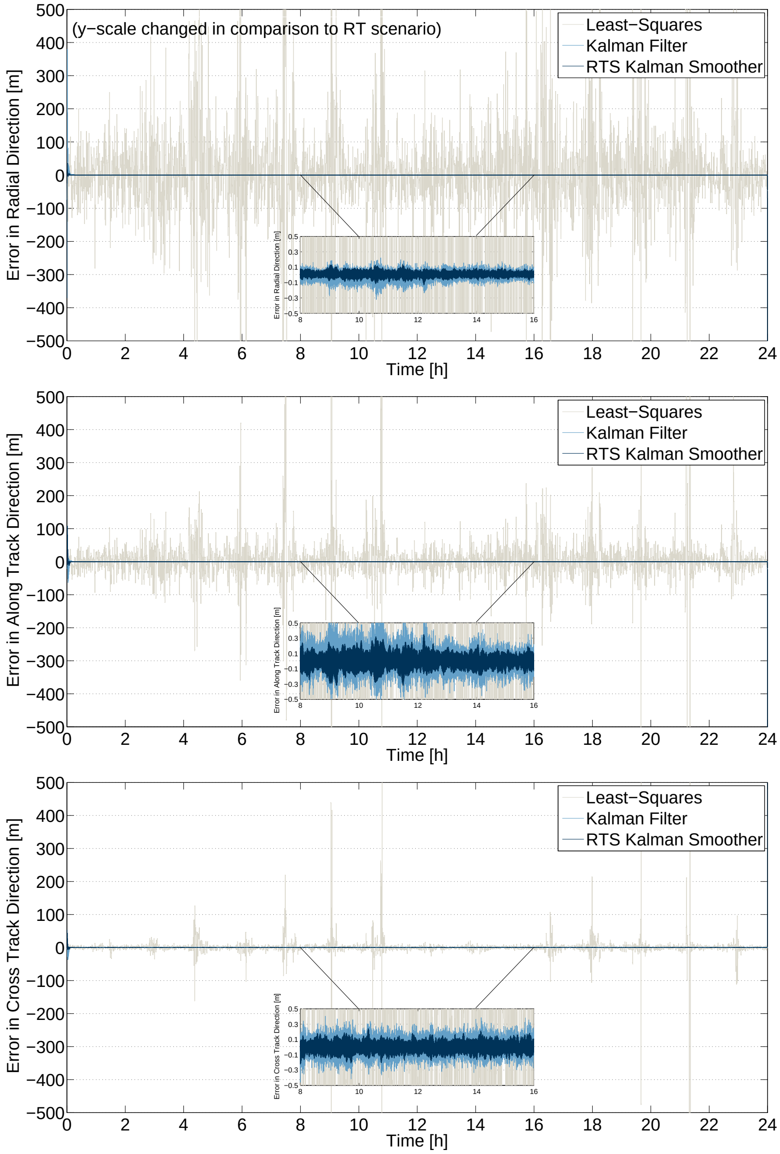

Figure 5.14: Positioning accuracy of a geostationary data relay in an STC simulation, based on the scenario presented in Section 5.3.1. The plots show the Least-Squares solution errors (gray line), the Kalman filter solution errors (light blue line) and the RTS smoother error (dark blue line) in radial, along track and cross track direction. The y-scale is zoomed in compared to the RT Figures.

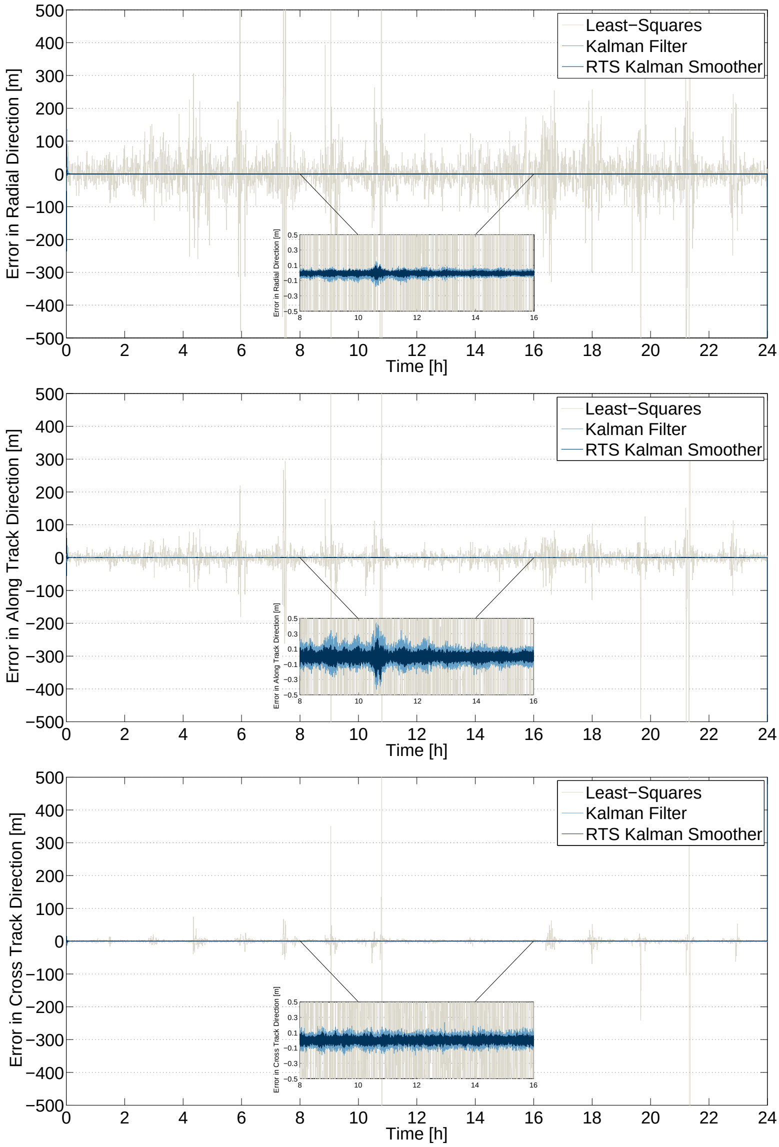

Figure 5.15: Positioning accuracy of a geostationary data relay in an NTC simulation, based on the scenario presented in Section 5.3.1. The plots show the Least-Squares solution errors (gray line), the Kalman filter solution errors (light blue line) and the RTS smoother error (dark blue line) in radial, along track and cross track direction. The y-scale is zoomed in compared to the RT Figures.

	Mean Positioning Error			Standard Deviation		
NTC Scenario	Radial	Al. Track	Cr. Track	Radial	Al. Track	Cr. Track
Least-Squares	−0.6 m	0.5 m	0.3 m	99 m	21 m	16 m
Kalman Filter	−1.4 cm	0.6 cm	0.0 cm	2.0 cm	7.3 cm	4.8 cm
RTS Smoother	−0.3 cm	0.0 cm	0.0 cm	0.9 cm	4.1 cm	2.8 cm
STC scenario	Radial	Al. Track	Cr. Track	Radial	Al. Track	Cr. Track
Least-Squares	15 m	2.4 m	1.3 m	400 m	66 m	59 m
Kalman Filter	0.8 cm	2.5 cm	0.2 cm	3.1 cm	14 cm	9.6 cm
RTS Smoother	1.2 cm	0.4 cm	0.0 cm	1.7 cm	7.6 cm	5.3 cm
RT Scenario	Radial	Al. Track	Cr. Track	Radial	Al. Track	Cr. Track
Least-Squares	58 m	19 m	10 m	1200 m	260 m	190 m
Kalman Filter	2.6 cm	16.4 cm	2.4 cm	57 cm	250 cm	170 cm

Table 5.9: Simulated positioning accuracies for the NTC, STC and RT scenario.

5.3.4 Comparison to a Ground Based Variant

The concept for GEO satellite positioning applied in the previous section is based on the use of LEO satellite signals. A variant to this concept is substituting the LEO satellites with ground terminals. This variant is similar to the pseudolite approach presented in Section 5.1.3. The main difference, however, is the separated time synchronization by GNSS services which overcomes the problem of large PDOP described in Section 5.1.3. Furthermore, a higher carrier frequency (Ka-band instead of L-band) mitigates the influence of the ionosphere.

Table 5.10 shows a comparison between the ground based method and the LEO satellite based method. The main difference between the two is the missing dynamics in the Ground-GEO constellation, which inhibits an effective bias estimation. However, the biases are smaller than for the LEO satellite based solution due to higher positioning and clock synchronization accuracy on the ground and the possibility of real-time calibration of the RF equipment and the antennas. Another difference is the additional tropospheric influence on the Ground-GEO links, which slightly increases the measurement error in comparison to the LEO-GEO links.

Main Advantages

LEO Satellite Based Concept	Ground Based Concept
High dynamics in the LEO satellite positions enables efficient bias estimation	High ground station positioning accuracy
No tropospheric influences on the LEO-GEO link	High time synchronization accuracy (< 0.5 ns)
Usage of existing telemetry infrastructure is economical	Real-time calibration of RF equipment and antennas possible
	Large Tx ground antennas and high Tx power

Main Disadvantages

LEO Satellite Based Concept	Ground Based Concept
Simple GNSS receivers: - poor time synchronization accuracy	High ground station network operation costs (all antennas dedicated to one single purpose)
- poor real-time LEO satellite positioning accuracy	Poor bias estimation due to missing dynamics in the GEO-Earth constellation
Small LEO satellite Tx antennas	Tropospheric influence on the uplink paths

Table 5.10: Comparison of the advantages and disadvantages of a LEO satellite and a ground based GEO satellite positioning solution.

Dilution of Precision

The PDOP analysis for a ground based variant was already shown in Section 5.3.2. The PDOP for the ESA ESTRACK ground station network comprising 9 stations is 6.2. The number of 9 stations is comparable to the mean number of visible LEO satellites for a 15 LEO satellite approach. The PDOP is slightly higher than the mean PDOP of 5.2 for the 15 LEO satellite constellation (cf. Table 5.8).

Receiver Noise

As explained in Section 5.2.2, the receiver noise is characterized by the Carrier Power to Noise Spectral Density Ratio C/N_0, the carrier bandwidth B, the receiver integration time T_i and the Power Spectral Density $S_\mathrm{m}(f)$. Table 5.11 shows the link budget for the ground based method using comparable hardware setups to the LEO satellite based method. For a BPSK modulation and an integration time of 60 s, the Cramér-Rao Bound (CRB) is 7.4 cm for the LEO satellite similar setup. The tropospheric losses in the uplink of the LEO satellite similar setup lead to a larger CRB than in the purely space based concept.

The receiver noise of ground based concepts can be further reduced by increasing the transmit power or antenna diameter within the limits specified by the ITU. For example, a reflector diameter of > 3 m at equal transmit power of 50 W is sufficient to reach a CRB of < 1 cm.

Clock Synchronization Error

The clock synchronization by GNSS services on the ground allows the application of high-performance GNSS receiver hardware and antenna calibration compared to LEO satellite onboard equipment. The achievable clock synchronization accuracies are higher than for satellite onboard time synchronization. IGS services specifies the accuracy of IGS ground station clock synchronization to 75 ps RMS after $17-41$ hours (cf. IGS Central Bureau [2013]). The United States Naval Observatory (USNO) shows an operational clock-synchronization of approximately 100 receiver clocks with accuracies of < 0.3 ns after 3 hours, which corresponds to a bias of < 10 cm (cf. Hackman and Matsakis [2012]).

Biases

The dominant bias is the clock synchronization error. The residual tropospheric bias after correction is in the centimeter region (cf. Section 5.2.2).

Uplink: Earth-GEO	For Comparison to the LEO Satellite Concept
Carrier Frequency	27 GHz
Carrier Bandwidth	2.3 MHz
Symbol Rate	1 MBd/s
Earth TX Antenna Diameter	0.5 m
Earth TX Antenna Gain	40.8 dBi
Earth TX power	50.0 W
Earth EIRP	56.8 dBW
Free Space Loss	212.7 dB
Atmospheric Loss	1.4 dB
Rain Loss (99.9% availability)	13.4 dB
GEO RX Global Horn Gain	18.0 dBi
GEO RX System Noise Temperature	550 K
GEO RX G/T	-10.1 dB/K
C/N_0	47.8 dBHz
Downlink: GEO-Earth	
Carrier Frequency	27 GHz
GEO TX Antenna Diameter	0.8 m
GEO TX Antenna Gain	44.9 dBi
GEO TX power	25.0 W
GEO EIRP	57.9 dBW
Free Space Loss	212.7 dB
Atmospheric Loss	1.4 dB
Rain Loss (99.9% availability)	13.4 dB
Earth RX Antenna Diameter	5.0 m
Earth RX Gain	60.8 dBi
Earth RX System Noise Temperature	380 K
Earth RX G/T	34.0 dB/K
C/N_0	93.0 dBHz
Overall C/N_0	47.8 dBHz
Cramér-Rao Bound ($T_\mathrm{i} = 60$ s)	7.4 cm

Table 5.11: Link budgets and Cramér-Rao Bounds for ground based variants of the geostationary data relay positioning concept. The parameters are selected, in order to achieve setups comparable to the LEO satellite concept and the pseudolite concept.

Table 5.12 shows the simulation parameters for the ground based approach in Ka-band. In comparison, also the parameters of the LEO satellite based approach are listed (cf. Table 5.6). Corresponding to Table 5.4, a worst case bias of 35 cm for the ground based approach is assumed. The simulation results of the ground based approach are shown in Figure 5.16.

	Ground Based Concept	LEO Satellite Based Concept
Stochastic Noise	Standard Deviation	
$\widetilde{\eta}^n_{\mathrm{EG}}$, $\widetilde{\eta}^n_{\mathrm{LG}}$ Combined Receiver Noise	1 cm	1 cm
$\delta\vec{r}^{\,n}_{\mathrm{E}}$,$\delta\vec{r}^{\,n}_{\mathrm{L}}$ Ground Station/LEO Satellite Position Error		
- Non-Time Critical (1 month)	2 cm	2 cm
Biases	Magnitude	
$\widetilde{b}^n_{\mathrm{EG}}$, $\widetilde{b}^n_{\mathrm{LG}}$ Combined Biases	35 cm	113 cm
(Including the dominant contribution of the Clock Synchronization Error:)	(10 cm)	(90 cm)
(Mean) PDOP		
9 Ground Stations/ 15 LEO Satellites	6.2	5.2

Table 5.12: Error models for the pseudorange simulations for the ground based concept in comparison to the LEO satellite based concept.

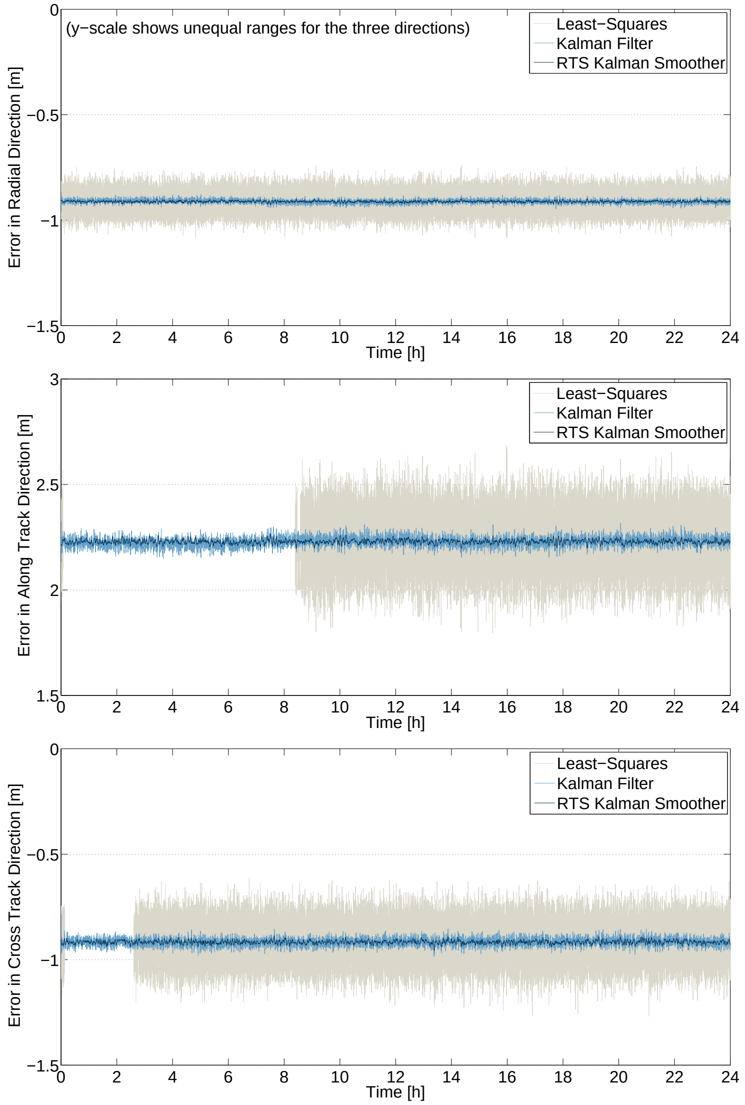

Figure 5.16: Simulated positioning accuracy of a GEO satellite in a ground station based approach. The simulation and noise assumptions are presented in Section 5.3.1. The plots show the Least-Squares solution errors (gray line), the Kalman filter solution errors (blue line) and the RTS smoother error (white line) in radial, along track and cross track direction. Since the biases can not be estimated effectively due to the missing dynamics in the constellation, they increase the errors in the positioning solution. This becomes especially obvious in the direction of the measurements, i.e. the radial direction.

The graphs for the ground based positioning concept are not showing large variations in the positioning uncertainty. This is due to the constant PDOP because of the missing dynamics in the Earth-GEO constellation. The missing dynamics in the constellation however inhibits an effective bias separation from the positioning solution. If the bias estimation is included in the Kalman filter, the biases converge to random values (see Figure 5.17). Applying a Kalman filter without bias estimation leads to a propagation of the unknown biases into the positioning solution (see Figures 5.16). Thus, the positioning results show much larger mean positioning errors compared to the LEO satellite based approach. The Least-Squares estimation errors are much smaller when the biases are not estimated concurrently. Table 5.13 shows the mean positioning values and their accordant standard deviation for the ground based scenario. The accuracies match very well with the accuracies achieved with ranging data produced for supporting the Chinese Area Positioning System (CAPS) as mentioned in ZhiGang et al. [2009]. The orbit determination accuracies are presented to < 2 m. The code noise of the ranging signal was at 1 cm.

	Mean Positioning Error			Standard Deviation		
Ground Based Scenario	Radial	Al. Track	Cr. Track	Radial	Al. Track	Cr. Track
Least-Squares	−91 cm	220 cm	−92 cm	4.3 cm	11 cm	8.0 cm
Kalman Filter	−91 cm	220 cm	−92 cm	0.8 cm	2.1 cm	1.6 cm
RTS Smoother	−91 cm	220 cm	−92 cm	0.4 cm	1.0 cm	0.8 cm

Table 5.13: Simulated positioning accuracies for the ground based scenario. The LEO satellite based results are shown in comparison.

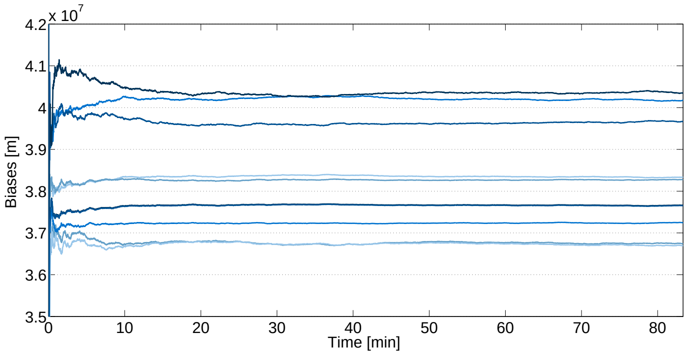

Figure 5.17: The biases converge to random values when estimated with a Kalman filter. This is due to the missing dynamics of the signal sources.

5.3.5 Comparison to a Ground Based Ranging Approach

In the last section, a ground based variant of the LEO satellite based positioning concept was analyzed. It only differs from the conventional ground based ranging concept by using a common downlink to a separate ground station, instead of using multiple two-way ranging links. The performance of both ground based concepts is almost equal assuming an equal network of 9 ground stations and equal link parameters. Only appreciable difference is an additional tropospheric path delay on the downlinks in the conventional ranging approach. If the tropospheric path delay is assumed to be determined at the centimeter level, the effect is negligible.

Practical ground based ranging systems, as cited in Section 5.1.1, often achieve lower accuracies than theoretically estimated in the previous section. Reasons for that are:

- Due to costs, the number of available stations is reduced to $3-4$ stations only (see BRTS system described in Section 5.1.1). If in addition the stations are concentrated in adjacent geographic regions, the DOP can increase to several times the value for the ESTRACK ground station network (cf. Gill and Montenbruck [1998]).
- So far, most satellite systems use lower frequency bands than Ka-band, e.g. S-, C- or X-band, for communication and ranging. At these frequency bands ionospheric path delays are no longer negligible, but dual-frequency receivers can mitigate the influence. When estimated with dual-frequency receivers, the ionospheric bias in S-band at $2.2-2.4$ GHz is comparable to GPS ionospheric biases, which are given in Allain and Mitchell [2008] to approximately $0.1-1$ m.
- Most ground stations are not equipped with high performance RF calibration units. In addition, antennas are often used for serving multiple GEO satellite links consecutively, which requires a change in the angular pointing of the antenna each time the satellite is switched. This can increase the uncertainty of the antenna phase center determination and can cause an increase in the ground station RF equipment biases.
- The EIRP can be limited by ITU or regional regulations, leading to an increased receiver noise. Also the allocation of large bandwidth in these low, but very occupied satellite frequency bands can be limited. Both effects can cause a lower positioning accuracy.

5.4 Summary and Outlook

In this chapter a new variant of GEO satellite positioning was presented. LEO satellites are positioned applying high precision onboard GNSS receivers and serve as navigation satellites for the GEO satellite. Telemetry links between LEO satellites, the GEO satellite and the ground station are used for LEO-GEO-Earth pseudorange measurements. An additional two-way measurement between the ground station and the GEO satellite determines the GEO-Earth distance. The LEO-GEO pseudoranges are separated from the LEO-GEO-Earth measurements. They are used to estimate the position of the GEO satellite.

A separate clock synchronization between the LEO satellite onboard clocks and the ground station receiver clock using GNSS signals is performed. This reduces the PDOP. The GEO satellite is not involved in the processing.

Simulations indicate achievable positioning accuracies in the order of meters for real-time applications and in the order of centimeters for non-time critical applications. This exceeds most of the conventional positioning methods. The remaining positioning error has a negligible influence on the performance of the data relay communications concept.

The effective bias estimation is decisive for achieving such high accuracies. Due to the dynamics in the signal sources, a Kalman filter is able to separate the biases from the positioning solution. Ground based signal sources are at fixed locations, which makes it difficult to separate the biases.

The positioning concept presented in this chapter is cost-efficient. It makes use of the existing communication links and hardware a geostationary data relay for LEO satellites provides. An expensive network of ground stations is not necessary.

As a next step, the concept of using standard telemetry protocols for inter-satellite pseudorange measurements shall be validated with the help of a hardware demonstrator. The demonstrator is currently set up at the laboratory of the Institute for Communications and Navigation at the Technische Universität München. It consists of a Software Defined Radio (SDR) based on USRP hardware devices by ETTUS Research. One USRP device shall serve as transmitter (LEO satellite), another USRP device shall serve as receiver (Ground Station). The two USRP devices shall be synchronized with the help of GNSS timing signals provided by external GNSS receivers. The standard Telemetry Transfer Frame Protocol defined in ECSS-E-ST-50-03C [2008] shall be implemented in software on a PC connected with the USRP devices. A pseudorange measurement between transmitter and receiver shall be validated while a telemetry communication between the nodes via the Telemetry Transfer Frame Protocol is performed. The experiment shall deliver an operational implementation of the concept as well as investigation results about the achievable timing accuracy considering the applied hardware.

A further validation on real spacecrafts is planned within the next years. An experiment performing a pseudorange measurement with onboard hardware and a 3 m ground station at the Technische Universität München was accepted for the OPS-SAT mission. OPS-SAT is a flying experimental platform by the European Space Agency (ESA), which allows changes in the onboard software during flight. A reconfigurable FPGA provides the necessary data handling unit for the onboard implementation of the Telemetry Transfer Frame Protocol defined in ECSS-E-ST-50-03C [2008]. The launch of the satellite is scheduled for 2016.

Appendix A

Link Budget Calculations

A.1 Link Budget Model

The link budgets calculated in this thesis are based on the formalism presented by Maral and Bousquet [2009]. The characteristic of the link budget is expressed by the Carrier to Noise Spectral Density Ratio C/N_0:

$$C/N_0 = \mathrm{EIRP} - L + G/T - k_\mathrm{B} \quad [\mathrm{dBHz}], \tag{A.1}$$

with EIRP the Equivalent Isotropic Radiated Power, L the propagation loss, G/T the antenna gain-to-noise-temperature and k_B Boltzmann's constant.

The different contributions to the link budget are derived in the following section. A visualization is shown in Figure A.1.

Equivalent Isotropic Radiated Power

The EIRP is determined by

$$\mathrm{EIRP} = P_\mathrm{TX} + G_\mathrm{TX} \quad [\mathrm{dBW}], \tag{A.2}$$

where P_TX is the transmit power and G_TX is the transmit antenna gain. If G_TX can not be measured or simulated, it can be estimated by

$$G_\mathrm{TX} = G_\mathrm{max} - L_\mathrm{FTX} - L_\mathrm{T} \quad [\mathrm{dB}]. \tag{A.3}$$

G_max is the maximum antenna gain, estimated for a reflector with circular aperture to

$$G_\mathrm{max} = 10 \cdot \log 10 \left[\eta \left(\frac{\pi D f_\mathrm{C}}{c} \right)^2 \right] \quad [\mathrm{dBi}], \tag{A.4}$$

with the diameter of the transmit antenna aperture D, the carrier frequency f_C, the speed of light c, and the transmit antenna efficiency η. η is usually between $0.55 - 0.75$.

L_{FTX} considers the feeder losses between the transmission amplifier and the antenna. L_{FTX} is typically between $0.5 - 1$ dB. Depointing losses L_{T} are approximated to be small compared to L_{FTX} and are not considered in these link budget calculations.

Propagation Loss

The propagation loss

$$L = L_{\mathrm{FS}} + L_{\mathrm{A}} \quad [\mathrm{dB}] \tag{A.5}$$

mainly consists of the freespace loss L_{FS} and the atmospheric losses L_{A}. The freespace loss is calculated by

$$L_{\mathrm{FS}} = 10 \cdot \log 10 \left(4\pi r f_{\mathrm{C}}/c\right)^2 \quad [\mathrm{dB}], \tag{A.6}$$

where r is the propagation distance.

For LEO-GEO links and GEO-Ground links at 27 GHz, L_{FS} is approximately 213 dB. The atmospheric loss L_{A} in Ka-band is approximately $0.2 - 1$ dB during clear sky conditions (depending on the elevation angle) and 1.4 dB in worst case during cloudy conditions. The loss during rainy conditions can achieve peak values up to approximately 40 dB or more. However, it does not exceed 13.4 dB for more than 0.1% of the time considering a ground station located in Munich, Germany.

Antenna Gain-to-Noise-Temperature

The antenna gain-to-noise-temperature G/T is a figure of merit characterizing the performance of an antenna. It consists of the antenna gain G_{RX} and the system noise temperature T:

$$G/T = G_{\mathrm{RX}} - T \quad [\mathrm{dBK}^{-1}]. \tag{A.7}$$

If the antenna gain G_{RX} can not be measured or simulated, it can be estimated by

$$G_{\mathrm{RX}} = G_{\mathrm{max}} - L_R - L_{\mathrm{FRX}} \quad [\mathrm{dB}]. \tag{A.8}$$

G_{max} is the maximum antenna gain estimated according to Equation (A.4). L_{FRX} is the loss between antenna and receiver, which is typically between $0.5-1$ dB. Depointing losses L_{R} are approximated to be small compared to L_{FTX} and are not considered in these link budget calculations.

The system noise temperature T is calculated by

$$T = 10 \cdot \log 10 \left(T_{\mathrm{A}}/L_{\mathrm{FRX}} + T_{\mathrm{F}} \left(1 - 1/L_{\mathrm{FRX}}\right) + T_{\mathrm{eRX}}\right) \quad [\mathrm{dBK}]. \tag{A.9}$$

Thereby, T_{A} is the antenna noise temperature, T_{F} is the thermodynamic temperature of the feeder and T_{eRX} is the effective input noise temperature of the receiver.

For space antennas facing the Earth at Europe, T_{A} is approximately 260 K. For a ground station, $T_{\mathrm{A}} = T_{\mathrm{Sky}} + T_{\mathrm{Ground}}$. According to Maral and Bousquet [2009], in Ka-band, T_{Ground} is approximately 10 K for elevation angles $> 10°$ and T_{Sky} is approximately 25 K for an elevation angle of 36°. This matches the values for a ground station in Germany pointing to a GEO satellite at 10° East. T_{F} is typically at 290 K. The effective input noise temperature of the receiver can be approximated to be at $T_{\mathrm{eRX}} = 290$ K. The system noise temperature for a space antenne in Ka-band pointing towards the Earth is estimated to approximately 550 K. For a Ka-band antenna on the ground, it is estimated to approximately 380 K.

Boltzmann's Constant

Boltzmann's Constant, which relates the energy at an individual particle level with temperature, is approximately $k_B = -228.6$ dBW/HzK.

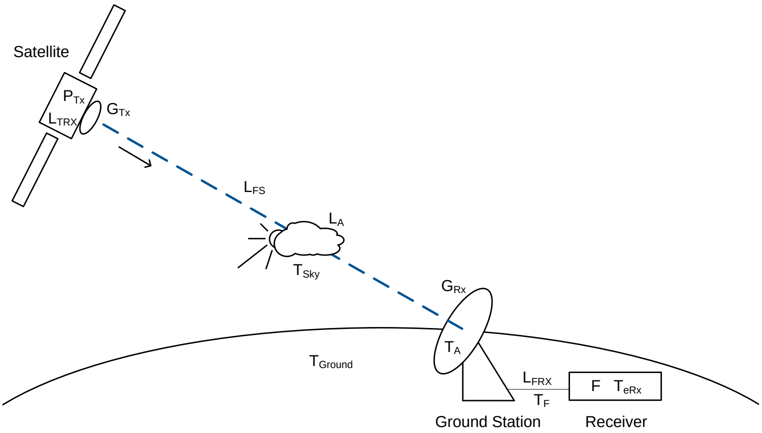

Figure A.1: Different contributions to the link budget for a satellite downlink.

A.2 The Shannon-Hartley Theorem

Considering a Carrier to Noise Spectral Density Ratio C/N_0 on a specific bandwidth B allows to calculate a theoretical upper bound on the maximum achievable data rate at which information can be transmitted over a communications channel. The Shannon-Hartley theorem (cf. Shannon [1948]) can be applied to determine this theoretical tightest upper bound on the information rate. It is called channel capacity C_{c}. It is approximated, that the noise on the channel is additive white Gaussian:

$$C_{\mathrm{c}} = B \log_2 \left(1 + \frac{C}{N_0 \cdot B}\right) \quad [\text{Bit/s}]. \tag{A.10}$$

The channel capacity C_{c} is used to estimate the maximum possible data rate on a communications channel in this thesis. This is a reasonable approximation, since long packet lengths can be used.

Bibliography

AGI STK. Technical Notes, June 2013. URL `http://www.agi.com/resources/help/online/stk/source/hpop/hpop-10.htm`.

D.J. Allain and C.N. Mitchell. Ionospheric Delay Corrections for Single-Frequency GPS Receivers over Europe Using Tomographic Mapping. *GPS Solutions*, 13(2): 141–151, 2008.

C. W. Allen. Optical Aberrations of Reflectors. *Vistas in Astronomy*, 19(2):179–195, 1975.

I. Bahl. *Lumped Elements for RF and Microwave Circuits.* Artech House, 2003.

O. Balbach, B. Eissfeller, G.W. Hein, W. Enderle, M. Schmidhuber, and N. Lemke. Tracking GPS above GPS Satellite Altitude: First Results of the GPS Experiment on the HE0 Mission Equator43. *IEEE Position Location and Navigation Symposium*, pages 243–249, 1998.

M. Born and E. Wolf. *Principals of Optics.* Pergamon Press Ltd., 1959.

R. Brown and P. Hwang. *Introduction to Random Signals and Applied Kalman Filtering.* John Wiley and Sons, New York, 1997.

K. Y. Chan, M. Daneshmand, R.R. Mansour, and R. Ramer. Scalable RF MEMS Switch Matrices: Methodology and Design. *IEEE Transactions on Microwave Theory and Techniques*, 57(6):1612–1621, 2009.

L.G. Cook. Three Mirror Anastigmatic Optical System, 05 1981.

K.D. Dang, S. Slojkowski, D.T. Ward, J. Dunham, and M.R. Blizzard. Tracking and Data Relay Satellite (TDRS) Orbit Determination Using Chain-Dependent Range Biases. *2005 Flight Mechanics Symposium*, 2005.

P. Davenport. A Vector Approach to the Algebra of Rotations With Applications. Technical Report TD-4696, National Aeronautics and Space Administration, 1968.

Dow-Key Microwave Corp. Space Products. Technical report, Dow-Key Microwave Corp., 2013.

G. S. Downs. Space Network Ground Segment Sustainment (SGSS) Mission System Requirements Document (MSRD). Technical report, NASA/GSFC, 2008.

T. Ebinuma, M. Unwin, R. Myatt, E. Rooney, Y. Hashida, and A. Garutti. GEO GPS Receiver Demonstration on a Galileo System Test Bed Satellite. *Proceedings of the ION GNSS 2004*, pages 2721–2727, 2004.

ECSS-E-ST-50-02C. Ranging and Doppler Tracking (ECSS-E-ST-50-02C). Technical report, European Cooperation for Space Standardization, 2008.

ECSS-E-ST-50-03C. Space Data Links - Telemetry Transfer Frame Protocol (ECSS-E-ST-50-03C). Technical report, European Cooperation for Space Standardization, 2008.

B. Eissfeller, G. Ameres, V. Kropp, and D. Sanroma. Performance of GPS, GLONASS and GALILEO. *Photogrammetric Week 07*, pages 185–199, 2007.

G. Elgered. Tropospheric Wet Path-Delay Measurements. *IEEE Transactions on Antennas and Propagation*, 30(3):502–505, 1982.

S.A. Figur, E. Meniconi, U. Prechtel, V. Ziegler, B. Schoenlinner, R. Sorrention, and L. Vietzorreck. Design and Characterization of a Simplified Planar 16 x 8 RF MEMS Switch Matrix for a GEO-Stationary Data Relay. *Proceedings of the 42nd European Microwave Conference*, 2012.

R.A. Frosch. Anastigmatic Three-Mirror Telescope, 06 1978.

M. Fujieda, M. Aida, H. Maeno, Lam Quoc Tung, and J. Amagai. Delay Difference Calibration of TWSTFT Earth Station Using Multichannel Modem. *IEEE Transactions on Instrumentation and Measurement*, 56(2):346–350, 2007.

J. Furthner, A. Moudrak, A. Konovaltsev, J. Hammesfahr, and H. Denks. Time Dissemination and Common View Time Transfer with GALILEO: How Accurate Will It Be? *35th Annual Precise Time and Time Interval (PTTI) Meeting*, pages 185–198, 2003.

E. Gill and O. Montenbruck. xDOP Analysis of PRS Station Network. Technical report, Dornier Satellitensysteme GmbH, 1998.

C. Günther and J.S. Knogl. 3D Attitude Determination from 2D Measurements. *To be published*, 2014.

C. Granet. Designing Schwarzschild Dual-Reflector Systems. *IEEE Antennas and Propagation Magazine*, 48(3):68 –74, June 2006.

W. Gregorwich, R.B. Ward, and L. Capots. A Novel Multibeam Approach for a GEO Positioning Spacecraft System. In *IEEE Aerospace Conference Proceedings*, volume 2, pages 885–890, 2002.

C. Hackman and D. Matsakis. Precision ant Accuracy of USNO GPS Carrier Phase Time Transfer: 2012 Update. *2012 IEEE International Frequency Control Symposium (FCS)*, 2012.

B. Haines, M. Armatys, Y. Bar-Sever, W. Bertiger, S. Desai, A. Dorsey, C. Lane, and J. Weiss. One-Centimetre Orbits in Near-Real Time: The GPS Experience on OSTM/JASON-2. *CalTech*, pages 1–14, 2010.

C. Hajiyev and M. Ata. Error Analysis of Orbit Determination for the Geostationary Satellite with Single Station Antenna Tracking Data. *Scientific Research*, 2:135–144, 2011.

Y. Huang, X.G. Hu, X.Z. Zhang, D.R. Jiang, R. Guo, H. Wang, and S.B. Shi. Improvement of Orbit Determination for Geostationary Satellites with VLBI Tracking. *Chinese Science Bulletin*, 56:2765–2772, 2011.

Y. Hwang, L. Byoung-Sun, K. Hae-Yeon, K. Haedong, and K. Jaehoon. Orbit Determination Accuracy Improvement for Geostationary Satellite with Single Station Antenna Tracking Data. *ETRI Journal*, 30:774–782, 2008.

IGS Central Bureau. IGS Products, June 2013. URL `http://igscb.jpl.nasa.gov/components/prods.html`.

ISS Reshetnev. ISS Reshetnev, October 2013. URL `http://www.iss-reshetnev.com/?cid=prj_ca_loutch5a`.

ITU. Radio Regulations 1. Technical report, ITU, 2008.

B. Johnston, M. Haslam, E. Trachtman, R. Goldsmith, H. Walden, and P. McGaugh. SB-SAT - Persistent Data Communication LEO Spacecraft via the Inmarsat-4 GEO Constellation. In *Advanced Satellite Multimedia Systems Conference (ASMS) and 12th Signal Processing for Space Communications Workshop (SPSC)*, pages 21 –28, Sept. 2012.

E. D. Kaplan and C. Hegarty. *Understanding GPS: Principles and Applications (Second Edition)*. Artech House, Inc., 2006.

Z. Katona. GEO Data Relay for Low Earth Orbit Satellites. *6th Advanced Satellite Multimedia Systems Conference (ASMS) and 12th Signal Processing for Space Communications Workshop (SPSC)*, 2012.

S.M. Kay. *Fundamentals of Statistical Signal Processing: Estimation Theory.* Prentice Hall PTR, 1993.

J.D. Kronman. Experience Using GPS For Orbit Determination of a Geosynchronous Satellite. *Proceedings of ION GNSS 2003*, pages 1622–1626, 2003.

D. Kuang, Y. Bar-Sever, W. Bertiger, S. Desai, B. Haines, B. Iijima, G. Kruizinga, T. Meehan, and L. Romans. Precise Orbit Determinatibn for CHAMP using GPS Data from BlackJack Receiver. *Proceedings of the ION National Technical Meeting 2001*, 2001.

R. Kulke, W. Simon, C. Günner, G. Möllenbeck, D. Köther, and M. Rittweger. RF-Benchmark up to 40 GHz for various LTCC Low Loss Tapes. *IMAPS-Nordic*, 2002.

R. B. Langley. Dilution of Precision. *GPS World*, pages 52–59, 1999.

T. Lewis. 2nd TDRSS Workshop. Technical report, NASA, 1996.

C.C. Liebe. Accuracy Performance of Star Trackers - A Tutorial. *IEEE Transactions on Aerospace and Electronic Systems*, 38(2):587–599, 2002.

E. Lutz, M. Werner, and A. Jahn. *Satellite Systems for Personal and Broadband Communications.* Springer-Verlag, 2000.

B. MacEvoy. Astronomical Optics - Part 4: Optical Aberrations, June 2013. URL `http://www.handprint.com/ASTRO/ae4.html`.

G. Maral and M. Bousquet. *Satellite Communications Systems.* Wiley, 2009.

F. L. Markley and D. Mortari. Quaternion Attitude Estimation Using Vector Observations. *Journal of the Astronautical Sciences*, 48(2):359–380, 2000.

A. Martellucci. Radiowave Propagation Modelling for SatCom Services at Ku-Band and Above. Technical report, ESA, 2002.

R. A. Miller and A. K. Berndt. NASA's Next Generation Tracking and Data Relay Satellite System (TDRSS): Launch and Operational Ground Segment Architecture. In *Fourth International Symposium on Space Mission Operations and Ground Data Systems*, volume 1, pages 240–247, Nov. 1996.

P. Misra and P. Enge. *Global Positioning System: Signals, Measurements, and Performance (Revised Second Edition).* Ganga-Jamuna Press, 2012.

P. Misra and M. Pratt. Role of the Clock in a GPS Navigation Receiver. *ATC Memorandum*, May 1994.

O. Montenbruck, M. Garcia-Fernandez, Y. Yoon, S. Schön, and A. Jäggi. Antenna Phase Center Calibration for Precise Positioning of LEO Satellites. *GPS Solutions*, 13:23–34, 2009.

R. Nakamura. SLR Tracking Standards for Engineering Test Satellite-VIII (ETS-VIII). Technical report, Japan Aerospace Exploration Agency (JAXA), 2006.

R. Nakamura, T. Inoue, S. Nakamura, S. Katagiri, S. Noppanakeepong, and Y. Feng. ETS-VIII Precise Orbit and Clock Estimation Experiments. *Proceedings of the 23rd ION conference*, pages 1572–1579, 2010.

G. Nie, F. Wu, K. Zhang, and B. Zhu. Research on LEO Satellites Time Synchronization with GPS Receivers Onboard. In *IEEE International Frequency Control Symposium Joint with the 21st European Frequency and Time Forum*, pages 896 –900, June 2007.

M.R. Pearlman, J.J. Degnan, and J.M. Bosworth. The International Laser Ranging Service. *Advances in Space Research*, 30(2):135–143, 2002.

B. Pillans, S. Eshelman, A. Malczewski, J. Ehmke, and C.Goldsmith. Ka-Band RF MEMS Phase Shifters. *IEEE Microwave and Guided Wave Letters*, 12(9), 1999a.

B. Pillans, S. Eshelman, A. Malczewski, J. Ehmke, and C. Goldsmith. Ka-Band RF MEMS Phase Shifters. In *IEEE Microwave and Guided Wave Letters*, pages 520–522, 1999b.

T.D. Powell, P.D. Martzen, S.B. Sedlacek, C. Chao, R. Silva, A. Brown, and G. Belle. GPS Signals in a Geosynchronous Transfer Orbit: Falcon Gold Data Processing. *ION Nation Technical Meeting*, pages 575–585, 1999.

Radant MEMS. 2013-2014 RF MEMS Switches and Products Catalog. Technical report, Radant MEMS, 2013.

H.E. Rauch, F. Tung, and C.T. Striebel. Maximum Likelihood Estimates of Linear Dynamic Systems. *AIAA Journal*, 3(8):1445–1450, 1965.

J. Roselló, P. Silvestrin, R. Weigand, S. d'Addio, A. Garcìa, and R. Gustavo López Risueno. Next Generation of ESA's GNSS Receivers for Earth Observation Satellites. *6th ESA Workshop on Satellite Navigation Technologies*, Dec. 2012.

M. Rosengren, J. De Vicente-Olmedo, and F. Pedersen. Keeping Track of Geostationary Satellites - A Novel and less costly Approach. *ESA bulletin*, 119:64–68, 2004.

J.L. Ruiz and C.H. Frey. Geosynchronous Satellite Use of GPS. *Proceedings of the ION GNSS 2005*, pages 1227–1232, 2005.

J.G. Savard. The Five Seidel Aberrations, June 2013. URL `http://www.quadibloc.com/science/opt0505.htm`.

B. Schönlinner, A. Stehle, Ch. Siegel, W. Gautiera, B. Schulte, S. Figur, U. Prechtel, and V. Ziegler. The Low-Complexity RF MEMS Switch at EADS: An Overview. *International Journal of Microwave and Wireless Technologies*, 3:499–508, Oct. 2011.

D. Schroeder. *Astronomical Optics*. Academic Press, 2000.

C.E. Shannon. A Mathematical Theory of Communication. *The Bell System Technical Journal*, 27(3):379–423, 1948.

H. R. Shea. Reliability of MEMS for space applications. *Proc. of SPIE*, 2006.

V.Y. Terebizh. Two-Mirror Schwarzschild Aplanats. Basic Relations. *Astronomy Letters*, 31(2):129–139, 2005.

S. Theil. Autonomous Onboard Orbit and Attitude Control of Geostationary Satellites Using Pseudolites. *Proceedings of the 11th International Technical Meeting of the Satellite Division of The Institute of Navigation (ION GPS 1998)*, pages 1565–1575, 1998.

J. Tombasco. *Orbit Estimation of Geosynchronous Objects Via Ground-Based and Space-Based Optical Tracking.* University of Colorado, 2011.

B. Visser, C. Sabol, and S. Dahlke. Geosynchronous Orbit Determination Using High Accuracy Angular Observations. *Advances in the Astronautical Sciences*, 120, 2005.

W. B. Wetherell and M. P. Rimmer. General Analysis of Aplanatic Cassegrain, Gregorian, and Schwarzschild Telescopes. *Applied Optics*, 11(12):2817–2832, 1972.

G. Whaba. Problem 65-1: A Least Squares Estimate of Spacecraft Attitude. *SIAM Review*, 7(3):409, 1965.

R. Wilke, S. Hamid, K. Schraml, R. Khunti, and D. Herberling. Multi-Layer Patch Antenna Array Design for Ka-Band Satellite Communication. In *International Microwave and Optoelectronics Conference*, 2013.

M. Witting and K. Kably. ARTES 7 EDRS Overview, Oct. 2012. URL `http://telecom.esa.int/telecom/www/object/index.cfm?fobjectid=29643`.

J.T. Wu, S.C. Wu, G.A. Hajj, W.I. Bertiger, and S.M. Lichten. Effects of Antenna Orientation on GPS Carrier Phase. *Manuscripta Geodaetica*, 18:91–98, 1993.

C. L. Wyman and D. Korsch. Aplanatic Two-Mirror Telescopes: A Systematic Study. I - Cassegrainian Configuration. *Applied Optics*, 13:2064–2066, Sept. 1974.

P. Zentgraf, S. Berge, C. Chasset, H. Filippi, E. Gottzein, I. Gutiérrez-Cañas, M. Hartrampf, P.A. Krauss, C. Kuehl, B. Lübke-Ossenbeck, M. Mittnacht, O. Montenbruck, C. Müller, P. Rueda Boldo, and A. Truffi. Preparing the GPS-Experiment for the SMALL GEO Mission. In *33rd Annual AAS Guidance and Control Conference*, 2010.

L. ZhiGang, Y. XuHai, A. GuoXiang, S. HuLi, Q. RongChuan, and F. ChuGang. A New Method for Determination of Satellite Orbits by Transfer. *Science in China Series G: Physics, Mechanics and Astronomy*, 2009.

V. Ziegler, A. Stehle, G. Georgiev, B. Schoenlinner, U. Prechtel, H. Seidel, U. Schmid, and J. Hartmann. SP48T Module Architecture and RF-MEMS Multi-Throw Switches for a Multi-Beam Antenna Measurement Set-Up at K- and Ka-Band. In *39th European Microwave Conference*, pages 1128–1131, 2009.

J.F. Zumberge, G. Hajj, S.M. Lichten, and T.K. Meehan. The NASA/JPL BlackJack GPS Receiver on CONAE's SAC-C Mission. Technical report, Tracking Systems and Applications Section, JPL, CIT, 2003.